DEVELOPMENT OF MULTI-MODAL TECHNIQUES FOR THE INVESTIGATION OF BRAIN ENERGETICS

A Dissertation
SUBMITTED TO THE FACULTY OF
UNIVERSITY OF MINNESOTA
BY

Jennifer Michelle Taylor

IN PARTIAL FULFILLMENT OF THE REQUIREMENTS
FOR THE DEGREE OF
DOCTOR OF PHILOSOPHY

Advised by Wei Chen, Ph.D.

October 2015

© Jennifer Michelle Taylor 2015

ACKNOWLEDGEMENTS

I would first like to acknowledge and express my sincere thanks to my advisor Dr. Wei Chen, for his guidance throughout my PhD research. I would also like to thank my committee, Drs. Geoff Ghose, Pierre-Gilles Henry, Hubert Lim, and Rajesh Rajamani, for their many inputs on the direction of my project, as well as all of my colleagues at the CMRR for allowing me to tap your expertise to answer my multitude of questions.

To the other members of the lab, thank you for allowing me to bounce ideas off of you and helping when extra hands were needed. In particular, I would like to thank Dr. Xiao-Hong Zhu for advice and assistance with all of the experimental details, and Dr. Yi Zhang, without whom my animal experiments would be significantly more difficult.

I would also like to thank my friends, for keeping me sane. And lastly, I would like to thank my parents, whose guidance put me where I am today.

ABSTRACT

The study of spontaneous and highly variable brain activity, or task-evoked activity and its quantitative relationship with neuroimaging signals, is severely restricted by the lack of techniques to investigate multiple measures of brain activity simultaneously. In order to study the coupling and interactions between metabolic, hemodynamic, and neuronal activity, we here develop the technology to acquire *in vivo* magnetic resonance (MR) spectroscopy (MRS) simultaneously from two or more nuclei, as well as develop MR-compatible electrodes for neuronal recording in the MR scanner with minimal susceptibility artifacts. We apply these techniques to investigate metabolic trends resulting from a whole brain occlusion in the rat and to study neuronal, hemodynamic, and network responses to changes in anesthesia depth. Lastly, we show the first steps in developing an MR-compatible optrode to allow simultaneous MR imaging (MRI), neuronal recording, and optogenetic stimulation. With these new techniques, a wide field of studies becomes feasible to investigate direct neuronal, metabolic, and hemodynamic correlations under resting and working conditions to advance our understanding of brain function and dysfunction.

TABLE OF CONTENTS

LIST OF FIGURES

LIST OF ABBREVIATIONS

4BVO	4 blood vessel occlusion model
ADP	Adenosine diphosphate
ATP	Adenosine triphosphate
BISTRO	B_1-insensitive train to obliterate signal saturation scheme
BOLD	Blood oxygenation level dependence
ChR2	Channelrhodopsin-2
CNT	Carbon nanotubes
Cr	Creatine
CSI	Chemical shift imaging
DI	Deionized
DMN	Default mode network
EEG	Electroencephalography
EPI	Echo planar imaging
FASTMAP	Fast, automatic shimming technique by mapping along projections
FID	Free induction decay
fMRI	Functional magnetic resonance imaging
FOV	Field of view
FSEMS	2D fast spin echo sequence
G6P	Glucose-6-phosphate
GABA	γ-Aminobutyric acid
GEMS	2D gradient echo sequence
GO	Graphene oxide
HG	High gamma frequency band, 62-200 Hz
HRF	Hemodynamic response function
KCl	Potassium chloride
Lac	Lactate
LBL	Layer-by-layer
LF	Low frequency band, 0-10 Hz
LFP	Local field potential
LG	Low gamma frequency band, 30-58 Hz
MF	Medium frequency band, 10-30 Hz
MR	Magnetic resonance
MRS	Magnetic resonance spectroscopy
MUA	Multi unit activity
NAA	*N*-acetlyaspartate

NMR	Nuclear magnetic resonance
PCr	Phosphocreatine
PDDA	Poly(diallyldimethylammonium chloride)
PDMS	Polydimethylsiloxane
PEDOT	Poly(3,4-ethylenedioxythiophene)
PET	Positron emission tomography
PET	Polyethylene terephthalate
Pi	Inorganic phosphate
PI	Polyimide
PRESS	Point resolved spectroscopy sequence
PSG	Pulse sequence generator
PSS	Poly(sodium 4-styrene-sulfonate)
RF	Radio-frequency
rGO	Reduced graphene oxide
RMSE	Root-mean-squared error
S1FL	Primary somatosensory forelimb cortex
SCR	Signal-to-contrast ratio
SD	Standard deviation
SNR	Signal to noise ratio
SPULS	Single pulse sequence
SUA	Single unit activity
TE	Echo time
TR	Repetition time
V1	Primary visual cortex
VAPOR	Variable power RF pulses with optimized relaxation delays

Chapter 1 :

INTRODUCTION

The brain is a complex system of interconnected circuits and pathways, consuming a large amount of energy for its size. By investigating the mechanisms and correlations of cerebral functional and metabolic activity, we can develop a better understanding of the normal brain.

Functional magnetic resonance imaging (fMRI) and *in vivo* magnetic resonance spectroscopy (MRS) have played essential roles in the study of brain metabolism, neuroenergetics, hemodynamics, and function. One of the most popular fMRI approaches is based on the blood oxygenation level dependent (BOLD) contrast resulting from a stimulus-evoked overshoot of oxygenated blood, defined as the hemodynamic response function (HRF), due to a blood flow increase greater than the change in oxygen consumption (Ogawa *et al* 1990, Bandettini *et al* 1992, Kwong *et al* 1992, Ogawa *et al* 1992). While an important modality, fMRI is unable to quantitatively elucidate the mechanisms of brain energy and neuronal activity, and their coupling with hemodynamics. It has been found that the brain consumes much more energy than its weight accounts for during rest, with activation only resulting in a small change in energy consumption. The available ATP (an energy molecule) concentration in brain cells at any time, however, is low, with function relying on fast ATP production in mitochondria and efficient transport. Under normal conditions, roughly 90% of this ATP demand is met through oxidative phosphorylation (Rolfe *et al* 1997, Hyder *et al* 2006). *In vivo* MRS allows the direct measurement of cerebral energy using metabolic signals such as ^{1}H and

^{31}P and allowing quantification of intracellular ATP and a variety of cerebral metabolic rates from baseline and dynamic concentrations during changes in brain status (Hopkins *et al* 1987, Merboldt *et al* 1992, Gruetter *et al* 1996, Zhu *et al* 2002, Mateescu 2003, Mangia *et al* 2007, Du *et al* 2008, Zhu *et al* 2009, Zhu *et al* 2012).

Using these methods to study brain function or metabolic activity usually requires studying them individually and separately. In order to explore the correlations and connections between metabolism and function, paradigms must be designed which are reproducible, or rather, are assumed to generate reproducible responses, which can then be compared across repetitions. While this assumption may be reasonable for some stimulus conditions, such as a forepaw electrical stimulation or a flashing checkerboard visual stimulus, it is less likely to hold true for more complex stimuli, in particular under diseased conditions such as a stroke, and severely inhibits the study of spontaneous activity. Additionally, some responses are highly sensitive to the subject or animal's physiological condition and brain state, which can vary significantly even in the same subject. For example, in comparison to awake animals, Martin *et al* observed a delayed and attenuated HRF response to rat whisker pad simulation in anesthetized animals (Martin *et al* 2006). The ability to collect multiple measures of brain activity and neuroimaging signal response simultaneously will allow direct correlations to be calculated, providing insight into the complex workings of the brain.

To truly understand brain function and stimulus response, it is important to study the "resting state", or rather, brain activity when there is no direct paradigm stimulus. Spontaneous activity during resting state, particularly those seen with BOLD fMRI, are now believed not to be physiological noise to be discarded, but instead reflect underlying functional networks responsible for "housekeeping" activities and fundamental brain organization (Biswal *et al* 1995, Fox *et al* 2007, Mantini *et al* 2007). In BOLD fMRI, this intrinsic activity shows patterns of temporal coherence across multiple brain networks, for instance, dubbed the 'default mode of brain function' (Raichle *et al* 2001) and forms the default mode network (DMN). This activity has also been found to affect stimulation response. For example, Hesselmann *et al* found correlations between the spontaneous activity pattern just prior to stimulus onset and the initial perception to a face-vase illusion (Hesselmann *et al* 2008). Spontaneous activity may continue to occur during stimulation, leading to much of the variability seen in evoked responses (Fox *et al* 2006, Fox *et al* 2007), with up to 10% of spontaneous fMRI variance potentially explained by the local field potential (LFP) signal origin (Scholvinck *et al* 2010). These spontaneous fluctuations have also been observed in neuronal activity, exhibiting slow spontaneous fluctuations with multi-network correlations in neuron spiking and gamma-band LFP activity (Nir *et al* 2008), and a positive correlation between gamma-band LFP (40-80 Hz) fluctuations and BOLD fMRI signals (Scholvinck *et al* 2010). While these studies reveal important aspects of neuronal and hemodynamic coupling, they also serve to highlight the remaining unknown energy mechanisms behind spontaneous activity.

Further confounding the investigation of the coupling between neuronal, metabolic, and hemodynamic activity is the affect of anesthesia on these correlations. Anesthesia-depth dependent response suppression to a flicker pattern stimulus was found in rats (White *et al* 2012), and the HRF changed with anesthesia depth (Liu *et al* 2011). Deep isoflurane anesthesia (1.8% - 2.2%) induces global burst-suppression electroencephalography (EEG) activity, which differs significantly from awake brain activity (Vincent *et al* 2007, Liu *et al* 2011). These bursts have been found to have strong resting state coupling correlations between EEG and cerebral blood flow (CBF) in rat cortex (Liu *et al* 2011). The spontaneous nature of these bursts prohibits direct investigation of this coupling with BOLD activity, although CBF and BOLD correlations paired with EEG-CBF correlations indicate tight neurovascular coupling and point to an underlying neuronal origin for resting state BOLD fluctuations (Liu *et al* 2011).

Intrinsic spontaneous fluctuations are commonly eliminated by the traditional fMRI analysis method of averaging many trials to improve neuroimaging signal-to-contrast ratio (SCR). As the importance of these fluctuations becomes more apparent, new methods of analysis are needed which allow the identification of these oscillations and their neuronal and hemodynamic correlations. Multi-modal electrophysiology and MRI experiments are used to investigate this neurovascular coupling (Logothetis *et al* 2001, Shmuel *et al* 2006, Pan *et al* 2011), however the results remain unclear, sometimes

finding LFP as a better predictor of BOLD, other times pointing towards multiple unit activity (MUA). Visual suppression stimuli found a stronger gamma LFP (25-80 Hz) link to BOLD fMRI (Bartolo *et al* 2011), supporting Logothetis *et al*'s conclusion. Sensitivity to color and natural images in monkeys was used to dissociate LFPs and single unit activity (SUA), resulting in regional specific correlations to BOLD (Liebe *et al* 2012). In human auditory cortex, SUA firing rates were found to better predict group fMRI response than LFP activity (Mukamel *et al* 2005). Synchronous activity was found between fMRI and LFP signals in rats during seizure activity (Airaksinen *et al* 2010), however negative BOLD has also been found in deep brain structures during periods of high LFP and spike activity (Schridde *et al* 2008) and carbon fiber electrode microstimulation in posterior hypothalamus during fMRI elicited a positive cortical BOLD response that was only correlated with LFP and MUA for the first few seconds of stimulations, before becoming decorrelated for the sustained stimulation (Young *et al* 2011). However Shmuel *et al* found correlations between negative BOLD and decreased LFP and MUA activity, although not as strongly correlated as with positive BOLD (Shmuel *et al* 2006).

These correlations additionally exhibit nonlinear behaviors. Just *et al* applied a varying stimulation current, eliciting a sigmoidal curve of BOLD response and a minimum threshold to elicit a hemodynamic response (Just *et al* 2010). Previous work found nonlinear coupling between Laser Doppler flowmetry measured CBF and ∑LFP

(Nielsen *et al* 2001). These findings highlight the complexity of the brain, as well as the large dependence of response to the stimulation paradigm and region of interest. In order to gain a better understanding of this coupling, the analysis of multiple simultaneous measures of brain activity and neuroimaging signals are necessary.

To advance the study of the coupling between neuronal, metabolic, and hemodynamic activity, this dissertation work aims to develop new multi-modal techniques to allow the simultaneous acquisition of neuronal activity, MRS, and fMRI. With this technology, assumptions of reproducibility, stable physiological condition, and constant brain state are removed from multi-parametric correlations, facilitating the reliable study of spontaneous activity and dynamics. First, new methods were implemented for dual-nuclei MR acquisition, tightly interleaving ^{1}H MRS and ^{31}P MRS sequences to allow the comparison of a wide variety of metabolites and their dynamic trends. To investigate coupling between neuronal activity and BOLD or metabolic activity, an MR-compatible electrode was developed utilizing nano-structured carbon materials to minimize imaging susceptibility artifacts. A brain occlusion model provided an interesting pathological state that was monitored with the dual ^{1}H-^{31}P MRS sequence for testing and evaluating the novel techniques. Despite a consistent model, high response variability was found in the cellular lactate (Lac) versus phosphocreatine (PCr) trends that would have been missed without simultaneous acquisition. Compared with bench electrophysiology studies, low frequency neuronal activity followed BOLD more closely

than metabolic concentrations. The addition of the MR-compatible electrode into the magnet allows simultaneous BOLD fMRI and LFP acquisition during steady state as well as during a changing anesthesia paradigm. Through these data sets, I investigated dissociations between BOLD network activity and LFP as the anesthesia level changed. Lastly, preliminary work on the development of an MR-compatible optrode will allow future simultaneous investigation of BOLD and neuronal responses to optogenetic stimulation.

This technique advancement now allows investigation into direction neuronal, metabolic, and functional coupling, as well as neural connectivity under normal and pathological brain states for both spontaneous and working activity. Through the application of these techniques, insight into the neuroenergetic mechanisms of the brain can be gained, furthering the overall understanding of individual brain responses.

Chapter 2 :

DUAL NUCLEI MRS

2.1 BACKGROUND

Typical MR imaging looks at the large water signal present in the human or animal body. In contrast, MRS is an excellent technique to explore brain metabolism and energetics under normal and pathological conditions by acquiring signals from brain metabolites in the proton (^{1}H) and other (X-nuclei) spectra. Of high relevance to the investigation of brain energetics is ^{1}H, phosphorus (^{31}P), carbon-13 (^{13}C), and oxygen-17 (^{17}O) MRS. In this dissertation, I focus on the acquisition of ^{1}H and ^{31}P spectroscopy.

Proton spectroscopy is popular for its ability to see baseline concentration of a wide variety of metabolites, and as it does not require additional hardware compared to ^{1}H MRI. Major metabolites include *N*-acetlyaspartate (NAA), creatine (Cr), γ-aminobutyric acid (GABA), glutamate, glutamine, and lactate. ^{1}H MRS is of major use in the investigation of biomarkers for clinical diseases, both for diagnosis and treatment monitoring. For example, NAA is considered a biomarker of neuronal health, and is reduced in diseases associated with demyelination such as multiple sclerosis and Alzheimer's (Jenkins *et al* 1999). Elevated GABA levels have been found in pontine and putamen of Parkinson's Disease patients (Emir *et al* 2012). Importantly, some of these changes are reversed following treatment, making ^{1}H MRS a powerful tool for not only disease diagnosis but for clinical monitoring of disease progression and treatment efficacy. ^{1}H MRS can be quantified through the measurement of water as a concentration reference, or through calibration with known metabolic concentrations. The ^{1}H MRS

signal is many times lower than that of water, and so the water peak must be suppressed in order to see the metabolites (Dreher *et al* 2005). Different parameters in the ^{1}H MRS sequence are modified to adjust and optimize which metabolites are detected *in vivo*.

The investigation of brain energy metabolism is typically accomplished with ^{31}P MRS. ^{31}P is composed of inorganic phosphate (Pi), PCr, ATP, and other molecules with phosphorous atoms. ATP is the major energy molecule for brain function, providing a direct measure of brain energy pools. By saturating the ATP or Pi peaks with magnetization transfer methods, the rate of metabolic flux between PCr and ATP, or between Pi and ATP, can be calculated. The chemical shift of the Pi peak is also pH sensitive (Petroff *et al* 1985), allowing brain pH to be determined using the chemical shift difference between PCr and Pi. These measures allow the direct investigation of brain energy transfer, particularly under different anesthesia levels or during a stimulation paradigm.

Other popular X-nuclei include ^{13}C and ^{17}O. ^{13}C allows the investigation of the Krebs cycle by using ^{13}C-isotope labeled glucose or acetate and watching their dynamics as they move through the cycle, looking at metabolic consumption rates and identifying specific sub-steps of the cycle. Distinct from ^{15}O PET, ^{17}O as part of oxygen O_2 does not have a detectable MR resonance signal until it is metabolized into water in the mitochondria. ^{17}O MRS can be used to investigate the cerebral metabolic rate of oxygen,

cerebral blood flow, and oxygen extraction fraction simultaneously *in vivo* (Hopkins *et al* 1987, Mateescu 2003, Zhu *et al* 2011).

MRS shows great potential as a clinical tool for diagnostics and treatment monitoring, and much work has been done to develop an array of acquisition sequences for these different nuclei. However, MRS is slow to become integrated into the clinical workflow. Of particular interest in this dissertation is the long acquisition time that must be implemented due to low signal and slow longitudinal relaxation times. To reduce this time, a dual nuclei acquisition sequence is implemented here to acquire signals from two nuclei simultaneously in a single MRS sequence.

The technology now exists to easily acquire data from two nuclei (channels) in a single repetition time (TR) with minimal modifications. Some work was done on dual-channel acquisitions in the 80's and 90's, however they typically required high engineering expertise to implement, as well as sequence programmers to develop custom code to match the custom hardware. Kan *et al* developed a triple resonance coil to acquire ^{1}H, ^{2}H, and ^{13}C resonances in order to acquire ^{1}H decoupled ^{13}C spectroscopy, with the ^{2}H signal used for NMR sample spin locking (Kan *et al* 1980). Schnall *et al* developed a triple nuclei sequence to acquire ^{31}P, ^{1}H, and ^{23}Na simultaneously at 2.1T (Schnall *et al* 1988). Using similar methods, Eleff *et al* measured ^{1}H, ^{31}P, and ^{23}Na with two-minute resolution and ^{19}F with 20-second resolution in an interleaved fashion (Eleff *et al* 1988).

Combined ^{1}H and ^{31}P MRS was performed by Gyulai *et al* and Chang *et al* with 5 minute temporal resolution, and by Rudin *et al* with 7 minute resolution (Gyulai *et al* 1987, Rudin *et al* 1989, Chang *et al* 1990). The ability to apply spatial encoding with multiple nuclei simultaneously is complicated by the different effects of gradients on each nuclei, however it has been implemented as imaging for ^{1}H-^{19}F and ^{1}H-^{31}P (Schnall *et al* 1987), and as chemical shift imaging (CSI) for ^{1}H-^{31}P (Gonen *et al* 1994), ^{1}H decoupled ^{31}P-^{19}F (Gonen *et al* 1997), and ^{1}H-^{13}C (Smith *et al* 2012).

Here, simple hardware and software modifications are implemented on to Agilent 9.4T and 16.4T scanners to allow the acquisition of ^{1}H and ^{31}P MRS within a single sequence. The techniques developed here have resulted in a few robust sequences usable with any two nuclei, and the knowledge on how to implement additional sequences.

2.2 HARDWARE MODIFICATIONS

Standard MRI scanners are not designed to collect signal from multiple nuclei simultaneously. In order to circumvent this restriction, the fundamental organization and setup of the scanner hardware must be understood. Here, the radio-frequency (RF) pulse excitation and NMR signal receive circuitry was determined for a 9.4T and a custom configuration 16.4T Magnex Scanner with an Agilent console running VnmrJ.

The 9.4T scanner consists of 8 transmission-receiver channels, including 7 high band channels for ^{1}H and 1 low band for X-nuclei. As we are not interested in

multichannel single-nuclear excitation at this time, focus was on making the primary ^{1}H channel run in parallel with the X-nuclei channel. Hardware for these different bands is also tuned to account for the frequency range of interest, however in general, the circuit for each channel follows the same basic configuration.

For RF excitation, a wave of the desired frequency is generated and amplitude modulated to achieve a desired excitation pulse profile. The RF power is sent to a predetermined preamplifier, here Preamplifier 1 for ^{1}H and Preamplifier 2 for X-nuclei. The preamplifier board feeds the power into the transmit/receive RF coil. The RF pulse excites the spins, and the resulting NMR signal (or FID) is received as a modulation on a base signal that is sent back to the preamplifier. This receive signal is routed through a mixer and sent outside the magnet room to the hardware room. To minimize the overall number of connections, the receive signal from multiple preamplifiers are feed into each mixer, and all mixer outputs are routed through a single switch to one magnet room output. Prior to entering the receiver boards in the hardware room, the signal passes through another switch to route it to the appropriate receiver (**Figure 2.1**A).

The main hurdle for allowing the acquisition of two or more nuclear signals simultaneously is getting both signals out of the magnet room. Multiple nuclear transmit is standard for magnetization transfer studies, for example, and thus no modifications are needed for basic pulses. However for the receive side, it must be ensured that the

preamplifiers for the desired channels are routed through different mixers. The mixer switch must then be bypassed, and additional scanner room outputs must be installed. The receiver room switch must also be bypassed. Since the ^{1}H and X-nuclei pipelines are both directed through Mixer 1 in this 9.4T configuration, the X-nuclei preamplifier output must be redirected to Mixer 2. The installation of another cable allows the output of Mixer 2 to bypass the switch and leave the magnet room. This output is directly connected to the X-nuclei preamplifier, bypassing the second receive switch (**Figure 2.1**B).

These modifications can be made such that the normal operation of the ^{1}H channel is not affected, with only a few cables to adjust prior to simultaneous acquisition. These simple alterations allow the acquisition of two nuclei simultaneously, and can be applied to any similar stock Agilent systems. Hardware flow in custom installations, such as at our 16.4T, must be carefully analyzed to incorporate the same changes. In our case, no hardware modifications are required at the 16.4T to allow simultaneous acquisition of two nuclei.

In addition to the magnet hardware, the RF coil must have the capability to be tuned to multiple frequencies. For these studies, a dual-tuned surface coil consisting of a butterfly ^{1}H coil with a single loop ^{31}P coil (**Figure 2.2**) was used, with the channels passively decoupled to minimize crosstalk. To acquire more than two nuclei, a more

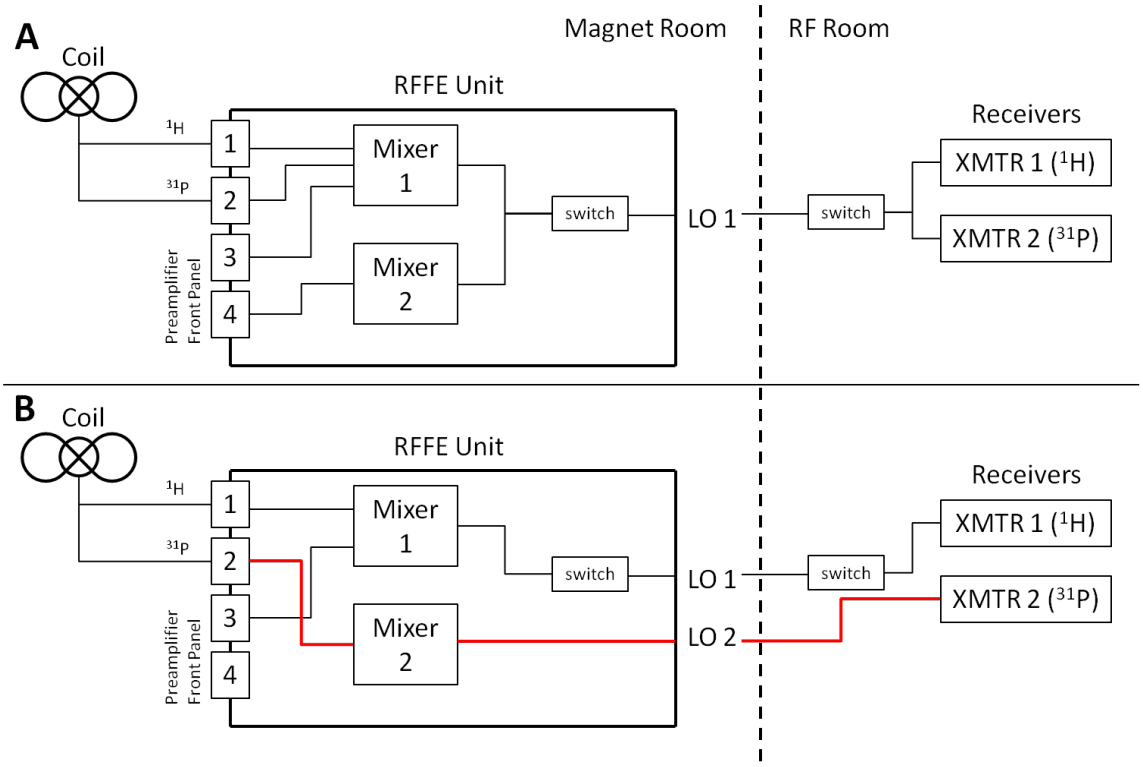

Figure 2.1. *Hardware modification diagram for the 9.4T scanner. (A) Default setup for single channel acquisition. (B) Dual channel setup.*

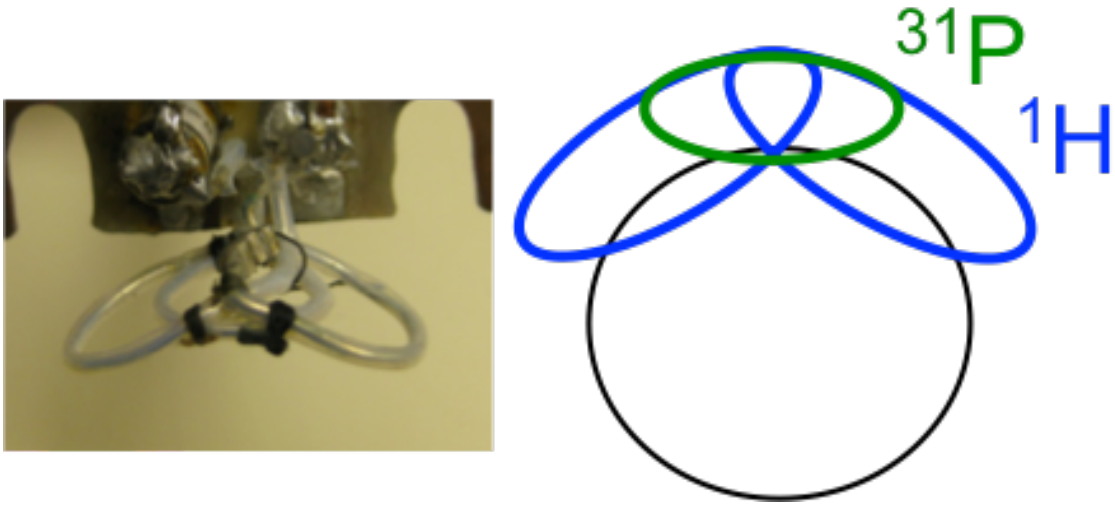

Figure 2.2. *RF coil picture and schematic demonstration of the dual-tuned butterfly ^{1}H and single loop ^{31}P RF coil.*

complex coil design would be required. Potential solutions include having nuclei of close frequencies share a physical coil with circuitry to switch between them, such as the tank circuit based coils designed by Eleff *et al* to acquire ^{1}H, ^{19}F, ^{23}Na, and ^{31}P (Eleff *et al* 1988).

2.3 SOFTWARE MODIFICATIONS

Hardware modifications alone are not sufficient to allow acquisition on both channels. Under normal operation, the software designated acquisition nuclei results in the specific activation of a preamplifier, a mixer input, and the two switches. Manual activation of the pipeline for the second nucleus cannot be performed in the MR sequence itself. Instead, modifications must be made in the software level below this, specifically the pulse sequence generator (PSG) file. In specific locations of the PSG, the desired preamplifiers and receiver boards must be turned on. Triggers were made so that these special modifications are only accessed on command, ensuring that normal usage of the scanner is not affect. Once located, these changes only required the addition of a few lines of code, and are easily added to any account.

2.4 SEQUENCE PROGRAMMING

As a result of the popularity of heteronuclear decoupling sequences, basic functions are built into the VnmrJ pulse sequence settings allowing for simple RF excitation pulses on two nuclei channels simultaneously. Simultaneous acquisition, however, requires multiple receivers to be turned on, and is limited by the memory

handling setup of the VnmrJ software. When an acquisition is performed on one receiver, the other receiver must also acquire data. These acquisitions must be matched in time, number of points collected, and separation of the collected points (spectral sweep width). Multiple acquisitions periods within a single TR must also meet these rules. A few sequences acquire single points instead of a full FID, and these numbers can be overwritten so that less points are acquired than specified, however multiple time-synchronization checks must be overridden to allow this acquisition scheme.

To meet these restrictions, nuclei must be chosen which have similar acquisition parameters. Here, we created sequences for the simultaneous acquisition of ^{1}H and ^{31}P in a modular fashion, as they require similar relaxation times, sampling times, and sweep widths. For example, a combined single pulse (SPULS) ^{1}H and single pulse ^{31}P sequence was created to allow for easy global signal measurement and RF power calibrations. A sequence combining the single voxel PRESS (point resolved spectroscopy) ^{1}H sequence and the global single pulse ^{31}P sequence, seen in **Figure 2.3**, was created to acquire localized ^{1}H metabolites and global brain ^{31}P metabolites. For nuclei with a faster signal recover time, multiple repeats of one sequence can be performed within the TR, as in **Figure 2.4**, where multiple global ^{2}H signal acquisitions can be performed for each single voxel ^{1}H acquisition.

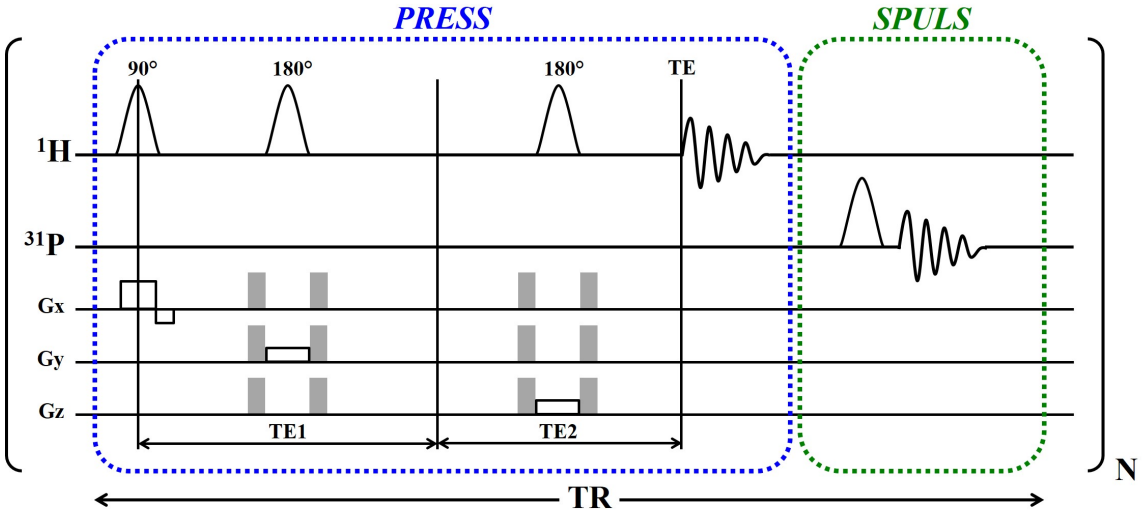

Figure 2.3. *Schematic of a dual channel sequence combining ^{1}H PRESS (blue) and ^{31}P SPULS (green) acquisition. All gradient modulations are performed for PRESS voxel localization. FID acquisition occurs on both channels during each indicated section. With this modular design, additional components such as water suppression are easily added.*

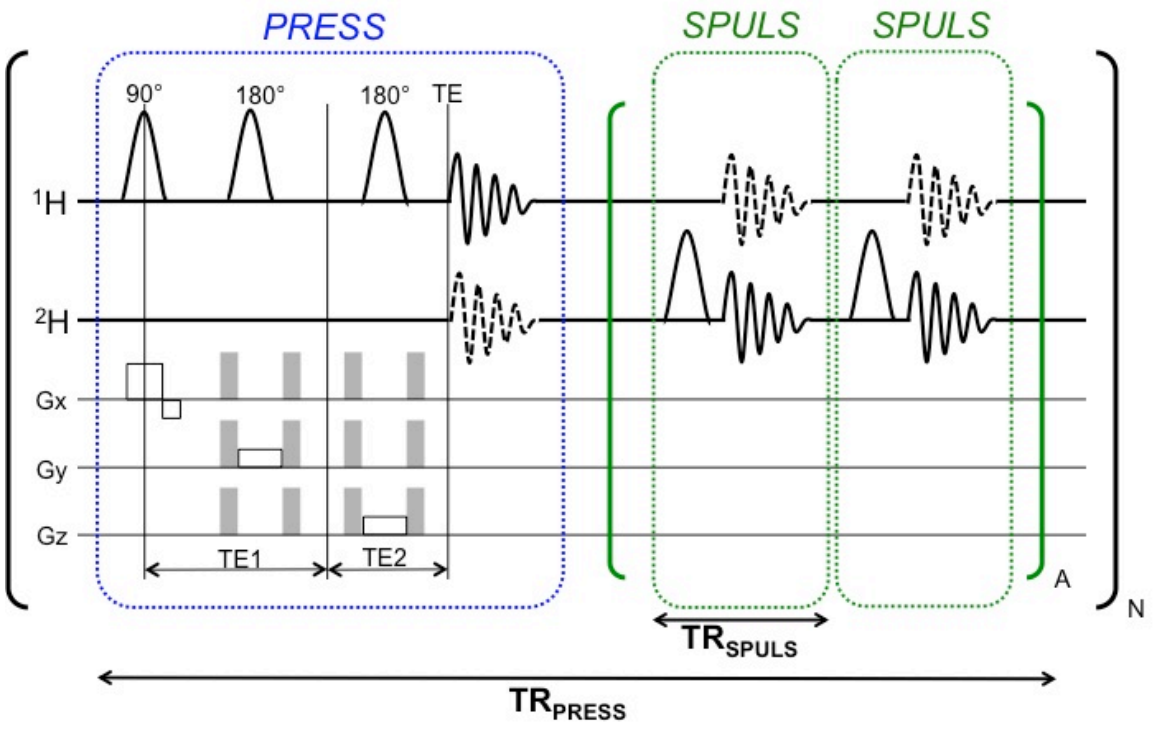

Figure 2.4. *Alternative sequence design incorporating multiple repeats of a second nucleus pulse, here ^{2}H with its short relaxation time. Dashed line FIDs are discarded as noise.*

2.5 EXPANSION TO MORE SEQUENCES

In an ideal world, any two sequences can be combined based on the same design concept. For example, acquisition of metabolic rates instead of steady state concentrations would provide valuable insight into brain mechanisms and neurophysiology. However, for such a sequence, a constant frequency specific saturation pulse train must be applied, here tested using a BISTRO (B_1-insensitive train to obliterate signal) saturation scheme (Chen *et al* 1997, Luo *et al* 2001). The time lost to acquire even a brief ^{1}H single voxel localized MRS sequence disturbed the saturation steady state, making the flux calculations less reliable. Simultaneous acquisition of fMRI or anatomical MRI with X-nuclei MRS would also provide valuable coupling information between hemodynamics and energy metabolism but is limited by the sampling restrictions previously discussed, and needs further development.

2.5.1 POTENTIAL SOLUTIONS

While not investigated in depth for this dissertation, a few potential solutions exist to allow different sampling schemes on each channel. Firstly, a complete reworking of the data handling structure of the VnmrJ system must be implemented, particularly focusing on how the memory buffer is handled, allowing for separate data pipelines for each channel. All of the redundant safety and timing verification checks must then be updated to allow proper synchronization of the different components of the scanner's control system. Lastly, reconstruction algorithms and data display macros would have to be reworked to account for these changes.

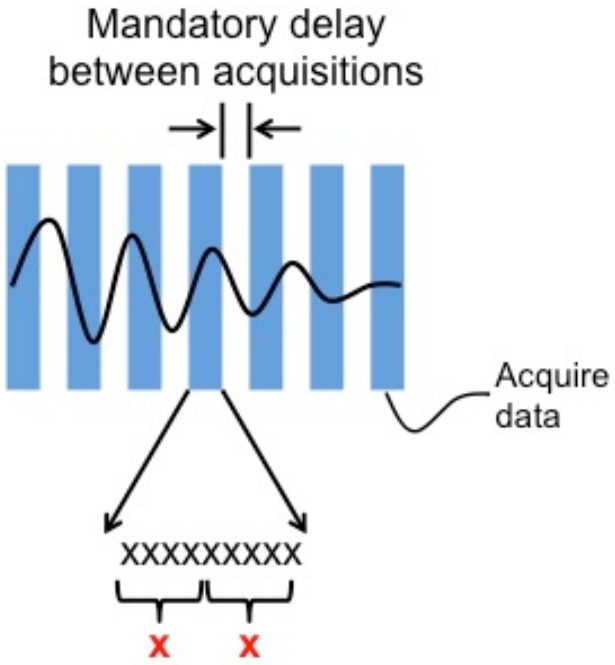

Figure 2.5. *Schematic showing an alternative acquisition scheme for high sampling of a signal which requires a low sample rate, by sampling at the maximal rate (black x) and averaging down to the required rate (red x).*

Alternatively, the restrictions of the system could be worked to the advantage of the data. Using multiple high-sample rate acquisitions in a row, data can be sampled over a longer period of time. A mandatory delay period between each acquisition complicates this method, however this issue could potentially be worked around using non-linear Fourier reconstruction methods. To recover the desired sample rates, the high rate data should be averaged over the period. A schematic of this method can be seen in **Figure 2.5**. Preliminary testing revealed a sensitivity decrease, indicating that true low-rate sampling internally collects samples from an open sensor for entire duration of each point, which cannot be fully replicated with the averaging of shorter duration points. However, taking the signal-to-noise ratio (SNR) loss, this method would allow simultaneous echo planer imaging (EPI) and X-nuclear MRS.

2.5.2 NOISE CONSIDERATIONS

Here we used a dual-tuned decoupled $^{1}H/^{31}P$ surface coil. Under normal use, only one component of the coil is connected to the system at a time, with the other component terminated with a 50Ω resistor to minimize crosstalk. However, during simultaneous acquisition, this is not an option. In order to quantify the amount of noise and crosstalk introduced by having both channels connected at the same time, baseline noise floors were calculated with a high-concentration ATP phantom. SNR was calculated using the built-in algorithms in VnmrJ. It was determined that adding a low pass filter to the ^{31}P channel and a high pass filter to the ^{1}H channel eliminated any signal degradation as compared to each channel connected on its own. Based on the amount of decoupling and

system hardware, this test must be repeated for each coil and system. No difference in SNR was found at the 16.4T when comparing single channel versus both channels connected. Additionally, each new sequence should be verified to not introduce noise due to unintended interactions.

2.6 CONCLUSION

With these simple hardware changes and the development of dual channel sequences, we are able to acquire twice the amount of data in a single TR as compared with normal acquisition methods. By acquiring simultaneous ^{1}H and ^{31}P MRS metabolite data, direct correlations between them can be made without the assumption of paradigm reproducibility and allowing extension into spontaneous data.

Chapter 3 :

MR-COMPATIBLE ELECTRODES

This chapter is modified from the submitted manuscript:

Taylor, Jennifer M, Corey Cruttenden, Shan Hu, Xiao-Hong Zhu, Yi Zhang, Rajesh Rajamani, Wei Chen. "Simultaneous MRI and Electrophysiology Acquisition with Nano-Structured Carbon Electrodes: A Proof of Concept Study."

3.1 BACKGROUND

Brain function relies on a complex interaction between local, global, and network level activity. The investigation of global activity is typically performed with functional MRI (fMRI), utilizing its high spatial sensitivity and a large field of view. Neuronal recording methods are used to study local neuronal activation with high temporal resolution. No single modality can measure the full multi-scale nature of brain dynamics; however combining fMRI and neuronal recording will provide valuable insight into the correlations of this activity. Hindering the development of simultaneous fMRI and neuronal recording techniques is the large susceptibility distortion introduced into the MR images from the standard neuronal electrode materials. Echo planar imaging (EPI), one of the most commonly used fMRI sequences, is particularly sensitive to susceptibility artifacts, becoming unusable in the presence of metal. One common solution is to simply avoid fMRI analysis in regions close to the implanted electrode. Other methods of circumventing the image artifacts issue have also been explored (Logothetis *et al* 2001, Shyu *et al* 2004, Dunn *et al* 2009, Airaksinen *et al* 2010, Pan *et al* 2011), but either the experimental setups were very complicated, or care was taken to use custom sequences to minimize artifacts.

Looking at the neuronal recording side, the radio-frequency (RF) excitation pulses and modulated gradient fluctuations of the MR acquisition induce large electrical artifacts in the recorded neuronal trace, herein referred to as MR-induced artifacts. These MR-

induced artifacts often oversaturate the neuronal recording amplifier, eliminating any chance of recovering the obscured neuronal activity signal. Current methods for signal recovery require complex circuitry to cancel out the MR-induced artifact prior to reaching the amplifier (Oeltermann *et al* 2007), or simply mask out the artifact heavy sections of data, preventing true simultaneous acquisition.

To eliminate susceptibility artifacts, we looked to the new nano-structured carbon materials carbon nanotubes (CNT) and reduced graphene oxide (rGO). This chapter presents data to show that carbon based nano-structured materials induce minimal susceptibility artifacts and distortion in anatomical MRI and fMRI images, even at the electrode site and at ultrahigh field strengths. Carbon fiber has been tested as an electrode material in the past (Dunn *et al* 2009), however large manufacturing variations were observed, and some susceptibility artifacts remained that required careful sequence choices.

CNT and GO/rGO have recently been highlighted for their unique electrical properties (Yang *et al* 2010), and new breakthroughs using these carbon based nanomaterials are being made in a wide range of applications including supercapacitive energy storage (An *et al* 2001, Yu *et al* 2010, Hu *et al* 2012), electrochemical sensing (Alwarappan *et al* 2009), optochemical sensing (Manivannan *et al* 2011, Manivannan *et al* 2012, Shabaneh *et al* 2014), and neuronal interfacing (Ben-Jacob *et al* 2008, Bareket-

Keren *et al* 2012, Kuzum *et al* 2014). Recently, these materials have shown promise for enhancing neuronal recordings. Carbon nanomaterials have been used as a functionalization method for traditional electrode contact surfaces, with carbon nanosheets of graphene increasing the signal-to-noise ratio (SNR) of recordings in mouse primary hippocampal neurons (Collaert *et al* 2014). CNT coating on gold electrodes increased the *in vivo* SNR due to a 45-fold increase in charge transfer (Keefer *et al* 2008), and LFPs recorded with CNT functionalized electrodes increasing SNR during LFP detected seizure activity (Kuzum *et al* 2014). While not yet completely understood, this SNR improvement is likely related to a significantly increased contact surface area as well as a capacitance dominated charge transfer (Bareket-Keren *et al* 2012).

Additionally, culture studies have found preferential neuronal growth and migration towards and on CNT (Sorkin *et al* 2006, Ben-Jacob *et al* 2008, Li *et al* 2011, Park *et al* 2011, Sahni *et al* 2013), and axonal entanglement was found with rat neurons (Bareket-Keren *et al* 2012). Preferential differentiation into neurons was found with higher survival rates on graphene-covered glass than on plain glass (Park *et al* 2011), supported by generally superior survival and growth (Sahni *et al* 2013) with longer neuronal axons (Li *et al* 2011) found on graphene. In a comparison of multi-walled CNT, GO, and rGO, stable viability of fibroblasts were found with increased transfection efficiency (Ryoo *et al* 2010). However, when seeded in a GO suspension, acceptable survival rate was only found for concentrations below 20 μg/mL, and organ tissue was

inflamed following tail vein injections of 0.1 and 0.25 mg GO (Wang *et al* 2010). Graphene has also been applied *in vivo*, and was observed by Park *et al* to give stable electrical recordings over a period of 70 days (Park *et al* 2014). Stable long term impedance *in vivo* was found with PEDOT nanotubes by Abidian *et al* from implantation day 8 to 50 (Abidian *et al* 2009). The unique electrical properties of the nanomaterials used here may be beneficial in reducing the MR-induced artifact amplitudes.

To the best of our knowledge, we here present the first investigation of the use of CNT and rGO electrodes to reduce imaging artifacts in MRI scanners. By creating nanomaterial CNT or rGO electrodes on a polymer base, we have manufactured neuronal recording electrodes with reasonable LFP signal amplitude, good SNR, and minimal susceptibility artifacts. We demonstrate a unique proof-of-concept for the MR-compatibility of these electrodes *in vitro* and *in vivo* at the ultrahigh MRI field strength of 9.4T, including truly simultaneous neuronal recordings and fMRI under a dynamic anesthesia paradigm.

3.2 MATERIALS & METHODS

3.2.1 ELECTRODE MANUFACTURING

Figure 3.1 shows a flow chart for the manufacturing of nano-structured carbon electrodes. A substrate polymer film of polyethylene terephthalate (PET, 5 mil) or polyimide (PI, 3 mil; Kapton, NH) was prepared for deposition of nano-material film

using layer-by-layer (LBL) nano-assembly methods similar to those performed by our collaborators previously (Xue *et al* 2007, Yu *et al* 2007). The film was soaked in 6 M NaOH for 20 minutes at 60°C, followed by 15 minutes soaking in a polyelectrolyte bath of poly(diallyldimethylammonium chloride) (PDDA), then poly(sodium 4-styrene-sulfonate) (PSS), and again PDDA, each with 0.5 M NaCl.

A dispersion of carbon nanomaterial, either CNT or graphene oxide (GO), was prepared. For CNT, 100 mg of L.MWNTs-2040 (NTP, China) nanotubes was stirred in 40 mL of 3:1 H_2SO_4: HNO_3 for 90 minutes at 110°C. The dispersion was diluted to 200 mL, then repeatedly rinsed and filtered (0.22 μm pores) to a neutral pH. The CNT nanotubes were flushed from the filter with deionized water, yielding approximately 50 mL of dispersion. Alternatively, GO was prepared by diluting 5 g/L aqueous graphene oxide dispersion (Graphene Laboratories, Calverton, NY) to 1.5 g/L. The CNT and GO dispersions were ultrasonically agitated for 60 and 30 minutes respectively. The chosen nanomaterial was then drop cast onto the treated polymer substrate and allowed to dry. Electrostatic forces between the negatively charged nanomaterial and the positively charged polymer substrate improve film adhesion. Additional layers of nanomaterial may be drop cast to increase nanomaterial surface concentration. For CNT-based electrodes, the desired geometry was cut from the substrate once dry. For GO-based electrodes, laser treatment was used to reduce the nonconductive GO into conductive reduced graphene oxide (rGO) prior to cutting the electrode from the substrate. The electrodes were cut such that the connection end was located outside the field of view of the RF coil. Silver

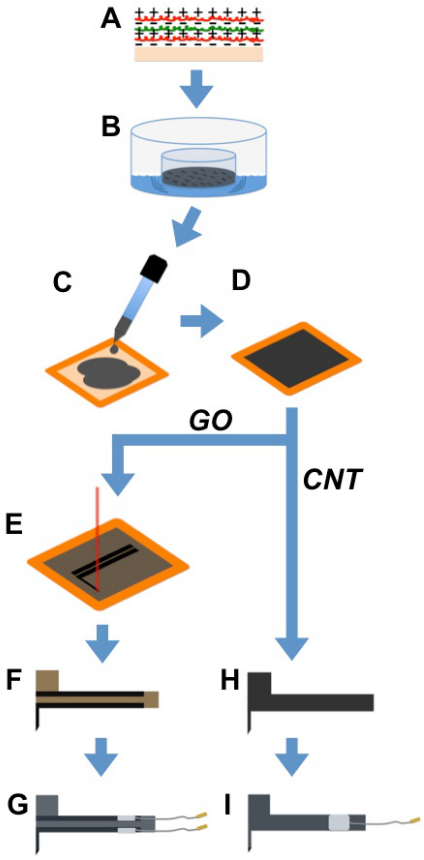

Figure 3.1. *Electrode fabrication flowchart. (A) A polymer substrate is prepared for electrostatic adhesion of nano-structured carbon with layer-by-layer surface treatment. (B) Carbon nanotube (CNT) or graphene oxide (GO) dispersion is prepared with appropriate treatment and ultrasonic agitation. (C) The dispersion is drop cast on the substrate, and (D) allowed to dry into a thin film. For GO, (E) the GO film is laser treated to create conductive reduced graphene oxide (rGO), and is then (F) cut out and the (G) wire and pin are attached prior to PDMS insulation. For CNT, (H) the electrode is cut out without additional treatment and (I) a wire and pin are attached to electrode prior to insulation with PDMS.*

wire leads were attached to this far end with conductive silver epoxy. The electrodes were insulated with polydimethylsiloxane (PDMS; Sylgard 184, Dow Corning, Midland, MI), leaving the recording tip exposed.

3.2.2 PHANTOM PREPARATION

In vitro artifact testing was performed with electrodes secured in agar filled phantoms. Agar, 2% by weight was prepared with deionized (DI) water. Liquid agar was poured around an electrode suspended in a cylindrical tube, and then allowed to cool to room temperature.

3.2.3 ANIMAL PREPARATION

Electrodes were implanted in male Sprague-Dawley rats (N = 7, weight: 320±17 g). Anesthesia was induced with 5% isoflurane, and then lowered to between 1.5 and 3% isoflurane for the duration of the surgery and experiment. Animals were intubated and catheterized via the femoral artery prior to being placed in an MR-compatible cradle, and secured with bite and ear bars. A small craniotomy (<4 mm diameter) was performed over one hemisphere of the primary somatosensory forelimb cortex (S1FL). The skull was dried completely, and a plastic anchor was attached to the contralateral skull for electrode stabilization. The electrode was inserted into the cortex using a stereotaxic system, and dental cement was applied to secure the electrode and close the craniotomy (**Figure 3.2**). A wire was placed in the animal's nose as a ground for the neuronal recording.

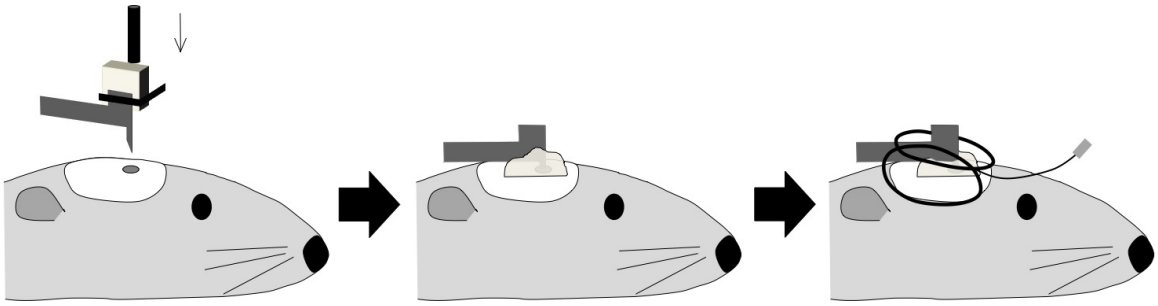

Figure 3.2. *Diagram of electrode implantation. Position and insert electrode into craniotomy with stereotaxic system. Secure electrode with dental cement. Place RF coil over dental cement and around the electrode.*

The animal's body temperature was maintained at 37ºC with a heated water pad. Artificial breathing was monitored and maintained for an exhaled CO_2 of 3.0 – 4.0%. Arterial blood samples were taken periodically to test blood glucose levels, pO_2, pCO_2, and pH. At the end of the study, a bolus of potassium chloride (KCl) was injected through a venous line to induce a heart attack. *Ex vivo* controls for each animal were collected for MRI and electrophysiology.

Three additional control animals were prepared with 2 bilateral craniotomies each. Two of these animals were used for MRI sham studies, including craniotomies with and without dura removal, as well as the insertion of a substrate-only electrode. One animal was used for a bilateral control bench study to compare signal from a commercial probe (NeuroNexus, MI) to a carbon nanomaterial electrode.

All animal procedures were approved by the Institutional Animal Care and Use Committee at the University of Minnesota.

3.2.4 MRI HARDWARE

The majority of experiments were performed on a 9.4T/31cm horizontal bore magnet with a VnmrJ console (Agilent, Santa Clara, CA). Custom RF coils, including a single-loop ^{1}H coil or a dual-tuned butterfly ^{1}H coil and single loop ^{31}P coil, were used. Multi-slice T_1-weighted gradient echo (GEMS) and T_2-weighted fast spin echo (FSEMS) sequences were performed to acquire whole brain anatomical images in sagittal, axial,

and coronal orientations with a resolution of 156.3 μm or 78.1 μm (FOV 40x40 mm, slice thickness 0.5 or 1 mm, 256x256 or 512x512 image matrix size). Functional imaging was acquired using single shot echo planer imaging (gradient echo EPI, TR 612 ms, TE 17 ms, FOV 40x40 mm, 64x64 voxels, slice thickness 1 mm, 1-3 slices).

3.2.5 IMAGING DATA ANALYSIS

All MRI images were loaded into MATLAB (MathWorks, Natika, MA) with the AEDES toolbox. Connectivity maps were calculated using a seed based correlation analysis and overlaid on slice matched anatomical images, with a threshold of $p < 0.05$ and $|cc| > 0.5$.

Apparent electrode widths were calculated based on anatomical imaging using the average of 6 manual measurements in ImageJ (Schneider *et al* 2012) (NIH, Bethesda, MD) and compared to 6 repeat measurements made at the same location in an image taken with a digital microscope (VHX-5000, Keyence, Itasca, IL).

3.2.6 NEURONAL RECORDING

Continuous neuronal signal was recorded at 30 kHz using a Cerebus data acquisition system (Blackrock Microsystems, Salt Lake City, UT). Control time courses were acquired when no MR acquisition was in progress. Noise filtering (60 Hz) was applied during post processing in MATLAB. No change in noise floor was found when recording near the MRI scanner, likely a result of the Faraday cage environment the

electrode was in. However, some effects on the online spike sorting algorithm were found when using a signal simulator, with noise signals being sorted into the spike sets.

Breathing artifacts were removed with in-house MATLAB code based on physiological recordings, and low-pass filtering was performed to isolate local field potentials (LFPs, <500 Hz).

MR-induced artifacts were removed using custom code in MATLAB utilizing the sequence repetition to generate a sliding window high-average artifact template. This template was then subtracted from the data after alignment to each artifact. This method is similar to that developed by Niazy *et al* (Niazy *et al* 2005) and Mirsattari *et al* (Mirsattari *et al* 2005) for human EEG data.

3.2.7 STATISTICAL ANALYSIS

Values are given as *mean* ± *standard deviation*. Significance was set for $p < 0.05$.

3.4 RESULTS

3.4.1 ELECTRODE IMAGING ARTIFACTS

While these prototype electrodes are larger than commercial wire or linear array electrodes, as well as than the desired size for chronic studies, the large distinct profile allows for the clear investigation of the minimal susceptibility artifacts induced. *In vitro*, clear edges of the electrode's shape can easily be identified in 3 directions (**Figure 3.3**A), matching the shape as observed with a microscope image (**Figure 3.3**B). A side profile of implanted electrodes was distinguishable for almost all animals, such as can be seen in **Figure 3.4**, unless the electrode was implanted out-of-plane. **Table 1** shows the measured electrode side profile width for an optical microscope image compared with in vivo GEMS and FSEMS apparent width. Despite the optical images being acquired prior to insulation, the average difference from the optical measurement was only 149 μm for GEMS and -57 μm for FSEMS, where the negative value indicates that electrodes appeared smaller than their physical size. As the MR imaging resolution was 78 μm, these differences were 2 and -1 pixels, respectively. These measurements were also repeatable across scans (E1 in **Table 1**).

In general, the anatomical imaging void created by the nano-structured carbon electrodes was limited to partial volume voxels at the electrode location. In contrast, a silver wire and a tungsten electrode, both standard neuronal recording materials, each created an imaging void larger than their physical size, as well as a dipole artifact much

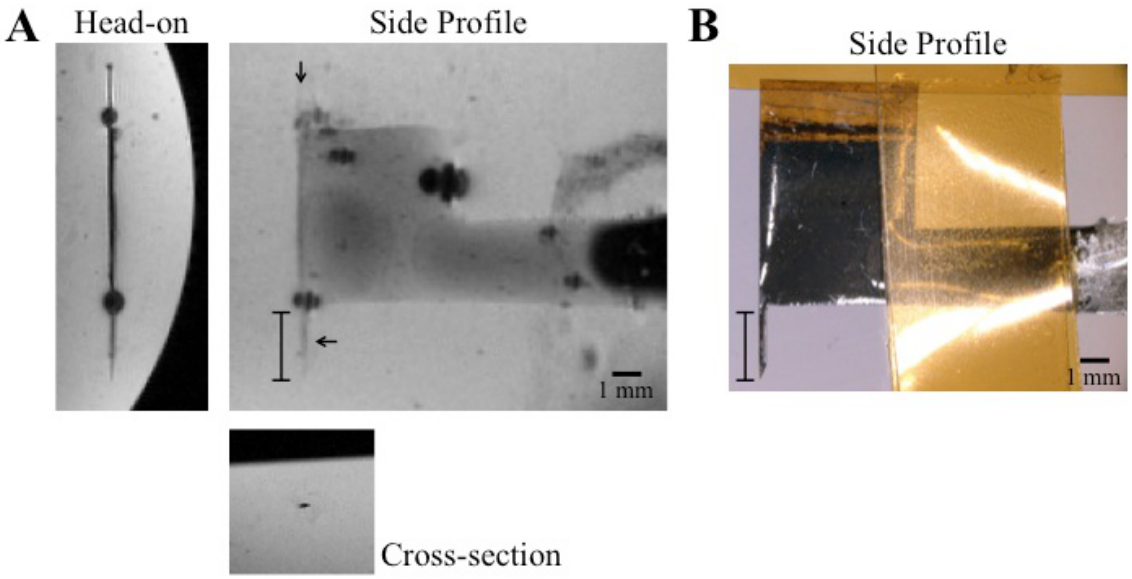

Figure 3.3. *Example electrode profile. (A) Three orientation images of electrode embedded in agar phantom, arranged as projections, with arrows indicating the projection slice locations. (B) The optical image of same electrode, to scale. Only the lower tip of the electrode (cross-bar in side profile) is inserted into the brain. Notice the clean edges of the electrode tip. The black dipole voids are from air bubbles that attached to the insulation during phantom preparation.*

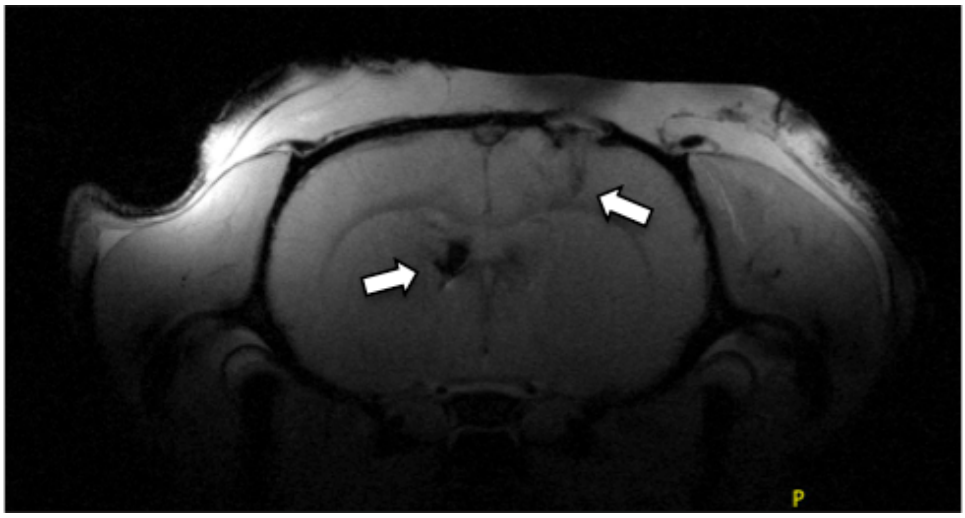

Figure 3.4. *Example T_1-weighted image of a CNT electrode side profile (top right) in vivo. The profile of the electrodes shows a clean angled insertion tip. Also observable is a large metal wire artifact in the left side deep brain region.*

Table 1. *Apparent width of electrodes determined by in vivo MRI at 9.4T (unless otherwise notes) and an optical microscope. Electrode images were each measured in the same location 6 times with ImageJ and reported as mean ± std. A single pixel in these anatomical images is 78 µm x 78 µm.*

Electrode	Scope (µm)	GEMS (µm)	Δ (µm)	FSEMS (µm)	Δ (µm)	Nano-Material	Substrate
E1	669 ± 5	964 ± 42	*295*	620 ± 38	*-49*	rGO	PET[§]
E1[†]		980 ± 34	*311*	614 ± 10	*-55*		
E1[†] (16.4T)		1061 ± 36	*392*	676 ± 39	*7*		
E2	570 ± 4	705 ± 48	*135*	276 ± 27	*-294*	rGO	PET[§]
E3	341 ± 5	341 ± 45	*0*	-	*-*	CNT	PI
E4*	714 ±7	1029 ± 109	*315*	832 ± 81	*118*	rGO	PI
E5	492 ± 5	426 ± 42	*-66*	459 ± 24	*-33*	rGO	PI
E6*	401 ± 5	729 ± 101	*328*	394 ± 27	*-7*	CNT	PI
E7	445 ± 8	484 ± 30	*39*	336 ± 31	*-79*	CNT	PI
Mean			*149*		*-57*		

[†] Phantom measurement, excluded from average

[§] Substrate material (PET) induces a shadow artifact in T_1-weighted (GEMS) images at ultrahigh magnetic fields

* Air bubbles in insulation induced large artifacts

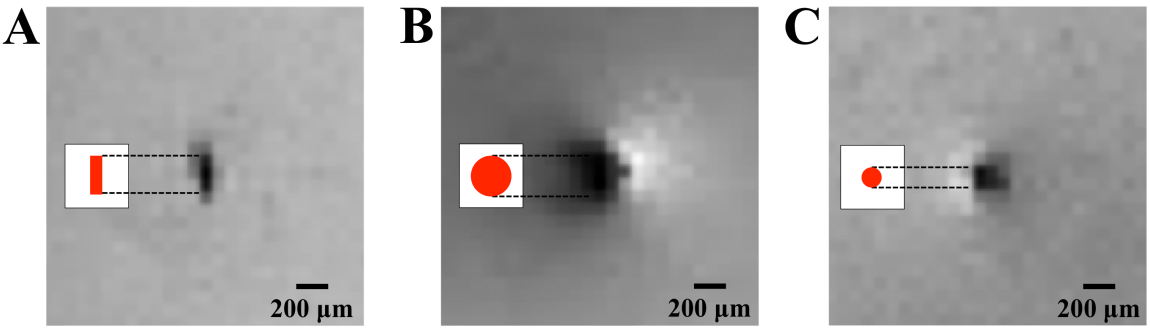

Figure 3.5. *Phantom cross-section MR anatomical images of a (A) CNT electrode on PI, with dimensions 243 µm x ~77 µm, a (B) silver wire of diameter 254 µm, and a (C) tungsten multi-unit recording electrode of diameter 127 µm. Each insert shows a red, scaled representation of the physical electrode size. Notice the large dipole artifacts around the silver (B) and tungsten (C) electrodes.*

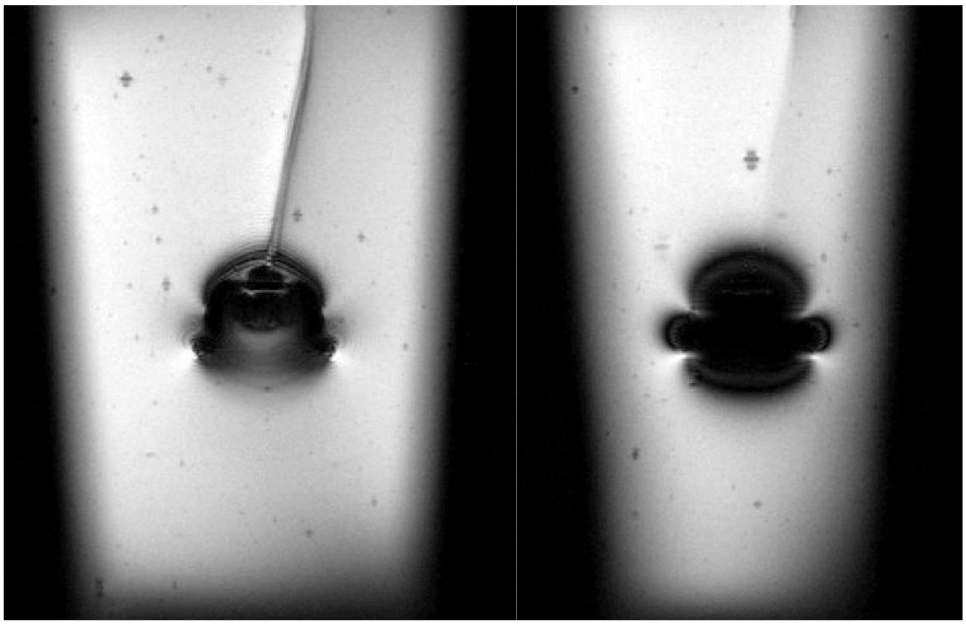

Figure 3.6. *Example of a large MRI susceptibility artifact due to a cylindrical EEG pellet electrode in two adjacent slices of a T_1-weighted image.*

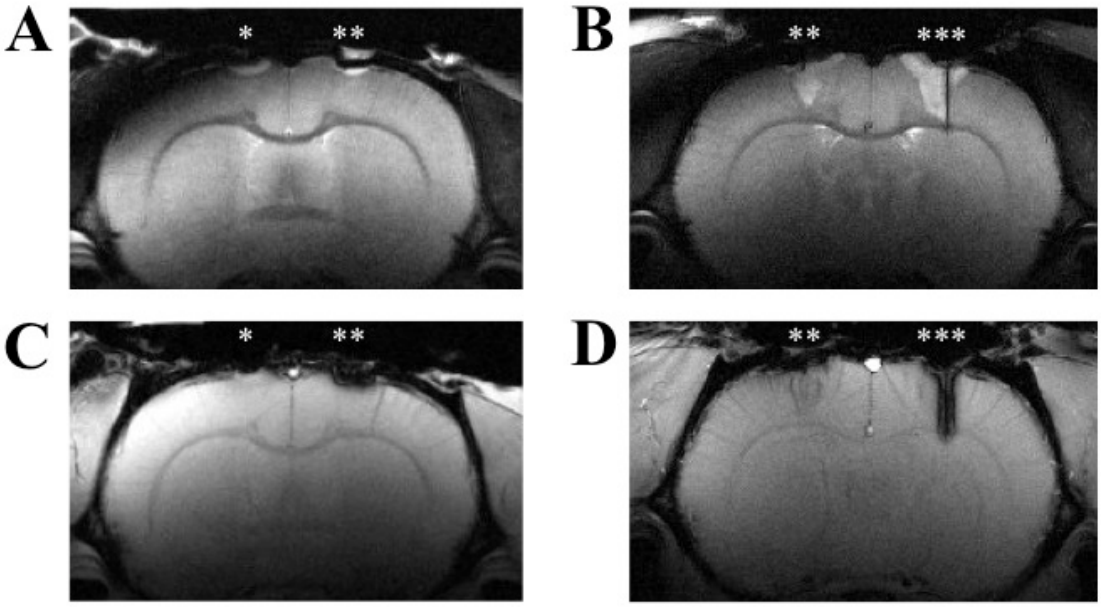

Figure 3.7. *Sham experiments to investigate observed T_2-weighted (FSEMS) hyperintensity. (A) Symmetric craniotomies on the left hemisphere without (*) and on the right hemisphere with (**) dura removal. (B) Symmetric craniotomies in a separate rat with dura removal (**) in the left hemisphere, and right hemisphere dura removal and polymer-only (PET) sham electrode insertion (***). (C-D) Matching T_1-weighted (GEMS) images show no tissue abnormalities. Due to the lack of conductive material in the sham experiments, the hyperintensity is not due to an electrically induced lesion. The observed tissue abnormalities under all sham conditions points to local swelling as a potential cause, but further investigation is needed. (D) A shadow artifact around the sham PET-based electrode is visible in the T_1-weighted image but not the T_2-weighted image (B). This artifact does not occur with PI base material.*

larger than itself (**Figure 3.5**). In the example cylindrical pellet electrode in **Figure 3.6**, a worst-case magnetic susceptibility artifact can be seen to create a very large dipole void around the electrode.

A hyperintensity was observed in T_2-weighted FSEMS images around the electrode in some animals, while no abnormalities appeared in the more commonly used T_1-weighted GEMS images. Comparison to a sham animal revealed the same issue when a sham electrode made of only base material was implanted (**Figure 3.7** B vs. D), therefore eliminating electrical lesioning as a cause. Although smaller, a similar effect was seen in a sham study with no electrode, both with and without dura removal (**Figure 3.7**A vs. C). While further investigation is required, we hypothesize that the hyperintensity is due to local swelling from the craniotomy itself.

3.4.2 FUNCTIONAL IMAGING ARTIFACTS

The EPI sequence is known for being highly sensitive to susceptibility artifacts, becoming unusable in the presence of a large magnetic field inhomogeneity. As seen in **Figure 3.8**, minimal distortion is observed in multi-slice EPI with our nano-structured carbon electrodes in most cases. Exceptions were typically related to bubbles in the electrode insulation or trapped in the craniotomy. In addition to a lack of streaking artifacts in the phase encode direction, the brain outline generated from the anatomical

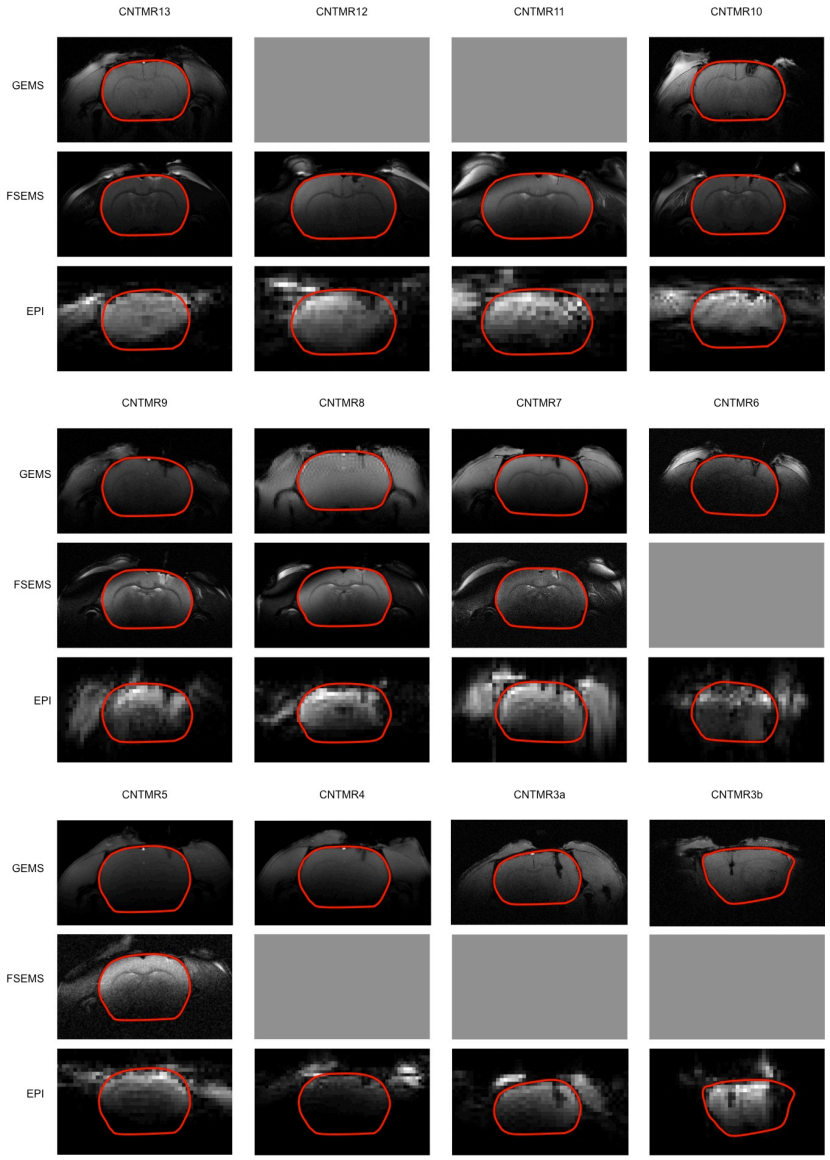

Figure 3.8. *Anatomical vs. EPI imaging for all animals(top labels). Note some differences between GEMS and FSEMS images. Outlines from the anatomical images match the EPI brain well in most cases.*

data shows good alignment with the raw unfiltered EPI images. Using this multi-slice fMRI data, neuronal networks can be calculated in the same slice as the electrode.

3.4.3 NEURONAL SIGNAL VERIFICATION

Outside of the scanner, data was acquired bilaterally in the S1FL cortex of a quality control rat. Recordings were performed in one hemisphere with a commercial linear array electrode (NeuroNexus, MI), and in the other with a CNT electrode. The animal was placed at an anesthesia depth of 1.7% isoflurane to produce a global neuronal burst suppression state, which we have investigated previously (Liu *et al* 2011). Visual comparison of the commercial and CNT electrode signals reveals highly similar temporal dynamics (**Figure 3.9** A vs. B), with some additional frequency information in the CNT trace, as highlighted by frequency domain comparison in **Figure 3.9**C. *Ex vivo* signals for each channel were also collected to emphasize the reduced noise floor in the CNT electrode trace. The SNR, calculated as burst amplitude versus noise amplitude, was 22 for the CNT electrode and only 6 for the commercial electrode. Another example of a simultaneous traditional and CNT recording can be seen in **Figure 3.10**, showing the same increased SNR in the CNT trace. No signal quality degradation was observed during the MR scanner studies, which lasted up to 8 hours post-implantation.

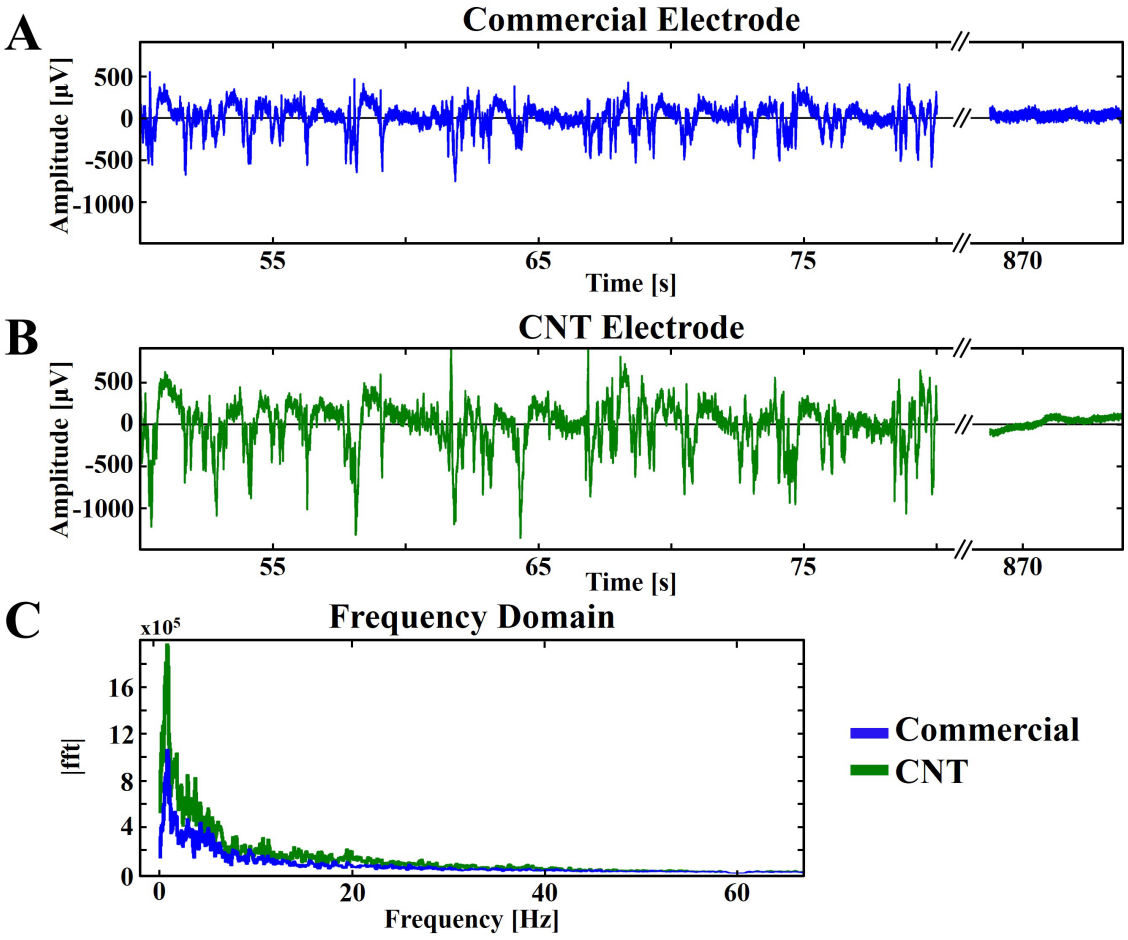

Figure 3.9. *Simultaneous bilateral comparison of local field potential bursts from a (A) commercial linear array probe and a (B) CNT electrode under 1.6% isoflurane in time, as well as an ex vivo noise floor (right side after axis break). (C) A comparison of the frequency profiles of the CNT electrode (green) and commercial electrode (blue).*

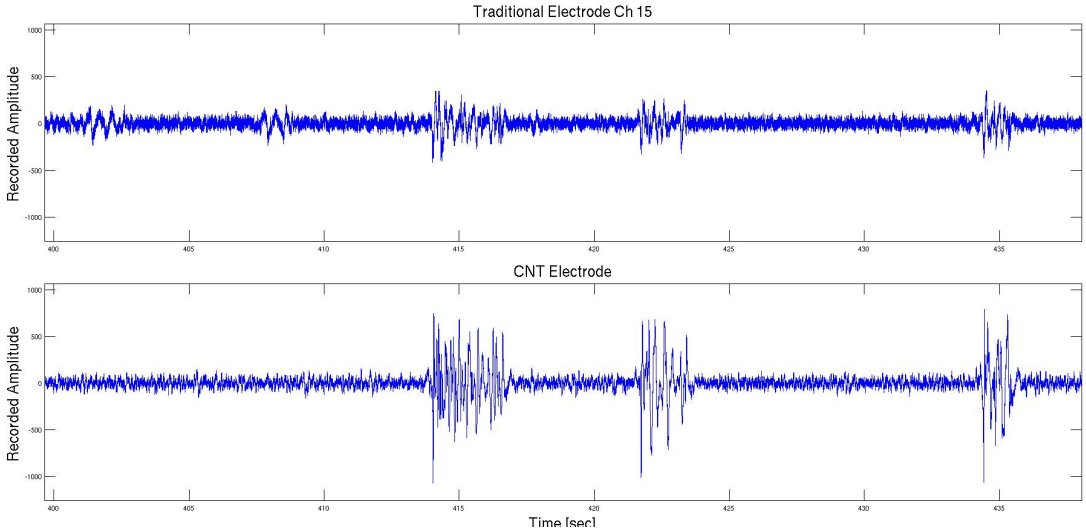

Figure 3.10. *Example in vivo comparison of a commercial (top) and CNT (bottom) electrode recording in somatosensory cortex. Both electrodes captured the LFP bursts, with superior SNR in the CNT electrode.*

3.4.4 NEURONAL RECORDING ARTIFACTS

During MR acquisition, the RF and gradient induced electrical artifacts obscure the neuronal activity. However, if the recording amplifier is not saturated, the signal can be recovered during post-processing. We were able to remove the fMRI-induced artifacts to the level of the neuronal bursts or lower, finding that for our data sets minimal saturation occurred during the EPI RF excitation pulses, and signal recovered quickly. In **Figure 3.11**, it can be seen that the burst amplitude and temporal distribution is unchanged by the artifacts.

These MR-induced artifacts are most commonly encountered when measuring EEG during an fMRI scan. The RF pulses and gradient changes to acquire the fMRI images generate repeating artifacts in the EEG traces that differ on each channel and obscure the brain activity. While many approaches have been used to remove the artifacts, a comparison of removal methods performed by Grouiller *et al* found that a template subtraction method was the most optimal for minimizing residuals with the least brain activity signal degradation (Grouiller *et al* 2007). Both Allen *et al* and Niazy *et al* implemented versions of a template subtraction model with the addition of adaptive noise canceling in order to remove both gradient and ballistocardiographic artifacts (Allen *et al* 2000, Niazy *et al* 2005). Subtracting signal from a reference EEG electrode located close to the recording electrode allowed a 70-100% reduction of artifacts by Mirsattari *et al*, facilitating real time seizure monitoring during fMRI or MRS (Mirsattari *et al* 2005). The

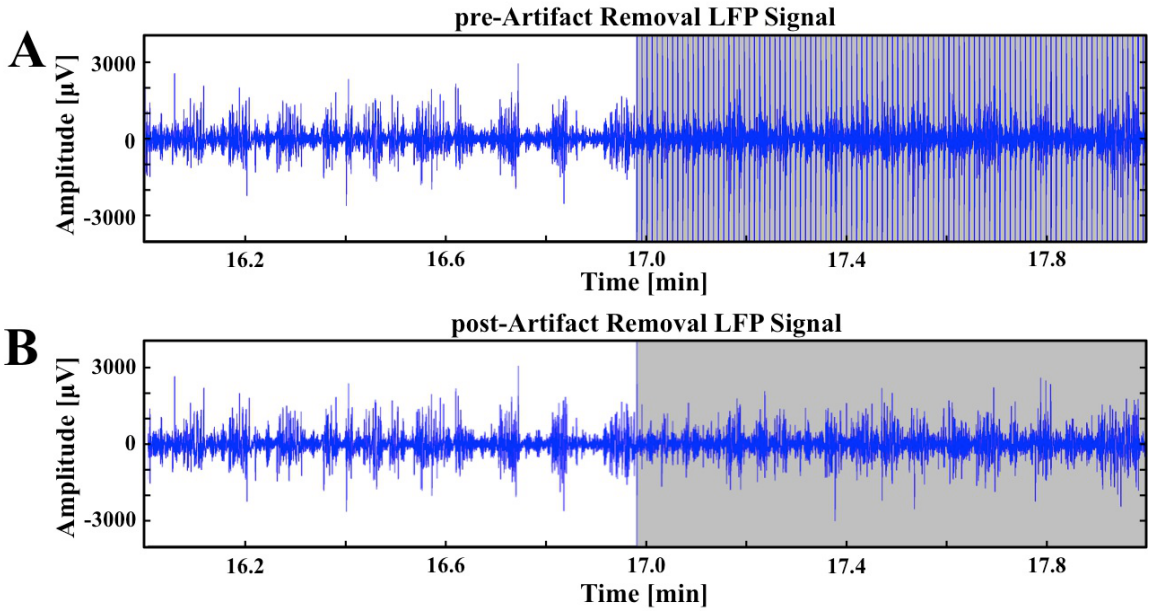

Figure 3.11. *LFP trace during fMRI acquisition (grey background, right side) using E2, (A) before and (B) after MR-induced artifact removal. Notice that the LFP burst amplitude, duration, and frequency is comparable during the control period and post-artifact removal.*

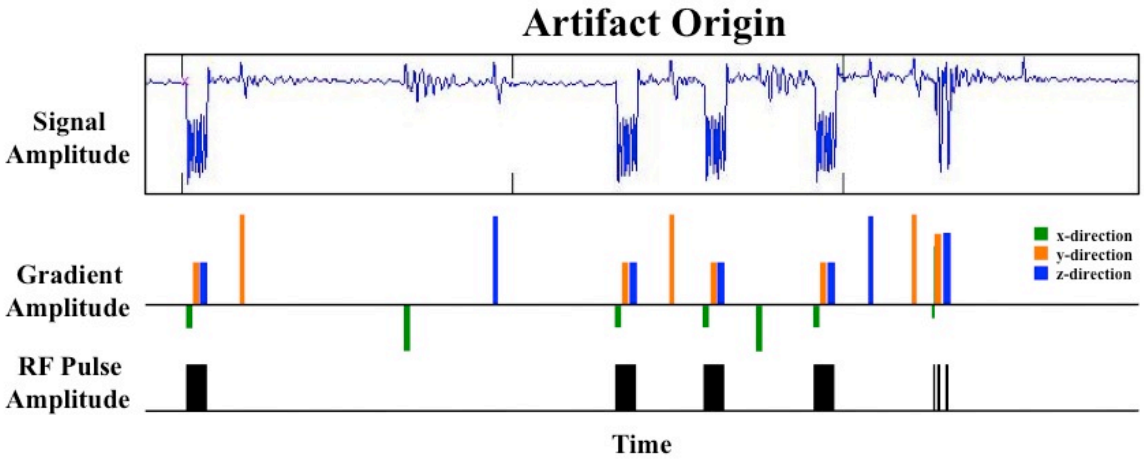

Figure 3.12. *Artifact comparison of recorded signal and ^{1}H PRESS sequence gradients and RF pulses. The largest artifacts line up with the RF pulses, with gradients inducing smaller but direction-dependent artifacts.*

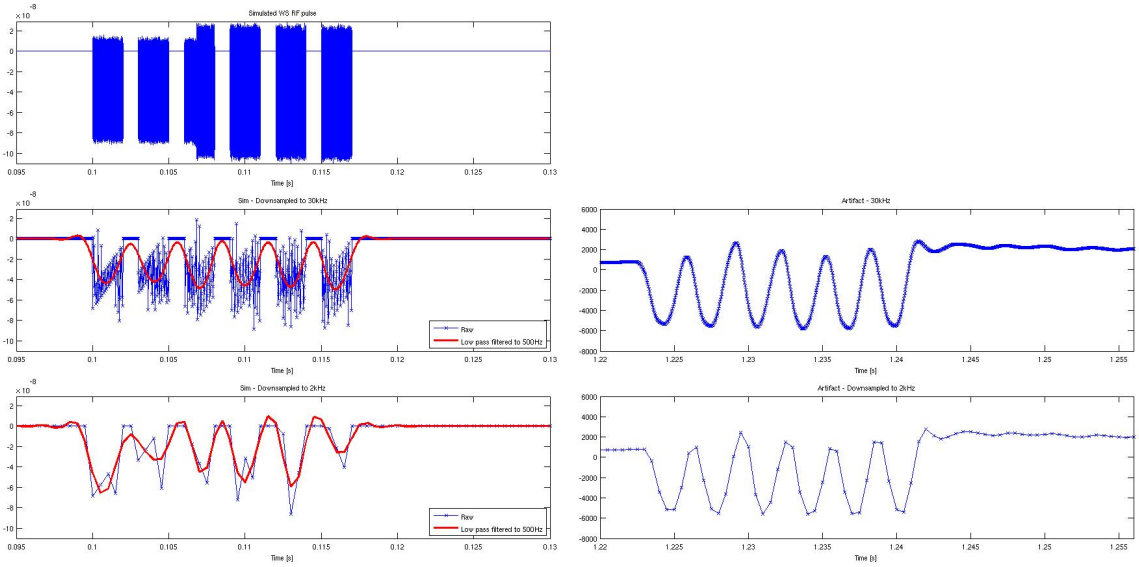

Figure 3.13. *Modeling the RF artifacts generated in the electrode reveals that following downsampling and filtering, a 6 square pulse train from* ^{1}H *PRESS (left) generates a signal which is highly similar to that recorded in vivo (right). The major difference is a slight post-stimulus ring in the in vivo data.*

high correlation between the sequence RF pulses and gradient modulation with the MR-induced artifacts can be seen in **Figure 3.12**. Preliminary analysis reveals that the artifact can also be modeled based on knowledge of the sequence itself. For example, down-sampling and filtering a simulation of the 6 square pulses which make up the voxel selection in PRESS results in a curve that is highly similar to the recorded artifact (**Figure 3.13**).

3.5 DISCUSSION

Nano-structured carbon electrodes, here made with CNT or rGO, show very limited anatomical artifacts and do not produce susceptibility artifacts to distort the highly sensitive EPI fMRI images. In T_1-weighted images, the average difference between the apparent electrode width and the optically measured width is less than 2 pixels in high-resolution imaging (40 mm FOV, 512 x 512), which could occur from partial volume effects alone. The T_2-weighted fast spin echo sequence shows even less artifact, as electrodes appear smaller than their physical size. When the electrode and imaging planes were out of alignment, the apparent width reduced even further, and electrodes nearly vanished from the MR images. For example, electrode E2 appeared to be half of its actual width in the T_2-weighted images (Table 1). Due to the large size of the prototype electrodes, some signal dropout is observed in the EPI, but it remains localized to the physical location of the electrode. As the size of the electrodes is reduced,

the amount of signal dropout should be minimized, making the electrodes practically invisible.

The limited artifacts produced by CNT and rGO in anatomical and functional imaging sequences make these conductive nanomaterials excellent choices for use in MR studies. By using these carbon-based nanomaterials to create MR-compatible neuronal electrode prototypes, we have achieved truly simultaneous MRI and electrophysiology recording. While many currently published simultaneous recording setups are highly sensitive to RF-induced amplifier saturation (resulting in loss of neuronal signal and the need to extrapolate data) (Pan *et al* 2011), our CNT and rGO electrodes do not generally demonstrate this problem for fMRI sequences. As such, we were able to recover the neuronal signal during RF pulses and gradient changes, potentially due to the unique electrical properties of the CNT and rGO. During EPI sequences, the induced artifact and electrophysiology signal appear to summate linearly and reproducibly. A local reference electrode will enable signal processing to further reduce the MR-induced artifact, allowing for even more consistent artifact removal.

A few groups have previously developed MR-compatible electrodes. Carbon fiber based electrodes were tested by Shyu *et al*, Jupp *et al*, Dunn *et al*, and Duffy *et al* (Shyu *et al* 2004, Jupp *et al* 2006, Dunn *et al* 2009, Duffy *et al* 2015), however the results were mixed due to manufacturing inconsistencies, and no group tested the electrodes with EPI.

Martinez Santiesteban *et al* investigated the compatibility of commercial silicon array probes, finding the apparent size to be 7 times that of the physical electrode size (Martinez Santiesteban *et al* 2006). A glass electrode, similar to a patch clamp, was employed by Pan *et al* (Pan *et al* 2010). Instead of developing an MR-compatible electrode, Airaksinen *et al* employed the RASER fMRI sequence to eliminate artifacts from a stainless steel probe, which limited them to single slice acquisitions (Airaksinen *et al* 2010).

As far as we are aware, the works of Logothetis *et al*, Pan *et al*, and Airaksinen *et al* are the only other reports of electrophysiology recorded simultaneously with the fMRI acquisition. Logothetis *et al* developed a complex recording circuit that used 3 small coils to monitor and counter magnetic field changes to minimize MR-induced artifacts (Logothetis *et al* 2001). Pan *et al* was unable to recover signal during MR-induced artifacts, instead extrapolating over the region (Pan *et al* 2010). Airaksinen *et al* excluded the MR-induced artifacts from analysis (Airaksinen *et al* 2010).

Simultaneously acquired data provides a wealth of information that we have yet to explore. With simultaneous LFPs and BOLD, we can look at spontaneous activity as well as direct responses to a variety of stimuli, as well as how their correlations fluctuate in time and with anesthesia depth. Without limiting ourselves to the selection of less sensitive fMRI sequences and to avoiding the brain region near the electrode, these nano-

structured carbon electrodes make simultaneous recording compatible with a wide range of established protocols and experiment paradigms.

To broaden the potential impact of these electrodes, their biocompatibility and safety remains to be verified. Many groups have found these materials to be biocompatible, showing successful cell proliferation (Ryoo *et al* 2010). However, at least one group found time and concentration dependent toxicity of GO in cell culture (Wang *et al* 2010). Additionally, a graphene monolayer was found to prevent corrosion on nickel, silver, and copper (Prasai *et al* 2012, Reed *et al* 2012). GO was also found to have antibacterial properties when placed in culture with *E. Coli* (Akhavan *et al* 2010, Hu *et al* 2010). A wide variety of manufacturing methods may contribute to this discrepancy and further research is needed.

While larger than desired for *in vivo* recordings, these prototype nano-structured carbon electrodes prove the feasibility of truly simultaneous fMRI and LFP recordings with minimal artifacts. Future work will focus on reducing the physical size of these electrodes to that of commercially available electrophysiology electrodes, adding a reference channel to improve artifact removal, moving to multiple channel array designs, and optimizing for neuronal spike waveform detection.

We have shown that the conductive nano-structured materials CNT and rGO can be used in conjunction with polymer substrates to create truly MRI-compatible neuronal electrodes. These electrodes introduce limited susceptibility artifacts, resulting in un-distorted fMRI acquisition with sufficient quality to generate network maps, as well as to investigate temporal BOLD dynamics. MR-induced artifacts are removable from the LFP neuronal signal recordings, allowing truly simultaneous analysis of neural and hemodynamic signals. To our knowledge, this is the first demonstration of the use of these nanomaterials as MR-compatible electrodes, as well as one of only a few methods that can acquire clear EPI fMRI without inducing significant susceptibility artifacts. With these electrodes, a wide range of animal experiments exploring healthy and pathological conditions is possible.

Chapter 4 :

OCCLUSION ENERGETICS

This chapter is modified from an accepted manuscript:

Taylor, Jennifer M, Xiao-Hong Zhu, Yi Zhang, Wei Chen. "Dynamic correlations between metabolic, hemodynamic, and neuronal responses to whole brain occlusion." *NMR in Biomedicine*. Accepted. DOI: 10.1002/nbm.3408.

4.1 BACKGROUND

Dynamic magnetic resonance spectroscopy (MRS) provides a wealth of *in vivo* information about brain metabolic pathways, rates, and mechanisms that can be explored utilizing specific nuclear MRS. For example, anaerobic metabolism can be monitored via cerebral lactate (Lac) concentration information with proton (^{1}H) spectroscopy (Howe *et al* 1993, Kemp *et al* 1994, Malisza *et al* 1998). Phosphorous (^{31}P) spectroscopy reveals high-energy phosphorous metabolites including PCr and ATP, and possibly the oxidative phosphorylation rate of ADP for producing ATP in mitochondria (Ackerman *et al* 1980, Kemp *et al* 1994, Chen *et al* 1997, Du *et al* 2008).

To better understand the dynamic relationship between metabolic and hemodynamic changes in the rat brain in response to a pathophysiological change, we have applied a high temporal resolution multi-channel MRS pulse sequence, discussed in Chapter 2, to acquire dynamic ^{1}H and ^{31}P spectra simultaneously. From these information-rich signals, we measured the dynamic responses of Lac, PCr, ATP, pH, and blood-oxygenation-level-dependence (BOLD) to an acute 12-minute whole-brain ischemia using the 4-blood-vessel-occlusion (4BVO) model (Pulsinelli *et al* 1979, Sugio *et al* 1988) with a 32-second temporal resolution. Upon induction of occlusion, the cerebral Lac concentration increases as a byproduct of glycolysis, recovering slowly to baseline following reperfusion, while PCr decreases dramatically upon occlusion and recovers relatively quickly. Although these results match the findings of similar ischemia

models (Lowry *et al* 1964, Ljunggren *et al* 1974, Gyulai *et al* 1987, Bolas *et al* 1988, Rudin *et al* 1989, Schmidt-Kastner *et al* 1989, Chang *et al* 1990, Nagatomo *et al* 1995, Malisza *et al* 1998, Bainbridge *et al* 2014), increased temporal and spectral resolution at ultrahigh field allows us to observe a delayed *in vivo* ATP response after the onset of occlusion, and to assess the hemodynamic and metabolic changes of individual animals within a single measurement.

Correlations between neuronal activity, specifically local field potentials, and BOLD responses to a paradigm stimulus have previously been explored using simultaneous electrophysiology and functional MRI methods (Logothetis *et al* 2001, Scholvinck *et al* 2010). Metabolic activity should play a key role in modulating this link under ischemic conditions, but is either explored using *ex vivo* extraction methods or low-temporal resolution *in vivo* MRS. To connect metabolic, hemodynamic, and neuronal activity changes with high temporal resolution, neuronal activity in the rat cortex under the same occlusion and reperfusion protocol was recorded outside of the MRI scanner and correlated with MRS measures, including BOLD. This information was used to investigate the cross correlations of both fast and slow dynamic changes of brain metabolism, BOLD, and neuronal activity during and after 12 minutes of whole-brain ischemia with high temporal resolution.

4.3 MATERIALS AND METHODS

4.3.1 ANIMAL SURGICAL PREPARATION

Whole-brain ischemia was induced in male Sprague-Dawley rats (n = 10, weight: 260 – 400 g). The 4BVO preparation (Pulsinelli *et al* 1979, Sugio *et al* 1988) was performed in two surgeries 24 to 48 hours apart. In brief, both vertebral arteries were cauterized under sterile surgical conditions. Animals were recovered for 1 - 2 days in a warm cage with soft food available. Hydronic (balloon) occluders (Harvard Apparatus, Holliston, MA) were installed around the common carotid arteries following intubation and catheterization of the femoral artery and vein. The rats were placed in a supine position on a custom-made MR-compatible cradle, and immobilized with ear and bite bars. Occluders were inflated for 12 minutes to induce a reversible occlusion.

During surgery, anesthesia was induced with 5% isoflurane and then maintained at 2%. Animals were kept between 1.6 and 2.0% isoflurane for the entire measurement session. Body temperature was monitored with a rectal probe and maintained at 37°C with a heated water pad. Using a BIOPAC data acquisition system (Goleta, CA), blood pressure was monitored through the femoral artery catheter, and inhaled and exhaled O_2, CO_2, N_2O, and isoflurane levels were sampled and monitored from the intubation line during the entire experiment. Inhaled O_2 and N_2O were kept at a 40:60 ratio. Blood pressure was considered stable if it was constant for 10 minutes, and was 86 ± 26 mmHg

prior to occlusion on average. Arterial blood samples were analyzed to monitor pO_2 (158.6 ± 45 mmHg), pCO_2 (35.4 ± 9.5 mmHg), and pH (7.44 ± 0.07). At the end of the study, a heart attack was induced with a high dose bolus of potassium chloride (KCl) through the venous line.

Animals were split into a MRI/MRS group (4 first and 4 second occlusion data sets were collected across 6 animals) and an electrophysiology group (4 first occlusion datasets were collected across 4 animals). In addition to the occluder placement, two small (< 4 mm) bilateral craniotomies were performed on the electrophysiology group to expose the primary somatosensory rat forelimb cortex regions (S1FL) for bilateral placement of two linear array probes. Physiological measurements after surgery were not observed to be different from animals without craniotomies. All animal experiments were conducted according to the National Research Council's Guide for the Care and Use of Laboratory Animals, and under protocols approved by the Institutional Animal Care and Use Committee of the University of Minnesota.

4.3.2 OCCLUSION AND REPERFUSION PROTOCOL

To induce global brain ischemia, the bilateral occluders were inflated for 12 minutes. Changes in systemic blood pressure were used to verify the occlusion based on expectations from literature (Pulsinelli *et al* 1979, Tomida *et al* 1987). Data acquisition consisted of a 3-minute control period, a 12-minute occlusion, and a >30-minute reperfusion and recovery period. The occlusion was repeated 30-60 minutes later if the

animal's recovery blood pressure level was maintained for at least 10 minutes, was similar to baseline values (average drop 13 ± 32 mmHg), and if brain lactate returned to pre-ischemic baseline levels. After the completion of the occlusion study, the response to an induced heart attack (i.e., no blood circulation) and an *ex vivo* control (dead brain) were acquired.

4.3.3 MRI/MRS MEASUREMENTS

In vivo MR imaging and spectroscopy was acquired on a 9.4T/31cm horizontal bore magnet (Magnex Scientific) interfaced with a VnmrJ console (Agilent Technologies, Santa Clara, CA). A dual-tuned radio-frequency (RF) surface coil was used, comprised of a butterfly ^{1}H coil and single loop ^{31}P coil (12 mm x 20 mm oval).

As discussed in Chapter 2, we implemented a combined ^{1}H-^{31}P MRS acquisition similar to techniques previously shown (Eleff *et al* , Rudin *et al* 1989, Chang *et al* 1990, Price *et al* 1996, Meyerspeer *et al* 2007). Spectral SNR and temporal signal fluctuations between repeated measurements were verified for the multi-channel sequence acquisitions as equivalent to single channel acquisitions. For this study, the localized ^{1}H spectroscopy sequence PRESS (Bottomley 1987) (TR = 4 s, TE = 15 ms, voxel size: 5x4x5 mm^3) was combined with a global ^{31}P single pulse (SPULS) acquisition. A nominal 90° RF pulse was employed to optimize the ^{31}P signal detection from the rat brain. VAPOR water suppression (Tkáč *et al* 1999) was employed prior to the ^{1}H PRESS sequence, and localized shimming was performed with FASTMAP (Gruetter 1993).

Spectra were averaged over 8 acquisition blocks (i.e., N=8) to increase SNR, giving a final temporal resolution of 32 seconds. Data was excluded if high lipid contamination remained in the ^{1}H spectrum.

4.3.4 ELECTROPHYSIOLOGY RECORDING

Electrophysiology data was acquired continuously at a sample rate of 2 kHz using a Cerebus Acquisition System (Blackrock Microsystems, Salt Lake City, UT) on 64 channels across two 32-channel linear array probes (NeuroNexus, Ann Arbor, MI) to monitor field potential activity in primary somatosensory S1FL cortex. Noise and low pass filtering (500 Hz cutoff) was applied in postprocessing. Signal quality was visually verified during the experiment, and the suppression of neuronal bursting activity was used to verify a successful occlusion.

4.3.5 SPECTRAL ANALYSIS

Manual spectral phasing was performed in VnmrJ (Agilent Technologies, Santa Clara, CA) on a 5-minute averaged baseline spectrum for each rat (**Figure 4.1**A-B). Individual spectrum quality as well as temporal stability can be observed in the dynamic spectral trend responses to occlusion and reperfusion in **Figure 4.1**C,D. Spectral quantification was performed using custom MATLAB (MathWorks, Natick, MA) code. Based on the finding of stable creatine (Cr) concentration during and following occlusion by Nagatomo *et al* (Nagatomo *et al* 1995), a baseline total Cr concentration ($[Cr]_{total}$, including Cr and PCr) of 8.5 mM (Pfeuffer *et al* 1999) was used for the normalization

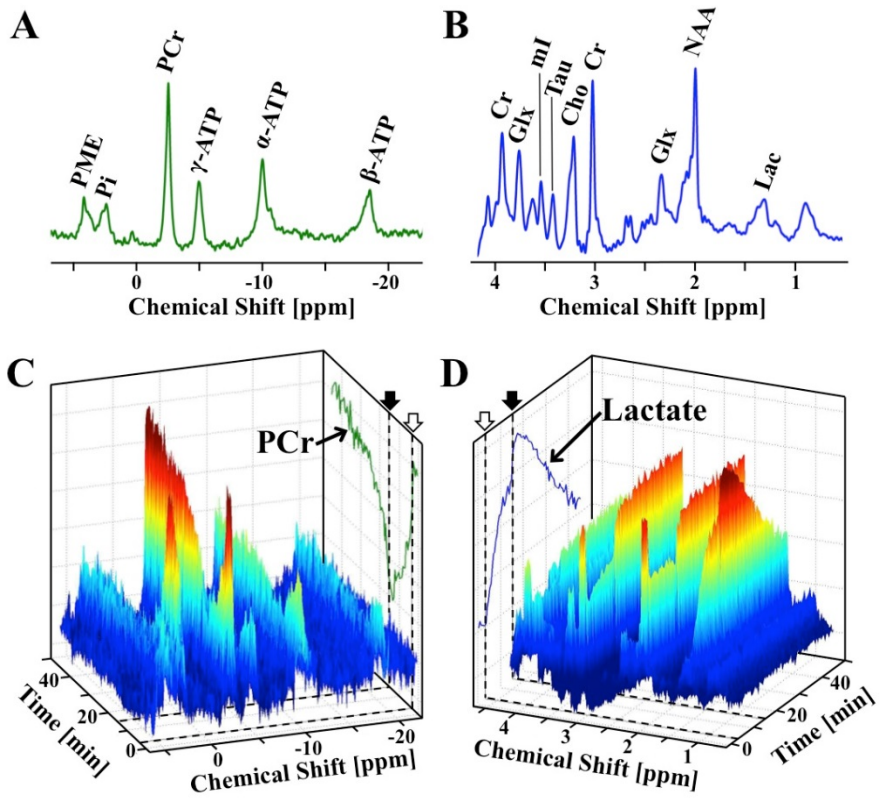

Figure 4.1. *Representative averaged ultrahigh-field baseline spectra for (A) ^{31}P and (B) ^{1}H from a representative rat brain, with major metabolites labeled. Spectral changes of dynamic (C) ^{31}P and (D) ^{1}H spectra during and following ischemia. Occlusion start (open arrow) and release (filled arrow) are indicated by dashed lines on (A, trace) PCr and (B, trace) Lac intensity projections. Temporal resolution is 32 seconds. The BOLD effect on the resonance linewidth and intensity is apparent in the NAA and Cr signals, as well as the lactate projection, particularly at occlusion onset and release.*

and quantification of [Lac], and the BOLD-effect was calculated from the percentage change in the linewidth of the Cr resonance at 3 ppm (Zhu *et al* 2001, Mangia *et al* 2006). Each ^{1}H spectrum was then corrected for this BOLD-effect prior to [Lac] quantification. To minimize lipid and macromolecule contributions in the [Lac] quantification, baseline ^{1}H spectra were averaged for each rat and subtracted from dynamic spectra measured during occlusion and post-ischemia reperfusion, as can be seen in **Figure 4.2**. The subtracted Lac peak was integrated to give changes in [Lac] (ΔLac, mM). Baseline [PCr] detected by ^{31}P MRS was normalized to 3.9 mM (Pfeuffer *et al* 1999), and Lorentzian fitting and integration was performed on the PCr peak (-2.5 ppm, **Figure 4.1** A) for the quantification of dynamic changes (ΔPCr, mM). While the global ^{31}P signal could include small contributions from the surrounding muscle, the entire signal was assumed to be dominated by brain tissue to simplify analysis.

Additionally, ^{31}P spectra were averaged at each time point across all 8 occlusions among the 6 rats in the MRI/MRS experiment group to increase SNR for reliable fitting of the γ-ATP resonance peak (-5 ppm, **Figure 4.1** A) and for the identification of changes in the chemical shift of inorganic phosphate (Pi). From these average spectra, group ΔPCr and ΔATP were quantified by integrating their respective spectral peaks. The intracellular pH values were calculated using the equation

$$pH = 6.75 + log\left(\frac{\Delta\delta - 3.29}{5.7 - \Delta\delta}\right)$$

where Δδ is the chemical shift difference in parts per million (ppm) units between the

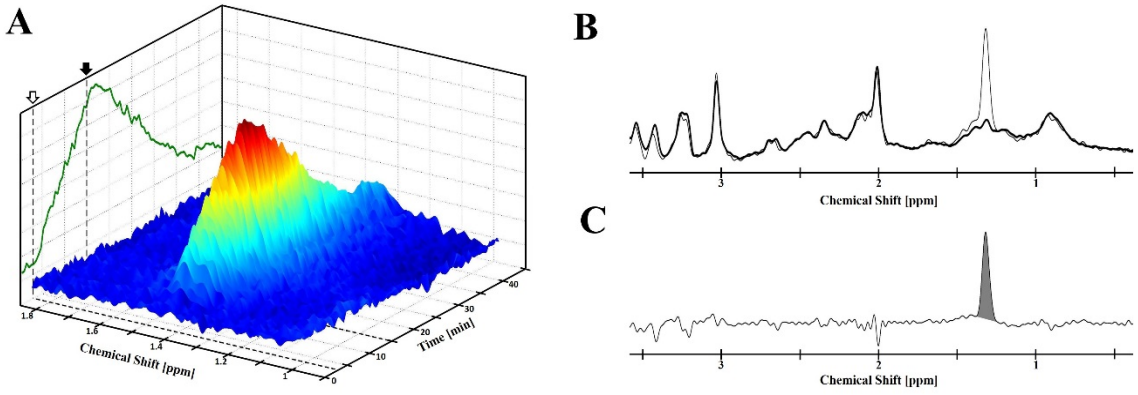

Figure 4.2. *Example lactate subtraction. Occlusion spectra subtracted from BOLD-corrected baseline spectrum to isolate changes in lactate. (A) Spectral time course response to occlusion (open arrow) and reperfusion (closed arrow). Projection of lactate peak maximum shown in green. (B) Baseline spectrum (thick line) overlaid on mid-occlusion, high lactate spectrum (thin line). (C) Subtraction of spectra in (B), with lactate integral indicated in grey. Negative peaks around 3.2 and 3.4 ppm show glucose depletion.*

PCr and Pi peaks (Bolas *et al* 1988). Justification for averaging across occlusions will be addressed in the **4.4 Results** section.

A coupled piecewise function consisting of a flat baseline and exponential occlusion and recovery phases was fitted to the temporal trend of each MRS metabolite of interest, following the equation

$$y(t) = \begin{cases} c_{Baseline} & 0 < t \leq t_1 \\ (a * exp(-k * t) + c)_{Occlusion} & t_1 < t \leq t_2 \\ (a * exp(-k * t) + c)_{Reperfusion} & t > t_2 \end{cases}$$

where t is time, k is a rate constant, a and c are offset constants, t_1 is the occlusion-induced-change start time, and t_2 is the reperfusion-induced-change start time. A reasonable delay following occlusion induction and release was allowed for the fitting of t_1 and t_2. A second recovery phase was added for pH to improve regression fit accuracy (Root-mean-squared-error, RMSE, of 1 Phase: 0.091 versus 2 Phases: 0.069). The high accuracy of the PCr and Lactate fits for each data set can be seen in **Figure 4.3**. Fitted Lac and PCr results from the same occlusion measurement were also plotted against each other to examine temporal trends.

4.3.6 ELECTROPHYSIOLOGY ANALYSIS

Continuous electrophysiology data was notch-filtered for 60 Hz noise prior to analysis. Time-frequency spectrograms (0 – 200 Hz) for each electrode channel were used to calculate signal power. Frequency normalization was performed to remove the 1/f power dependence (Demanuele *et al* 2007) and improve visualization of time-domain

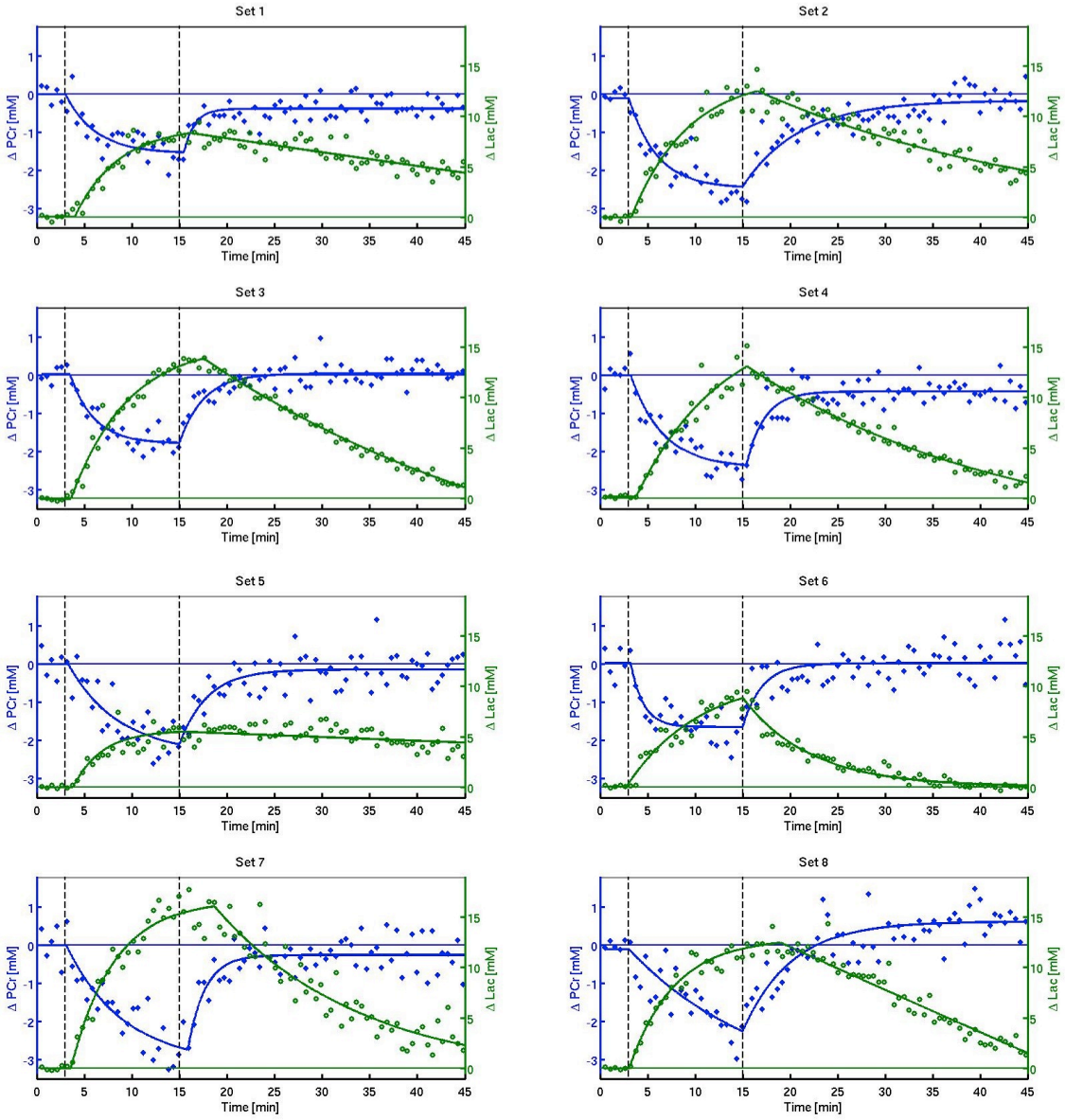

Figure 4.3. *Metabolic responses to occlusion and reperfusion showing ΔPCr (blue diamonds, left axis) and ΔLac (green circles, right axis) raw data (points) and regression fits (lines) for all data sets.*

dynamics. Multi-unit and spike activity were not analyzed here, as the deep isoflurane anesthesia level resulted in a very low spike detection rate. Temporal data was averaged across four frequency bands: 0 – 10 Hz (Low Frequency, LF), 10 – 30 Hz (Medium Frequency, MF), 30 – 58 Hz (Low Gamma, LG), and 62 – 200 Hz (High-Gamma, HG). For compatibility with the large brain volume MRS data, and utilizing the widespread, less specific neuronal connectivity found under deep isoflurane anesthesia (Liu *et al* 2011), the power of the field potentials was averaged across all channels within each rat. Traces were temporally smoothed with a 1-minute sliding window.

4.3.7 STATISTICAL ANALYSIS

Analysis values are given as *mean ± standard deviation* (SD). A linear mixed model was used when comparing the same metabolite to account for occlusion order, and correlations were used for comparing different metabolites time courses. Statistical significance was achieved for $p < 0.05$, unless otherwise stated. Correlation coefficients were considered highly significant for $|r| > 0.8$ and a $p < 0.001$.

4.4 RESULTS

4.4.1 MRS DATA QUALITY

Simultaneously acquired *in vivo* dual-nuclei ^{1}H-^{31}P MRS spectra have the same SNR as acquisition with traditional single-nucleus acquisition methods. The SNR and spectral resolution of our ultra-high field ^{31}P and ^{1}H *in vivo* spectra can be seen in

representative baseline spectra (**Figure 4.1** A,B, respectively). The temporal and spectra SNR of dynamically acquired data during an occlusion and reperfusion can be seen in **Figure 4.1** C and D for ^{31}P and ^{1}H, respectively.

4.4.2 METABOLIC AND BOLD RESPONSES TO ISCHEMIA

The 4BVO occlusion model produces a whole-brain ischemia, resulting in a large oxygen and energy deficiency in the rat brain. The occlusion onset immediately induces reductions in PCr and BOLD signals, and an increase in Lac (**Figure 4.1** C-D, **Figure 4.4** A-B). Reperfusion reverses these trends, although with a slower Lac recovery rate. Similar trends are observed upon heart attack induction and complete suppression of blood circulation, but with a larger PCr drop (**Figure 4.4** A) indicating that some energy reserves and residual blood flow remained during occlusion. In contrast, a relatively lower maximal ΔLac was generated by the heart attack and brain death as compared to the occlusion (**Figure 4.4** A), pointing to the depletion of glycogen reserves during the 12-minute occlusion.

Quantification of metabolic exponential regression rates (k from Eqn. 2) highlights differences in the PCr and Lac responses, as well as differences between occlusion, reperfusion, and heart attack. A distribution of these rates can be seen in **Figure 4.5**. The rate of PCr change for the occlusion ($k = 0.27 \pm 0.2$) was not statistically different from that of reperfusion ($k = 0.38 \pm 0.21$, $p > 0.05$). Lac reduced slower following reperfusion ($k = 0.04 \pm 0.05$, approaching linear) than it increased during

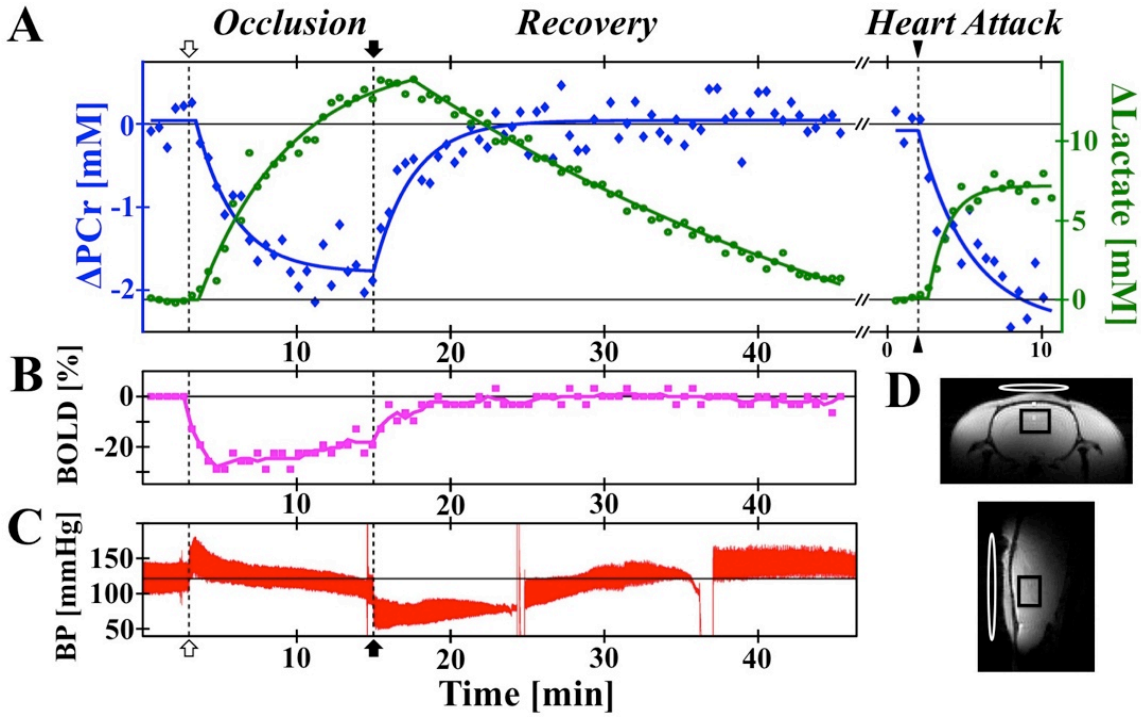

Figure 4.4. *Representative changes in (A) PCr (blue), Lac (green), (B) BOLD-effect (pink), and (C) blood pressure (red) during ischemia, reperfusion, and heart attack, with 32 sec temporal resolution. Solid traces in Lac and PCr indicate exponential regression fits. Occlusion start (open arrow), release (closed arrow), and KCl injection (triangle) indicated with dashed vertical lines. (D) Anatomical imaging in two orientations with black PRESS voxel and white* ^{31}P *single-loop coil (12 mm x 20 mm oval).*

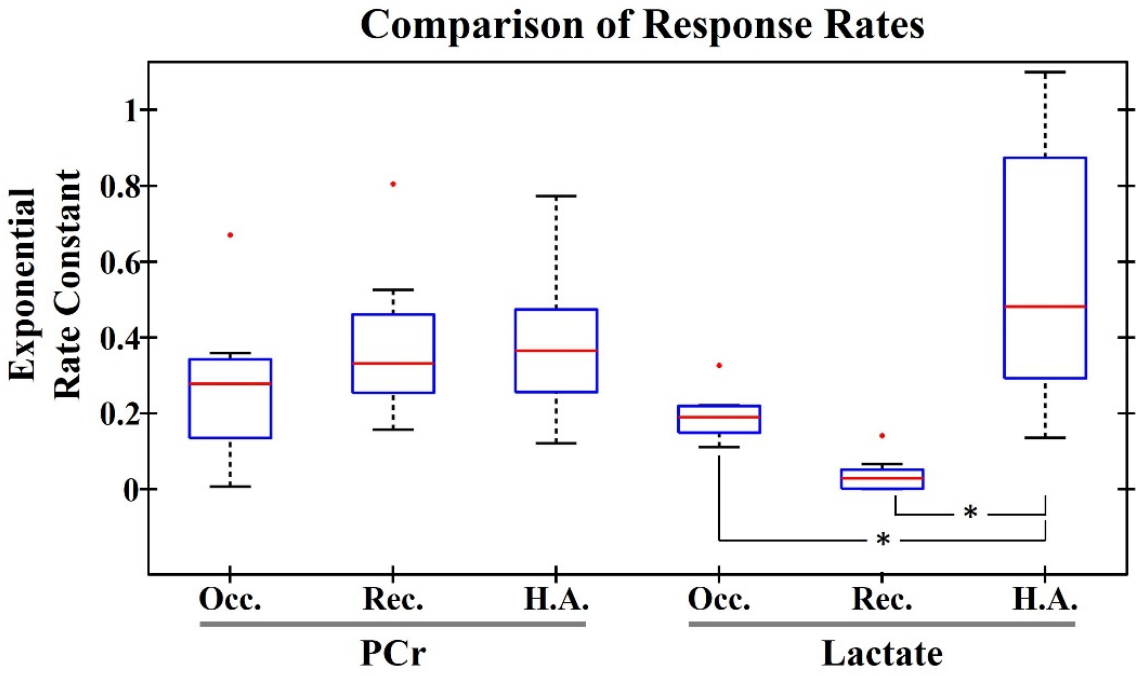

Figure 4.5. *Exponential rate constant boxplot comparison of individual PCr and lactate immediately following occlusion (Occ), recovery (Rec), and heart attack (HA). The equation* $y = ae^{k(t_0 - t)} + c$ *was used to fit each metabolic response, where k is the rate constant displayed. PCr recovery rate was similar to that of occlusion, with heart attack response being more variable. Lactate recovery was slightly slower than occlusion, with heart attack being significantly faster than both occlusion and recovery. *: Significance level of 0.05.*

occlusion (k = 0.19 ± 0.07), although the difference did not reach statistical significance. The difference in Lac responses between occlusion and reperfusion may result from the interplay between Lac transport across the blood brain barrier, the washout removal of excessive brain Lac, and possible cerebral Lac metabolism (Howe *et al* 1993). The significant increase in Lac production rate following heart attack induction (k = 0.57 ± 0.38, $p < 0.05$), compared with occlusion and recovery, highlights the presence of residual blood flow from peripheral vessels during occlusion in comparison with the complete absence of blood supply after the heart attack, as well as the response dependence on occlusion model.

The simultaneous nature of this ^{1}H-^{31}P MRS acquisition allows the analysis of PCr and Lac in the same rat within a single occlusion, previously assumed to have consistent trends across multiple rats. Analysis of simultaneous MRS data reveals that the individual PCr responses to occlusion and recovery were much more similar than Lac responses which showed more variation between inter-subjects, as seen in **Figure 4.6**. **Figure 4.7**A shows the time courses of the Δ[Lac]/[PCr] ratio for each rat. Within these ratio traces, two groups with different magnitudes of changes were observed. Performing a post-hoc linear mixed model test on the area-under-the-curve of the ratio traces, the two observed groups (Trend 1 and Trend 2) were determined to be statistically different (p = 0.001). Differences between these two groups are highlighted by plotting ΔLac versus ΔPCr correlation loops, viewed clockwise (**Figure 4.7** B,C), showing clearly that the

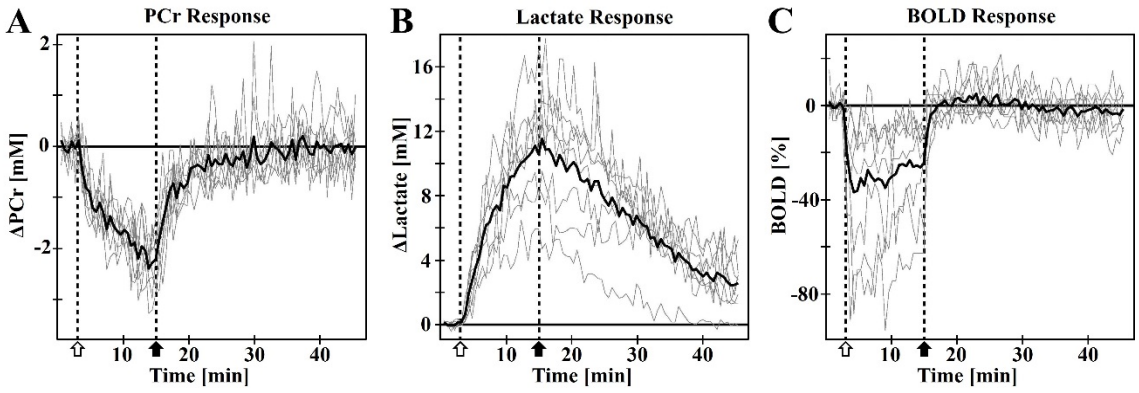

Figure 4.6. *Overlay of individual animal changes in (A) ΔPCr, (B) ΔLactate, and (C) BOLD induced by occlusion (open arrow) and reperfusion (filled arrow), with the thick line indicating multi-animal mean response. Notice that PCr is consistent within noise levels, whereas lactate and BOLD are highly variable.*

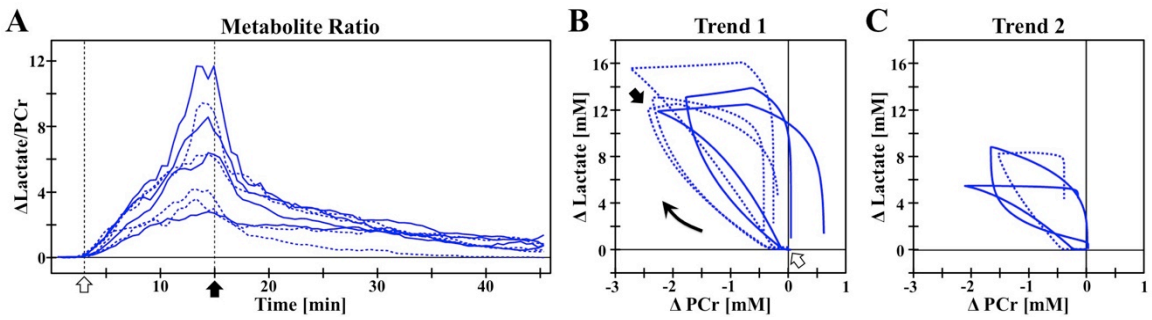

Figure 4.7. *Individual animal trends. (A) Temporal ratio of ΔLactate/[PCr] for individual rats for occlusion (open arrow) and reperfusion (closed arrow). Statistical comparison reveals two groups, whose dynamic correlation can be seen in the ΔLac versus ΔPCr plots for (B) Trend 1 and (C) Trend 2. The asymmetry of the correlation loop highlights the different temporal responses to occlusion versus reperfusion. First (solid) and second (dashed) occlusions indicated within each trend.*

trends were dominated by the larger Δ[Lac] variation among different rats. Notice that the correlation curves shapes are more consistent for the first trend than the second, as well as having smaller Lac and PCr overall concentration changes.

Considering the brain as a closed system during a complete whole-brain occlusion with no blood flow and thus no influx or efflux of nutrients including oxygen, glucose, and lactate, a simplified glycolysis metabolic model was employed to estimate the maximal Lac change resulting from the occlusion. Using the literature concentration values of 10 mM blood glucose, 2 mM brain tissue glucose, and 4 mM glycogen (Morgenthaler *et al* 2006, Du *et al* 2009), and approximating a 5% brain blood volume, it can be estimated that a maximum of 12.4 mM of Lac can be generated from the consumption of all available glucose and glycogen substrate pools in the rat brain (**Figure 4.8**). While in reality residual blood flow was present, the maximal Lac of 13.2 mM for Trend 1 is closer to this prediction than that of 7.8 mM for Trend 2. It is therefore hypothesized that occlusions in Trend 2 had reduced metabolic energy reserve pools of glucose and glycogen as compared to Trend 1. Blood glucose levels have previously been connected with increased ischemia impact (Ljunggren *et al* 1974, Duverger *et al* 1988, Hoxworth *et al* 1999), and it was observed that some rats remained lethargic following the initial surgery, and may have had low energy reserves, although weight loss did not correlate with final lactate results. Alternatively, Trend 2 occlusions may have had increased peripheral vessel blood flow, however a very small, non-significant correlation

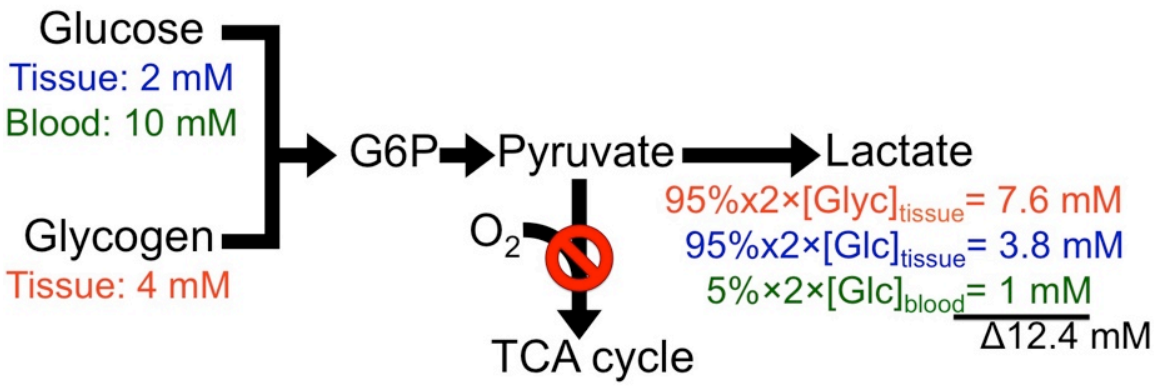

Figure 4.8. *Metabolic flowchart. The occlusion model creates a closed system with elimination of oxygen, resulting in a transition from oxidative to non-oxidative phosphorylation. Based on literature values of glycogen and glucose tissue and blood pools, and a conversion of 1 glucose-6-phosphate (G6P) → 2 lactate, we estimate an increase of ~12 mM lactate at the end of occlusion. An observation of 13.9 mM lactate increase in the average big-loop trend matches the estimation.*

coefficient of -0.23 ($p = 0.58$) between maximal changes in Lac versus BOLD does not support this notion. Further investigation is needed to distinguish the true metabolic basis for Trend 2.

4.4.4 ISCHEMIA INDUCED NEURONAL FIELD POTENTIAL RESPONSES

The temporal dynamics of the neuronal field potential response to occlusion reveal a rapid reduction in signal power across 0 – 200 Hz for the first 2 minutes of occlusion, with a small amount of recovery during the second half of occlusion in some electrode recording channels. Signal power recovers further following reperfusion but does not reach baseline levels. These changes are most easily observed in the example time-frequency spectrogram in **Figure 4.9**A. The deep 1.6-2.0% isoflurane anesthesia used here results in an unconscious state in the rat brain that exhibits burst-suppression EEG patterns (Liu *et al* 2011) (**Figure 4.9**B-a). Occlusion and reperfusion induced changes in burst signal amplitudes and duration in the temporal domain can be observed in **Figure 4.9**B, and match the trends seen in the average field potential power spectrum curves (**Figure 4.9**C). Field potential power following heart attack induction (dead brain representing the EEG background noise level, **Figure 4.9**B-d) can be seen to be substantially lower than occlusion (**Figure 4.9** B-b and C), again indicating the presence of some residual metabolic energy, blood flow, and neuronal activity during occlusion despite the lack of neuronal bursting. The field potential power amplitudes follow the order of baseline (highest), post-ischemia recovery, occlusion, and dead brain across frequencies below 60 Hz (**Figure 4.9**C).

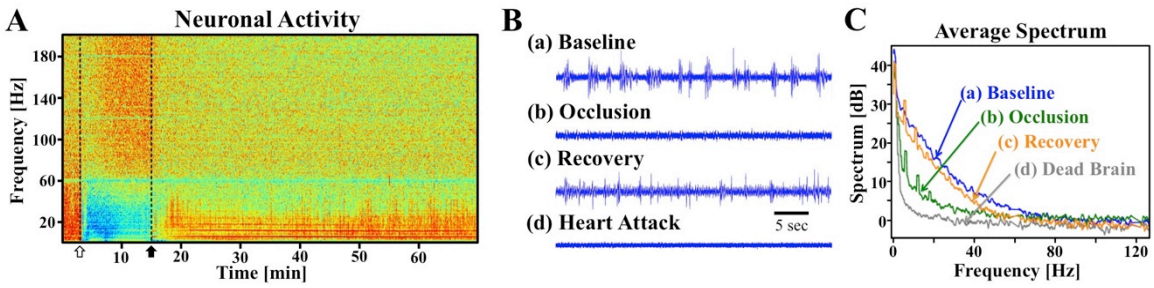

Figure 4.9. *Neuronal response. (A) Example time-frequency spectrogram for 0-200 Hz of field potential response to occlusion and reperfusion. (B) Filtered time course clips and (C) average power spectrum from (a) baseline, (b) 8 minutes following occlusion onset, (c) an hour after reperfusion, and (d) ex vivo. Power is calculated based on* $10*\log_{10}$ *of the amplitude of the spectrogram.*

4.4.6 GROUP COMPARISON OF METABOLIC, BOLD, AND NEURONAL RESPONSES

Beyond PCr, other energy molecules observable with ^{31}P MRS provide insight into cerebral energetics, but the SNR within the individual ^{31}P spectra of a single rat is insufficient for reliable quantification of low concentration metabolites such as Pi. Averaging the ^{31}P spectra at each measurement time point across all rats produced sufficient SNR for group quantification, comparison, and exponential regression fitting of cerebral PCr, ATP, and intracellular pH dynamics (**Figure 4.10** A-D). Group averaged PCr displays the same trend as individual rats, immediately dropping upon occlusion onset until reperfusion, and exhibiting a similar recovery rate to the baseline level during reperfusion.

While different vasculature responses and damage extent has been observed to result from repeated occlusions (Tomida *et al* 1987), no dependence on occlusion order was observed in the metabolic time courses of this study, presumably owing to a small sample size and mild impairment from the relatively short occlusion. Only a slight difference in the ΔPCr response to the first occlusion versus second occlusion was observed, where the maximum reduction by the end of the 12-minute occlusion period was slightly larger for the second than the first occlusion (**Figure 4.7** B). A linear mixed model with Bonferroni correction did not find a statistical significance between PCr responses of Occlusion 1 versus Occasion 2 ($p = 0.002$, Bonferroni significance at $p =$

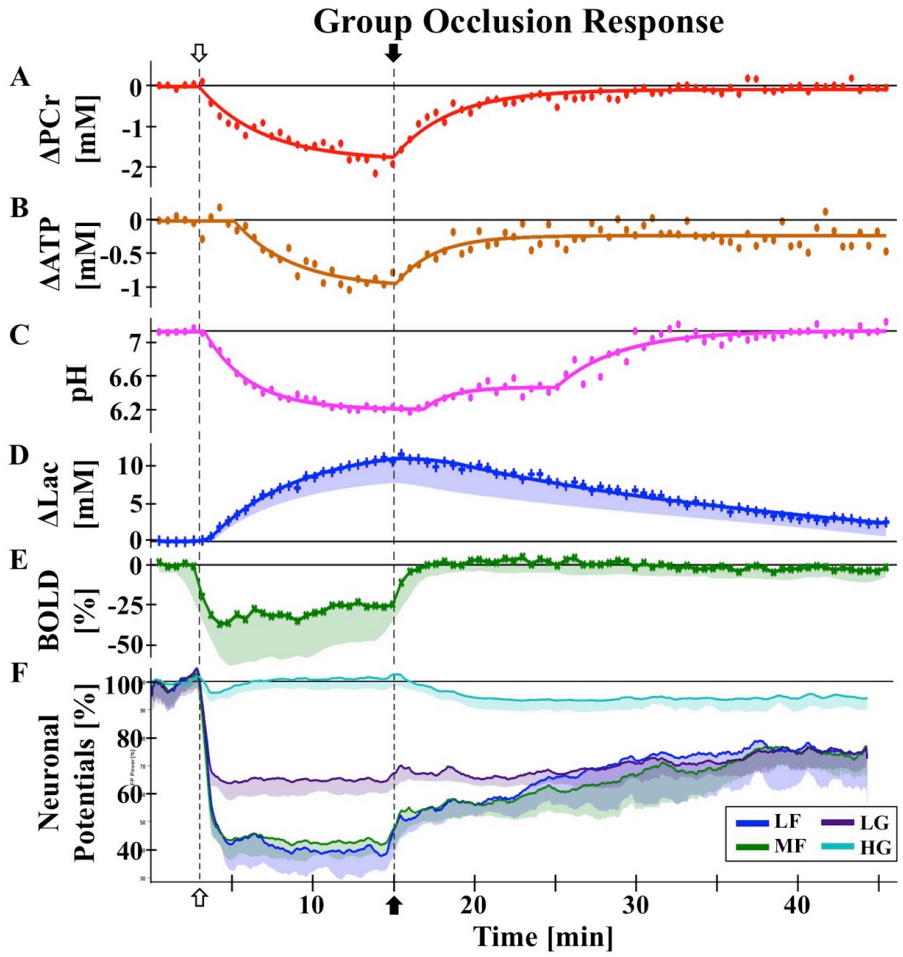

Figure 4.10. *Group responses to occlusion (open arrow) and reperfusion (closed arrow) with raw data (symbols) and regression fits (lines) for (A) ΔPCr, (B) ΔATP, (C) pH, and (D) ΔLac, raw data for (E) BOLD, and smoothed data (lines) for (F) neuronal field potential activity. (A-C) Values quantified from average ^{31}P spectrum. (D-F) Average of individual animal values, with shaded areas indicating one standard deviation (σ) from the mean. Field potentials were analyzed across 4 frequency bands: LF 0-10 Hz, MF 10-30 Hz, LG 30-58 Hz, and HG 62-200 Hz. Neither ATP nor field potential bands recover to baseline levels.*

$5.8e^{-4}$). Differences were only seen in the recovery phase (paired t-test, $p < 0.05$ for the initial recovery period of 20-35 minutes, $p > 0.05$ otherwise). These differences are consistent with a second occlusion that is metabolically slightly more severe than the first, as well as indicating the possibility of depleted glycogen reserves after the first occlusion. The reproducibility of the results can be seen in **Figure 4.6**. Averaging both occlusion responses together will slightly pull the data towards a middle range of occlusion severity, which given inter-animal variability and unknown residual perfusion, is still generally comparable. Results of other metabolite dynamics would therefore be slightly less severe than average for the first occlusion, and slightly more severe for the second occlusion.

Interestingly, ATP dynamics had a 2.2-minute delayed reduction response to occlusion, and the reperfusion steady state of [ATP] was significantly lower than baseline ($p = 8.3e^{-4}$), at 80% (**Figure 4.10** B). To our knowledge, this short delay in *in vivo* ATP response has not been previously reported in the literature due to the limited sensitivity and temporal resolution of *in vivo* ^{31}P MRS. In a decapitation model by Lowry *et al* (Lowry *et al* 1964), a plot of [ATP] and other metabolites shows ATP remaining near baseline for approximately 2 minutes in anesthetized mice, however this delay could be seen as noise in the data. They also found that adenylate kinase, an important enzyme in the ATP and ADP balance, did not begin to decrease and glycogen did not disappear until 2 minutes post ischemia. Indirect support of this delay can be also found in the brain slice

model used by Fleidervish *et al* (Fleidervish *et al* 2001), where an increase in ATP-sensitive potassium channel activation was observed 3 minutes into hypoxia, and large amplitude spontaneous spikes were gone by 2 minutes. Additionally, Raffin *et al* observed a 122 second latency, on average, of extracellular anoxic depolarization, which they linked to brain energy deprivation (Raffin *et al* 1991). Bainbridge *et al* found a change in ATP (referred to as NTP) decline associated with PCr reaching 1/3 of baseline values, however the time of occurrence appears to be much later than our results and the authors did not discuss or quantify this time point (Bainbridge *et al* 2014). These differences could be attributed to different animal and ischemic models.

As anticipated, changes in pH (**Figure 4.11**) were found to mirror that of Lac (**Figure 4.11**, $r = -0.86$, $p = 3e^{-25}$), responding immediately to occlusion, but with a delay of 1.8 and 1.5 minutes to reperfusion, respectively. Lac and pH trends diverged 10 minutes post-reperfusion, with pH following a distinct additional exponential recovery trend. This divergence time point matches when the recoveries of PCr and ATP concentrations recovered to a steady-state level (**Figure 4.12**B), and may be indicative of a complex but interesting relationship between the ATP energy reserves, cell acidity, and lactate concentration. In contrast to the metabolic responses, the average BOLD response (**Figure 4.10**E) reached a low steady state within 1 minute of occlusion, staying there until reperfusion, with a short (~2 minutes) recovery period back to baseline, and the BOLD change exhibited no strong correlation with other metabolites, presumably owing

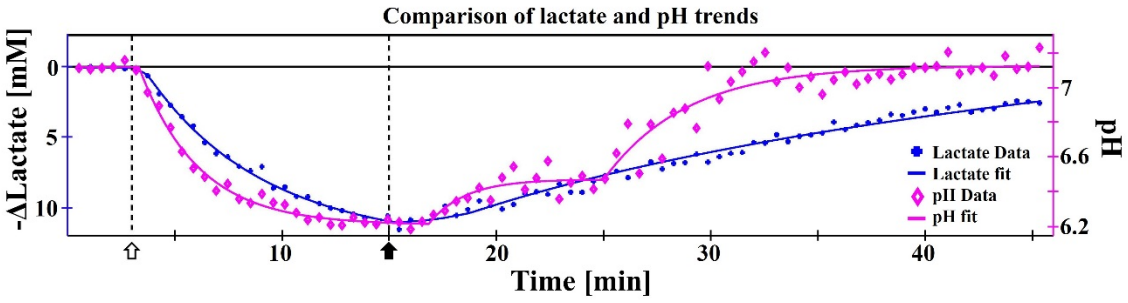

Figure 4.11. *Overlay of mean lactate and group pH response trends to occlusion (open arrow) and reperfusion (closed arrow), with the lactate y-axis reversed for visualization.*

to the distinct dynamics between the fast hemodynamic changes which dominates the BOLD signal and the relatively slow energy metabolite responses. While the overall trend of these metabolite changes match that previously found in separate literature studies (Bolas *et al* 1988, Rudin *et al* 1989, Chang *et al* 1990), the high temporal resolution and simultaneous ^{1}H-^{31}P MRS measurements reported here allow *in vivo* assessment of the short delays and dynamic correlations among metabolites and BOLD changes.

Multi-channel and multi-rat averaged responses of field potential spectral power were split into four frequency bands (see ***4.2 Materials and Methods***) to highlight group neuronal responses (**Figure 4.10**F and **Figure 4.12**). The field potential power in the LF and MF bands quickly dropped to 40% of baseline level upon occlusion, and to approximately 60% for the LG band, tightly linking neuronal activity to the reduced oxygen supply (Raffin *et al* 1991). Interestingly, despite this link and the band activity visually following the average BOLD dynamics (**Figure 4.10**E), only the LG band was found to correlate with BOLD ($r = -0.69$, $p = 4.3e^{-13}$). These activities reached a new low steady state within 2 minutes, around the same time as ATP began to be depleted (**Figure 4.12**A). The similar dynamics and time scales between the neuronal activity and brain ATP changes clearly suggest an essential role of cellular ATP availability in supporting neuronal activity and function, as well as neuronal impairment and dysfunction under the ischemic attack. The significance of the 2-minute delay is highlighted by an observation

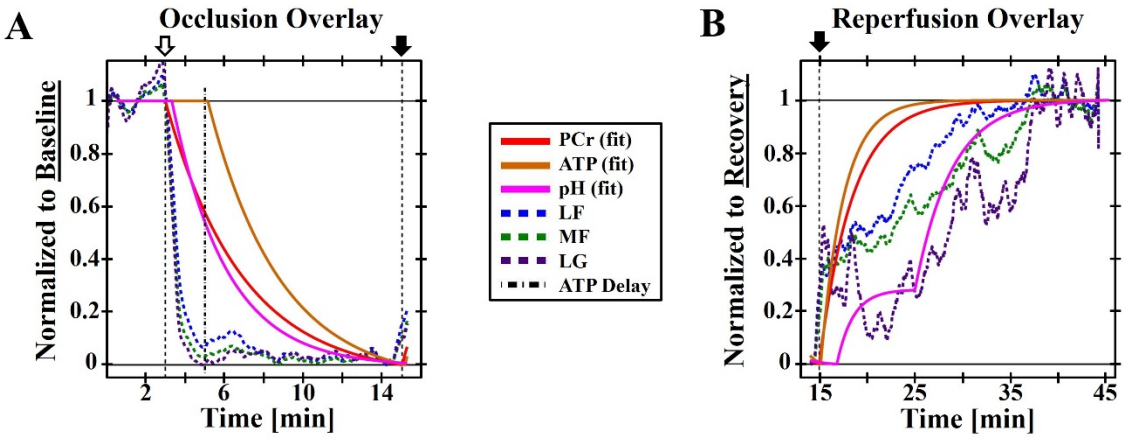

Figure 4.12. *Normalized comparisons. (A) Occlusion normalized comparison, highlighting the match in ATP response delay with low frequency field potential bands reaching a low steady state. (B) Reperfusion comparison normalized to recovery steady state showing the field potential recovery trend between the trends of pH and metabolites PCr and ATP.*

of Pulsinelli *et al* (Pulsinelli *et al* 1979), where awake animals became unresponsive with isoelectric EEG at 2-3 minutes following an occlusion using the same 4BVO model.

Interestingly, the changes in HG are much smaller, showing opposite changes to the systemic blood pressure response (**Figure 4.4**C), with under- and over- shooting after paradigm (occlusion and reperfusion) changes. Higher frequency neuronal activity originates from local neuron recruitment (Demanuele *et al* 2007), possibly reflecting the initial disruption of hypoxia on small local networks. None of the frequency bands analyzed returned to baseline power levels. Despite this, the animals in the study by Pulsinelli *et al* did not show abnormal behavior following recovery, and neuronal ischemic damage was delayed on the order of hours (Pulsinelli *et al* 1982). Schmidt-Kastner *et al* reported EEG traces returned to normal 72 hours following occlusion, both far beyond the time frame monitored in our present study (Schmidt-Kastner *et al* 1989). These findings could explain the majority of similar changes between the first and second occlusions as observed in the present study.

Analysis of group responses to occlusion and reperfusion revealed strong correlations ($|r| > 0.8$, all with $p < 0.001$) between neuronal and metabolic changes. Both pH and PCr had correlations of greater than 0.8 to LF ($r = 0.87$ and 0.86) and MF ($r = 0.83$ and 0.81) bands of the neuronal power. Correspondingly, there was a strong correlation between pH and PCr ($r = 0.82$, $p = 7.6e^{-22}$). As mentioned previously, lactate

and pH were also inversely correlated (r = -0.85), as expected from the acidic nature of lactate. BOLD was not strongly correlated with any other measure, presumably due to a fast reduction in response to occlusion.

4.5 DISCUSSION

Pulling all of these dynamic responses together, our high temporal resolution simultaneous ^{1}H-^{31}P measurement allows a cause-and-effect flow to be extrapolated. Upon the occlusion onset, BOLD decreases dramatically due to the rapid and substantial reduction in blood supply and perfusion, resulting in an increase in highly deoxygenated hemoglobin. This BOLD measure is mainly determined by the hemodynamic or perfusion changes during and after the 12-minute occlusion. Field potential power activity closely follows the changes in blood flow and BOLD, showing immediate suppression after the onset of occlusion. This suggests a tightly coupled neuro-vascular relationship, as seen previously (Raffin *et al* 1991). The rapid metabolic switch to glycolysis is triggered by the lack of oxygen supply during occlusion, where PCr reserves are consumed at a constant decay rate to maintain ATP following occlusion onset, and results in Lac byproducts and a change in pH within 30 seconds, or one MRS data point. ATP stores are tapped 2.2 minutes after occlusion induction, when low-frequency field potential powers and BOLD reach low steady states, indicating the need for the brain to maintain a minimum neuronal activity level, and relating to the maintenance of the basic housekeeping brain energy proposed by Attwell *et al* (Attwell *et al* 2001), Du *et al* (Du *et al* 2008), and Howarth *et al* (Howarth *et al* 2012). Energy metabolites continue to

decrease throughout the 12-minute occlusion, reaching a pseudo steady state as the occlusion release time-point is approached. Particularly in comparison with dead brain signal measures, the very low neuronal activity and metabolic concentration levels needed to maintain this housekeeping energy reveals the brain's robustness to harsh conditions.

The return of blood flow is reflected in an immediate recovery of BOLD, returning to baseline within 2 minutes. PCr, ATP, and field potential power begin to recover without a delay, but at a much slower rate than BOLD. In contrast, the recovery of Lac and pH is delayed 1.5 - 2 minutes, likely as a result of continued glycolysis in order to return ATP and PCr to a normal concentration range. The slow recovery of Lac to its baseline level points to a dominant but slow Lac transport efflux and blood flow washout as opposed to an active metabolic breakdown. The PCr recovery to a steady state was not significantly different from pre-occlusion baseline ($p = 0.79$), while ATP did not recover to baseline ($p = 8.3e^{-4}$), staying at 80% of baseline, with both recoveries mainly occurring within 10 minutes following reperfusion. The small differences in the degree of PCr recovery to baseline for first versus second occlusion would not raise this group ATP recovery baseline to 100% if the concentrations were quantified for each occlusion group separately. This persistent ATP depletion during the reperfusion period, though small, may contribute to the increased severity of the second occlusion. LF, LG, and MF field potential bands reached a steady state at 70% of baseline shortly after, followed by pH

and Lac returning slowly to baseline. Interestingly, most physiological measures gradually recovered to the baseline levels during the reperfusion period, however, both ATP and neuronal activities remained below the baseline levels. This finding again indicates a tight coupling relationship between the brain ATP availability and neuronal activity impairment.

The results and temporal correlations among multiple neurophysiological measures collectively suggest that the cellular ATP availability and production through oxidative phosphorylation in mitochondria and its dynamics have a major influence on the outcome and temporal behavior of other physiological changes, in particular, neuronal field potentials and tissue pH. From a neuroenergetic perspective, oxygen metabolism is essential for ATP generation, since the metabolism of a single glucose molecule can generate more than 30 ATP molecules via oxygen metabolism, as compared to only 2 ATP via glycolysis. The total oxygen stored in the brain tissue is very limited, and can only sustain cerebral oxygen metabolism for less than 30 seconds if the arterial oxygen supply is completely stopped due to the occlusion. Therefore, PCr plays an immediate role in supporting the ATP conversion, and meanwhile, the glycolysis metabolism of the tissue glucose and glycogen reserves are enhanced to produce ATP energy during the ischemic challenge, though with low efficiency. Therefore, we hypothesize that the delay time of brain ATP level reduction after the onset of ischemic insult should provide a sensitive measure of the ischemic severity, and reflects the

outcome of highly coupled dynamics among hemodynamic, metabolic, and neuronal activity responses.

While displaying temporally different trends, the dynamic changes of hemodynamic, metabolic, and neuronal activity during whole-brain ischemia and reperfusion are tightly related in general, and are crucial for cell viability and survival of the insult. High temporal resolution simultaneous multi-channel MRS acquisition is a powerful tool to investigate these dynamic responses. In this study, we have shown that this advanced MRS technique is capable of quantitatively revealing dynamics and correlations between Lac and PCr changes within a single animal brain. Group comparison of Lac, PCr, ATP, pH, and BOLD with neuronal field potential power bands highlights the importance of a tight neuronal-vascular coupling to conserve metabolic energy stores during the extremely hypoxic state. We observe, for the first time *in vivo*, a 2.2-minute conservation of cerebral ATP levels, a potentially important time-point related to the minimal neuronal activity levels required to allow functional recovery upon reperfusion. The overall results provide new insights into a comprehensive and dynamic relationship between neuronal activity, brain hemodynamic, and metabolic changes in response to an acute ischemia and during post-ischemic reperfusion.

Chapter 5 :

DYNAMIC BRAIN STATE CHANGES

This chapter contains portions from the submitted manuscript:

Taylor, Jennifer M, Corey Cruttenden, Shan Hu, Xiao-Hong Zhu, Yi Zhang, Rajesh Rajamani, Wei Chen. "Simultaneous MRI and Electrophysiology Acquisition with Nano-Structured Carbon Electrodes: A Proof of Concept Study."

5.1 BACKGROUND

We demonstrate unique proof-of-concept applications for the MR-compatible nano-structured carbon electrodes, acquiring truly simultaneous *in vivo* neuronal recordings and fMRI under a dynamic anesthesia paradigm. Shannon entropy was used to quantify the neuronal activity state of the brain from the LFP traces, based on good correlations between EEG and entropy for anesthetized patients (Bruhn *et al* 2001). The robust correlation between entropy and LFP bursts can be seen in **Figure 5.1**. BOLD fMRI time courses and connectivity maps were generated from 5-6 minutes segments that were interleaved with the neuronal recording activity. MR-induced artifact removal using template subtraction had inconsistent results, so here artifacts were not removed prior to entropy calculations, unless otherwise indicated.

In general, deep anesthesia reduces neuronal activity and cortical network connectivity. As anesthesia lightens, both the neuronal activity and connectivity increase. Under very light anesthesia, the activity pattern shifts to a more constant oscillatory pattern, and connectivity becomes more specific. These trends were investigated in our lab previously for isoflurane anesthesia (Liu *et al* 2011). However, individual animal responses demonstrated a large population heterogeneity. For instance, both Examples 2 and 3 (**Figure 5.3, 5.4**) start at 1.6% isoflurane, and yet their connectivity maps show different cortical recruitment and correlation strengths. The endpoint of Example 4 (**Figure 5.5**) is also at 1.6%, showing increased cortical connectivity compared to

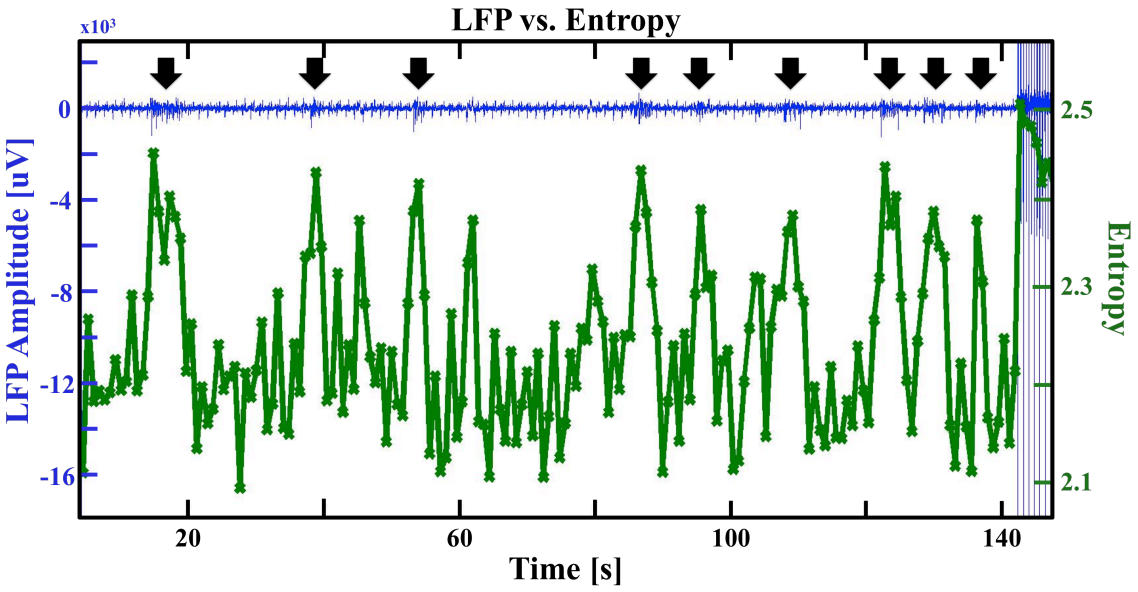

Figure 5.1. *Comparison of entropy and LFP bursts. Entropy calculated with 1-second temporal resolution to catch burst dynamics reliably. Higher entropy values correspond to LFP burst times and durations. The addition of MR-induced artifacts at ~140 seconds results in an artificially high entropy value.*

Examples 2 and 3. Based on these experimental observations of animal-specific response to anesthesia depth, changes in neuronal activity, BOLD, and network connectivity maps to changing anesthesia are investigated here. These observations also emphasize the importance of acquiring simultaneous measures of neuronal and fMRI BOLD signals from a single trial.

5.2 EXAMPLE RESPONSES

In Example 1 (**Figure 5.2**), the isoflurane was quickly dropped from 2.1% to 1.7%. The entropy, excluding the gray MR-artifact regions, increases to a new higher steady state in tight correlation with the anesthesia depth. The BOLD voxel time course does not begin to change until 13 minutes after the isoflurane drop. In this case, the BOLD changed in the same direction as the isoflurane, opposite the entropy, although this may be related to the vasodilator properties of isoflurane (Schwinn *et al* 1990). The weak correlation network under 2.4% ISO dramatically increases in spread across both slices by the third EPI block before stabilizing.

For both Example 2 (**Figure 5.3**) and Example 3 (**Figure 5.4**), anesthesia was raised from 1.6% to 2.4%. Despite started at the same anesthesia level, their baseline connectivity maps are very different, with Example 2 having higher correlation values but less cortical recruitment than Example 3. Entropy in both examples drops as the anesthesia rises, as expected due to the reduced neuronal activity. Their connectivity

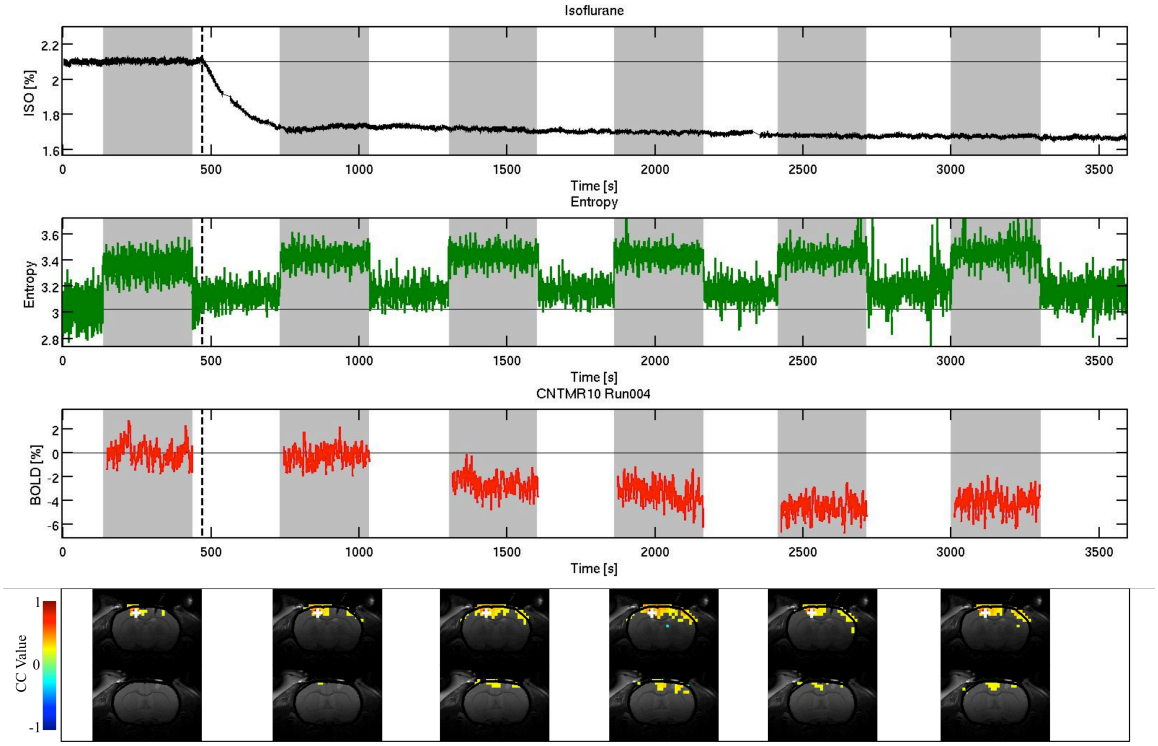

Figure 5.2. *Simultaneous Example 1, without artifact removal. As the anesthesia drops, the entropy and correlation map increases. The seed BOLD voxel decreases inversely of the entropy.*

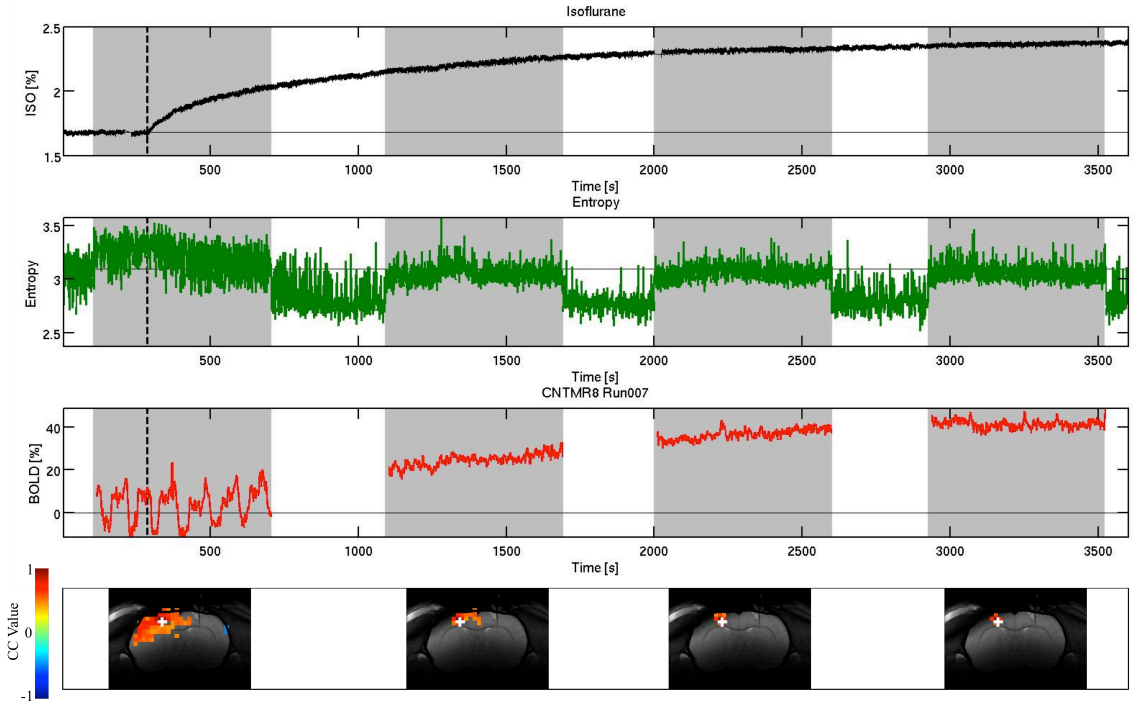

Figure 5.3. *Simultaneous Example 2, without artifact removal. As anesthesia increases from 1.6% - 2.4%, entropy and the connectivity map decreases, while the BOLD seed voxel increases. Note that a low-frequency oscillation pattern at 1.6% ISO vanishes after anesthesia increase.*

networks also shrink dramatically. However, their seed BOLD time courses go in opposite directions. Notice that, as with Example 1, the BOLD does not begin to significantly change until 10+ minutes after the anesthesia change initiation.

In Example 4 (**Figure 5.5**), the MR-induced artifacts could be reliably removed from all MRI acquisition blocks. Following a large drop in isoflurane from very deep (2.3%) to deep (1.8%) anesthesia, neuronal bursting increased in duration and frequency. This is reflected in a matching increase in entropy, which has an inverse correlation of -0.94 ($p = 4.6e^{-166}$) with the isoflurane level. The entropy calculations provide a clean way of quantifying neuronal activity and artifact residual levels. When raw (artifact filled) signal is used for entropy, entropy jumps up during MR acquisition. However, following removal, entropy remains stable during the transition period (i.e. between EPI and no EPI).

Network analysis of the fMRI data revealed an increase in cortical connectivity over the hour acquisition period as the anesthesia lightened, and temporal BOLD fluctuations show an increase in variability at lower anesthesia. Notice that the entropy curve shows no apparent jump during periods of fMRI acquisition with its subsequent MR-induced artifacts (grey background in **Figure 5.5**), highlighting the lack of significant residuals. Additionally, neuronal activity during fMRI acquisition was comparable to baseline activity, indicating no activation responses induced by the fMRI

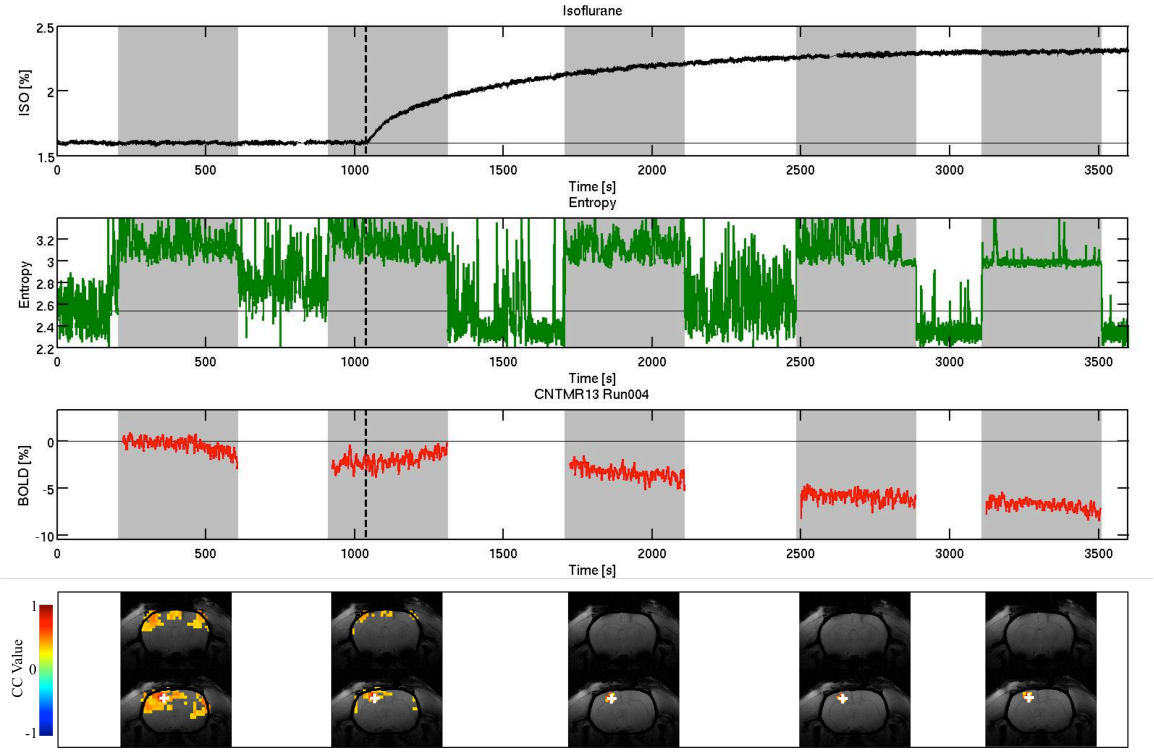

Figure 5.4. *Simultaneous Example 3, without gradient removal. Notice that baseline BOLD and entropy drifted despite a stable anesthesia. Once anesthesia increases, the network maps and entropy immediately drop. In contrast with the previous examples, BOLD here drops with increasing anesthesia.*

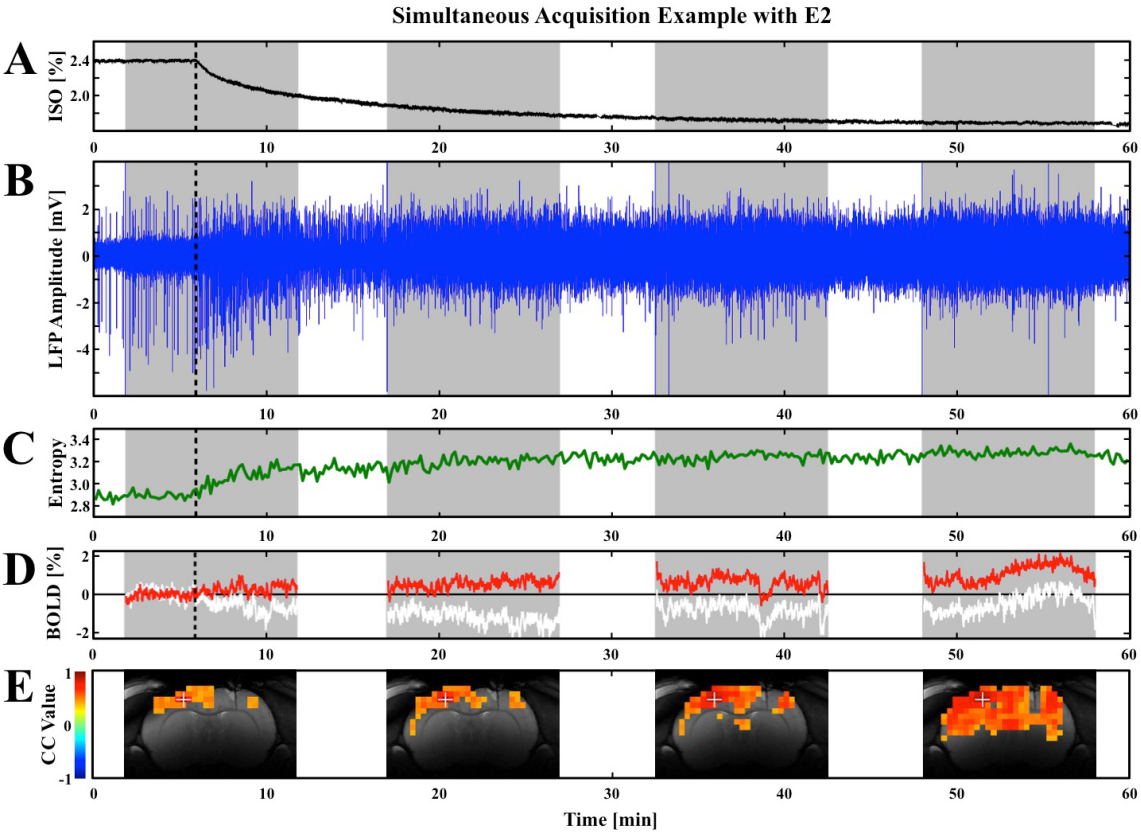

Figure 5.5. *Simultaneous Example 4, with gradient artifact removal. MR acquisition periods are highlighted in grey. (A) Isoflurane anesthesia concentration. (B) Post-processed LFP bursting activity, with an increase as the anesthesia lightens. (C) LFP Entropy mirrors the anesthesia, and is unaffected by the small residual of MR-induced artifacts. (D) Single voxel BOLD signals from the electrode (white trace) and contralateral cortex (red trace) show a baseline drift as well as an increase in amplitude and frequency. (E) fMRI connectivity from each acquisition block. The extent of the cross-correlation network ($|cc| > 0.5$, $p < 0.05$) increases in spread, although delayed from the neuronal and single voxel responses. The seed region is in the contralateral cortex (white cross).*

acquisition. The cortical region directly around the electrode did not meet the thresholds used for connectivity map analysis here, however a visual comparison of the BOLD fluctuations (red vs. white trace in **Figure 5.5**D), reveals similar dynamics. Notice that the direction of BOLD change was different for the 2 different voxels, similar to the inconsistent directions in the previous examples. The connectivity maps for this animal showed high correlation values and wide cortical spread, with the network at 1.8% having much larger spread than that at 1.7% in Example 1 and 2. Note that Examples 4 and 2 came from the same animal, with the variation reflecting inconsistent networks and complex anesthesia effects over time.

Although some residuals remained, two slice EPI MR-induced artifacts can be removed from simultaneous collected LFP signals, as seen in **Figure 5.6**. As with the previous example, the entropy level does not jump between the sections with (grey) and without (white) MR acquisition. Some residuals remained in the second half of the EPI block due to large baseline drifts.

5.3 MR SPECTROSCOPY

The simultaneous acquisition is not limited to fMRI, but can be extended to MRS sequences. Using global ^{31}P with BISTRO saturation pulse trains (Luo *et al* 2001), a large portion of the MR-induced artifacts were removed (**Figure 5.7**) despite being much larger and more complex than the fMRI-induced artifacts. Notice that the entropy

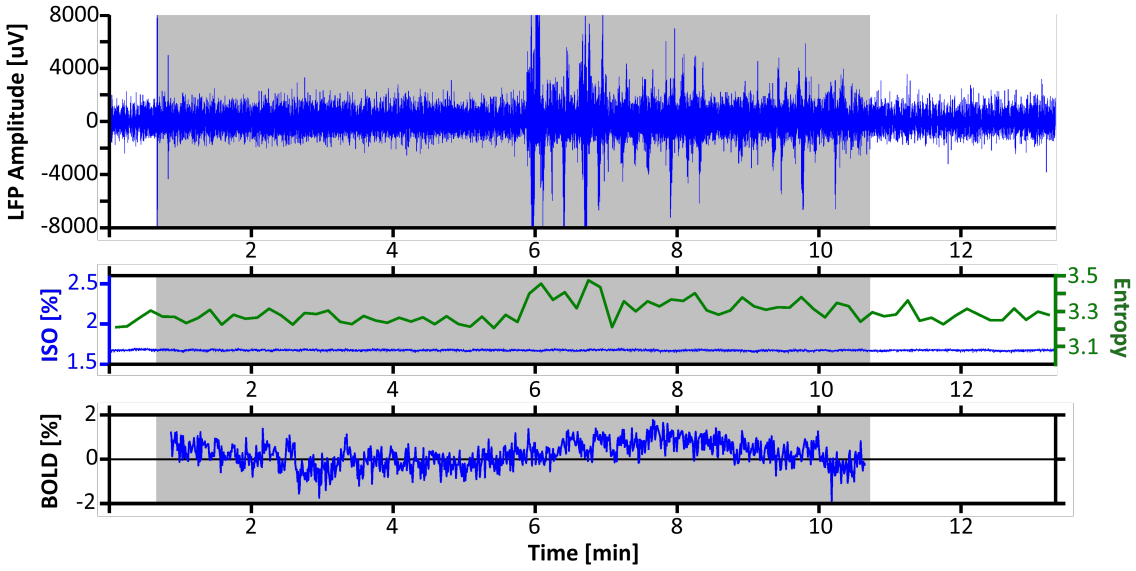

Figure 5.6. *Simultaneous 2 slice EPI and neuronal activity after MR-induced artifact removal. Due to large baseline drifts resulting in amplifier saturation, some residual artifacts remained in the second half of the MR acquisition period.*

calculations are highly sensitive to the remaining MR-induced artifact residuals, but can be extrapolated when necessary. As the anesthesia increased, the entropy decreased. In magnetization transfer difference spectra, dynamics in ATP and PCr and be observed. While some of the fluctuations may be related to noise, some correlations with the increase in entropy and LFP burst activity towards the end of the recording period (following the last MR block) may be connected to the decrease in PCr peak height.

5.4 DISCUSSION

In these proof-of-concept examples, the power of these simultaneous measurements to explore neuronal activity, BOLD, and network connectivity is clearly demonstrated. With these methods, a glimpse into the variability of responses across animals, as well as in time, is shown. High temporal resolution events can be observed, and direct comparisons between local neuronal responses and whole brain network activity can be made. From these examples, the use of this technology can be expanded to study resting activity and activated activity in normal and pathological animal models. To improve future data quality, bipolar recordings and advanced acquisition circuits will be applied to minimize the effects of MR-induced artifacts on the acquired signal.

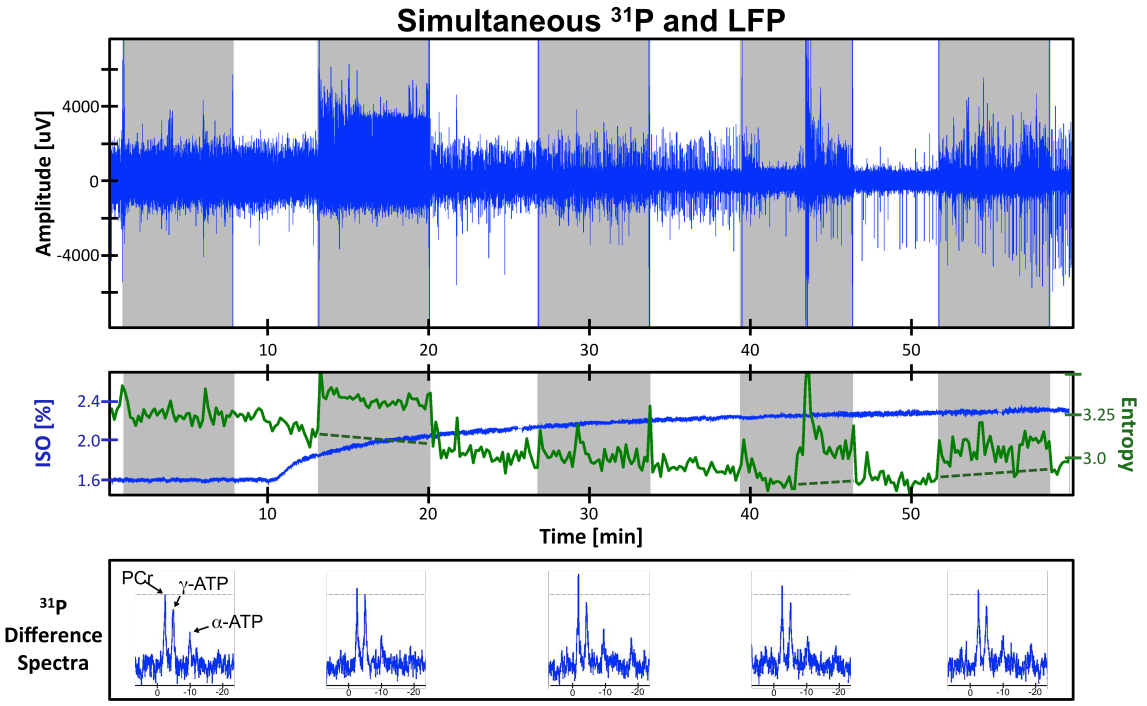

Figure 5.7. *Simultaneous in vivo ^{31}P MRS and neuronal activity with BISTRO saturation on the γ-ATP peak during dynamic anesthesia depth. Some of the MR-induced artifacts were removable, however, large residuals remained in some sections. The entropy calculations are particularly sensitive to the residual (example in the second MR block), however extrapolations can be made across these areas (dashed green lines). Difference spectra (control – saturated) for each block reveal metabolic changes as the anesthesia changes.*

Chapter 6 :

MR-COMPATIBLE OPTRODES

6.1 BACKGROUND

Optogenetics is a burgeoning field that genetically alters neurons to allow activation with light. A light sensitive gene is converted into a vector, called an opsin, and is injected into a region of interest in the brain via a virus. The virus is modified to target a specific cell type, such as excitatory neurons, and an ion channel type. Once infected, coherent light is shone onto the neuron to selectively open the ion channels, typically with the goal of generating an action potential. The activation can be performed on the cell bodies, axons, or terminals to activate specific neuronal populations. Additionally, if their projections are known, isolated projection targets can be activated to investigate the network connections and downstream affects. For example, following the introduction of Channelrhodopsin-2 (ChR2) into a localized region of non-human primate primary visual (V1) cortex, it was found that cell specific activation mimicked a flashing visual stimulus in the neuron's receptive field, resulting in a saccade (Jazayeri *et al* 2012).

Recently, optogenetic techniques have been introduced into fMRI studies to investigate neuronal and hemodynamic coupling. Stimulation of excitatory neocortical neurons generated a positive BOLD response in its predicted downstream target verifying a match between functional and structural connections (Lee *et al* 2010). Similarly, a BOLD response was found to reflect a linear summation of an optical stimulation train of mouse barrel field pyramidal neurons in proportion to the neuronal response (Kahn *et al*

2011). Recently, Duffy *et al* used carbon fiber optrodes to optically induce seizures in rats and monitor their LFP and BOLD response profiles (Duffy *et al* 2015).

In order to fully investigate the local neuronal and global network effects of optical stimulation, we have developed MR-compatible CNT electrodes on optical fibers, herein referred to as CNT optrodes. These optrodes allow the direct recording of neuronal baseline activity and response directly at the optical stimulation site. Used in conjunction with fMRI, we can investigate the network effects and neuronal responses of targeted optical activation and its correlations with neuronal activation.

6.2 ELECTRODE DESIGN

Similar to the previously described carbon nanomaterial electrodes (see **Chapter 3**), CNT was added using layer-by-layer methods onto optical fibers with ceramic ferrules, as seen in (**Figure 6.1**). A silver wire was adding to the bottom half of the ferrule, connecting the CNT to the recording system. The top half of the ferrule was left unaltered in order to provide a connection point for light transmission. PDMS insulation was applied, leaving a cylindrical CNT recording tip exposed. The end of the coated fiber was then polished to remove any CNT from covering the end and to permit proper light transmission to the tissue.

As a control, a tungsten optrode was made by attaching a tungsten multi-unit

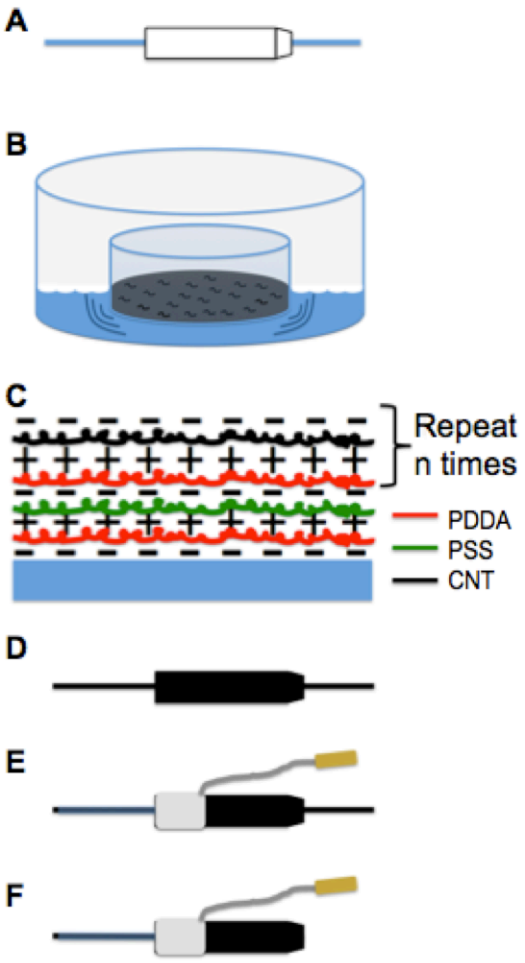

Figure 6.1. *Optrode manufacturing flowchart. (A) Optical fiber is glued to a ceramic ferrule. (B) CNT dispersion is prepared. (C) Optical fiber and ferrule are treated with layer-by-layer method to promote adhesion. (D) The optrode is coated with layers of CNT. (E) A wire and pin are attached to the optrode following PDMS insulation.(F) Proximal optical fiber excess is trimmer, and both proximal and distal ends are polished. Figure courtesy of Corey Cruttenden.*

activity wire electrode to an optical fiber and ferrule, with the tip of the electrode and the optical fiber closely aligned, similar to the optrodes developed by Armstrong *et al* (Armstrong *et al* 2013).

6.3 ELECTRODE TESTING

6.3.1 SUSCEPTIBILITY TESTING

Multiple steps in the manufacturing process were investigated for susceptibility artifacts. It was found that glass optical fiber generated a shadow artifact while plastic optical fibers did not. The addition of CNT onto the fiber, as well as the connection to the ferrule did not introduce additional artifacts. PDMS insulation increased the overall width of the electrode, but again did not introduce susceptibility artifacts in T_1-weighted images, as can be seen in **Figure 6.2**. The prototype optrodes had an observed width of 215 μm and 860 μm without and with insulation, respectively, and was consistent with the microscope observed widths of 206 μm and 979 μm. Being limited by the optical connection ferrule, a silver wire was used as a connection between the CNT and an eternal connector on the bottom half of the ferrule, however it created a large artifact even in T_1-weighted imaging, and would be located close to the brain *in vivo*. Alternative connector materials, such as carbon fiber, are being investigated.

6.3.2 IMPEDANCE TESTING

Impedance is an important factor in signal quality for a recording electrode. For

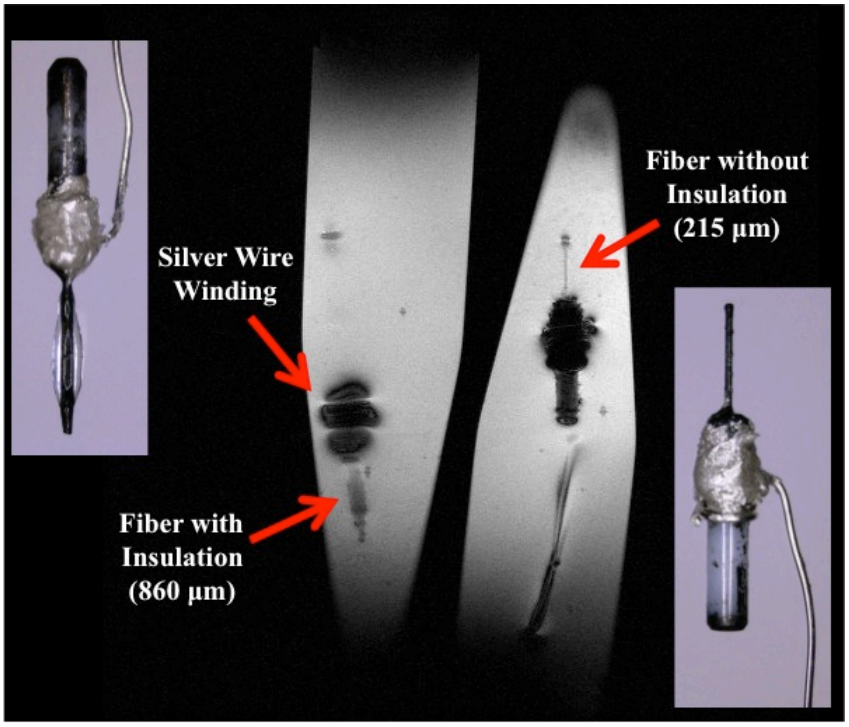

Figure 6.2. *Phantom T_1-weighting images of two CNT optrodes at 9.4T, with corresponding microscope images. (Left) Optical fiber covered with CNT and PDMS insulation. An apparent width of 860 µm in the MR image matches the microscope measurement of 979 µm, although large artifacts were generated from the silver wire connector. (Right) Optical fiber covered with CNT only. An apparent width of 215 µm matches the microscope measurement of 206 µm.*

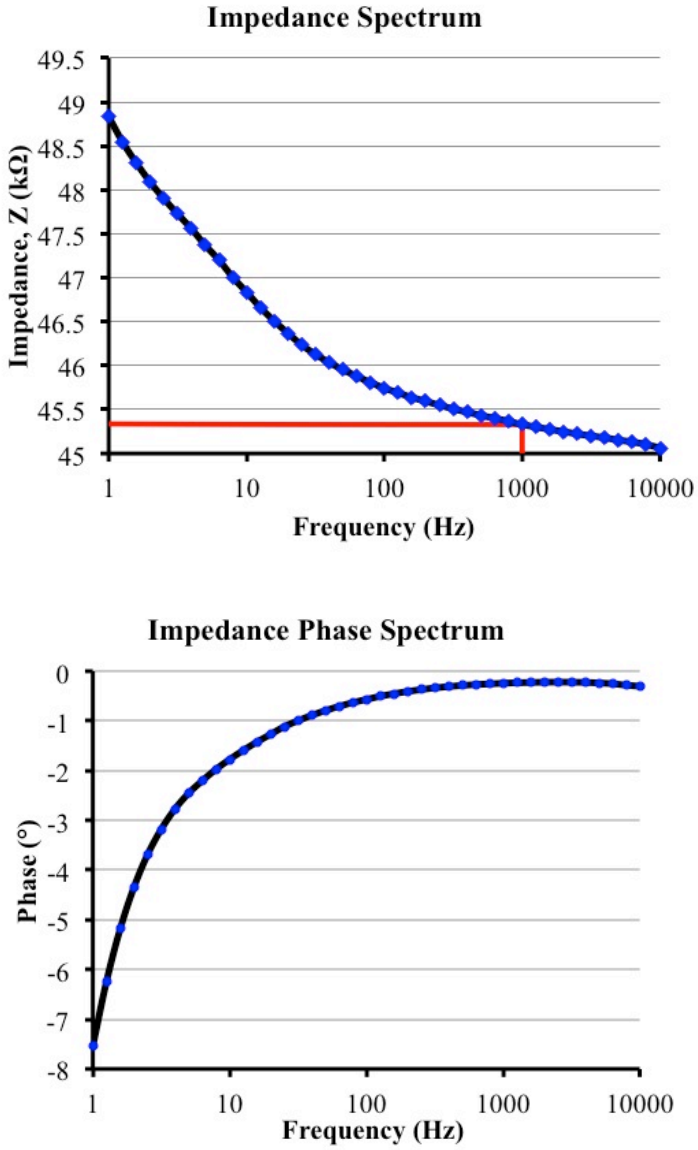

Figure 6.3. *Impedance test of prototype CNT optrode prior to in vivo implantation with both magnitude (left) and phase (right). The impedance of neuronal recording probes is typically measured at 1 kHz (red lines), giving a value here of 44 kΩ. Data courtesy of Corey Cruttenden.*

traditional materials, the impedance values are characterized and are part of the determination of the physiological signal range that is recorded. For example, impedance to acquire LFP signals is typically around 0.5 MΩ, while to record multi and signal unit spike waveforms is typically closer to 1 MΩ. Literature shows that nanomaterial-based electrodes exhibit an approximately order of magnitude lower impedance for the same 2D surface contact area and recording signal quality (Abidian *et al* 2009, Musa *et al* 2012, Collaert *et al* 2014). For this electrode, an impedance spectrum was acquired (**Figure 6.3**) to observe the magnitude and phase profile over a range of frequencies, and an impedance of 45 kΩ was recorded at 1 kHz. A second electrode had an impedance of 44 kΩ, with a similar profile.

6.3.3 Investigation of Photoelectric Effect

It has been found that light itself results in electrical signal generation, called the photoelectric effect (Cardin *et al* 2010, Kozai *et al* 2015). To investigate these false-positive responses in our setup, we placed a CNT optrode and a control tungsten optrode in agar (~2% by weight). We found a reproducible frequency and light amplitude dependent stimulation response to 5, 10, 20, and 40 Hz in the recorded electrical signal of each electrode (**Figure 6.4**). The artifact, seen close-up in **Figure 6.5**, is distinguished by a strong onset response lasting approximately 0.4 ms and an opposite phase off-response of similar duration. A slight saturation effect was seen for repeated stimuli at 40 Hz, however for lower frequency stimuli the response was consistent and robust for the entire

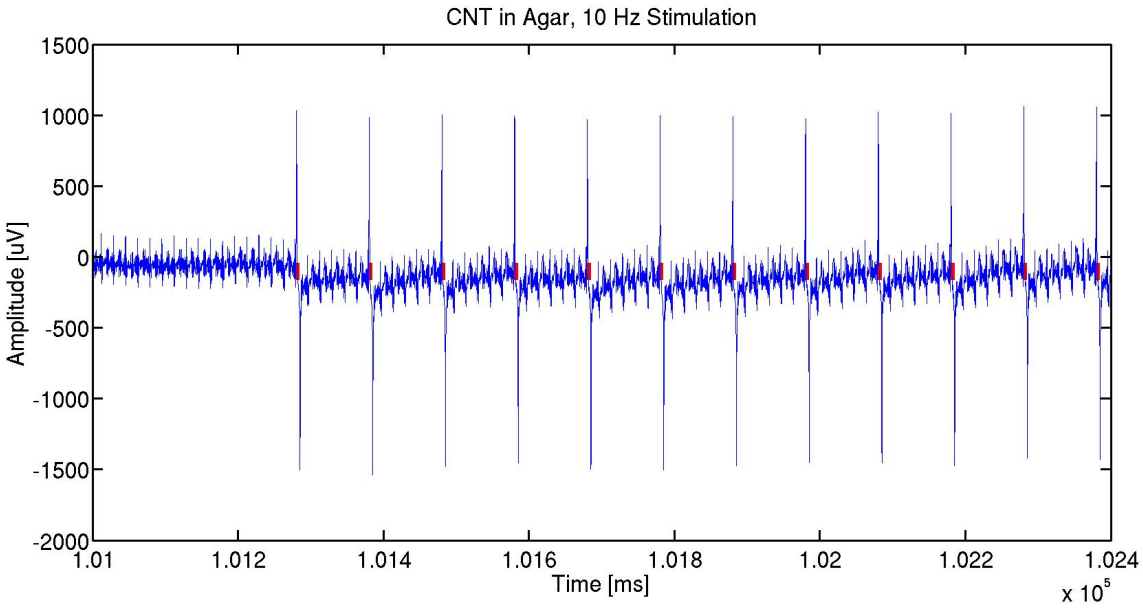

Figure 6.4. *Time course of the 10 Hz stimulus photoelectric effect recorded from a CNT optrode in agar phantom. Red bars indicate the pulse duration of 5 ms. Baseline fluctuations were related to room noise.*

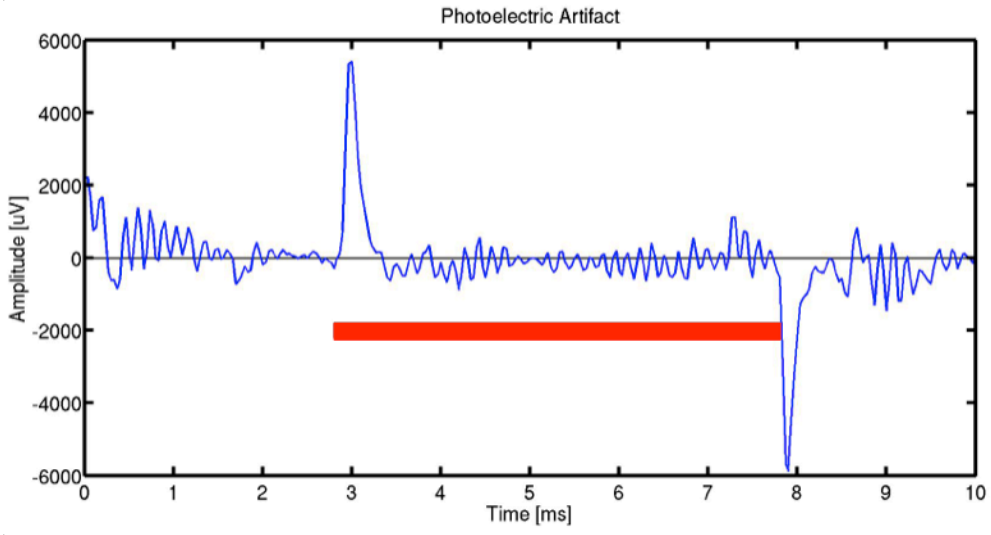

Figure 6.5. *Close up of photoelectric artifact induced in the CNT optrode in an agar phantom. Stimulation ON period indicated with the red bar, with a 5 ms duration. ON response is 0.4 ms long and the OFF response is 0.38 ms long.*

30-second stimulation period. While this artifact complicates the interpretation of *in vivo* results, the reproducibility of this artifact is promising for post-processed removal.

6.5 PRELIMINARY TEST

A mouse was infected with CaMKII-ChR2-EYFP in the ventral hippocampus and allowed to recover for 7 weeks. Under ketamine/xylazine anesthesia, a CNT optrode and a tungsten optrode were implanted bilaterally into the nucleus accumbens shell. Baseline signals from the CNT and tungsten optrodes were comparable in signal quality and noise levels. Similar, but not identical, spontaneous LFP bursts can be seen in **Figure 6.6** in traces from both optrodes.

With high power input to the laser, a square wave pulse train stimulation was applied. Pulses were 5 milliseconds in duration for 30 seconds ON and 30 seconds OFF at a frequency of 5, then 10, then 20, and lastly 40 Hz. Stimulation was performed on each side individually, as well as on both sides simultaneously. Low power stimulation was also performed on each side to check for light-induced cross talk.

A spectrogram, seen in **Figure 6.7**, reveals the multi-frequency response in the LFP range from the 5 and 10 Hz stimulation periods. The responses to 20 and 40 Hz were, in this case, weak. Interestingly, the photoelectric effect is not as robust *in vivo* as in phantom, with this difference highlighted in the comparison of the *in vivo* and *in vitro*

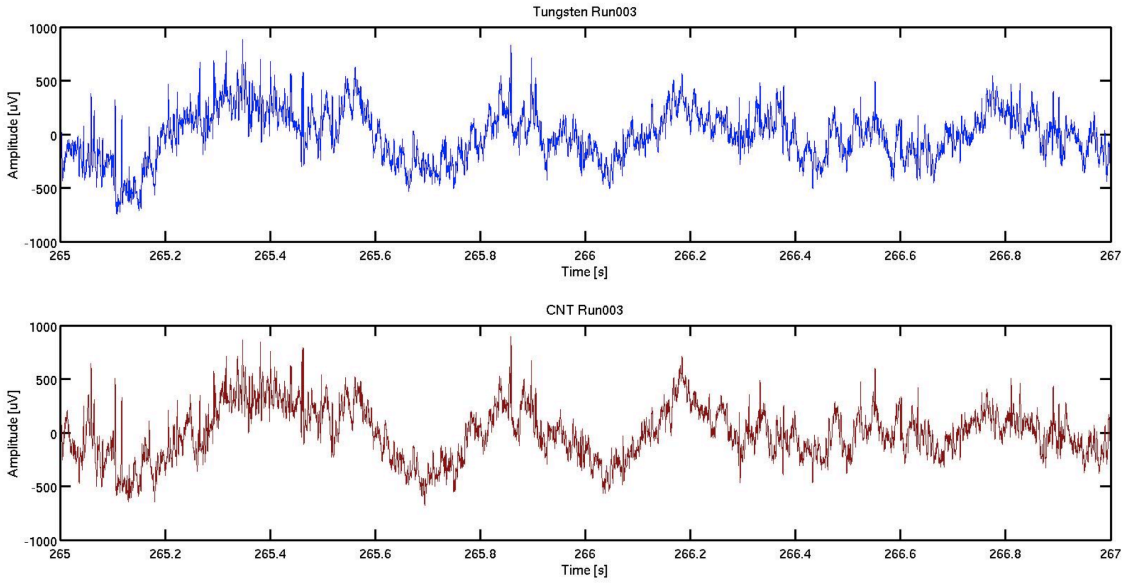

Figure 6.6. *Comparison of spontaneous LFP activity in the tungsten and CNT optrodes. Both channels recorded global activity with similar amplitude and SNR. The slow baseline fluctuation is a breathing artifact.*

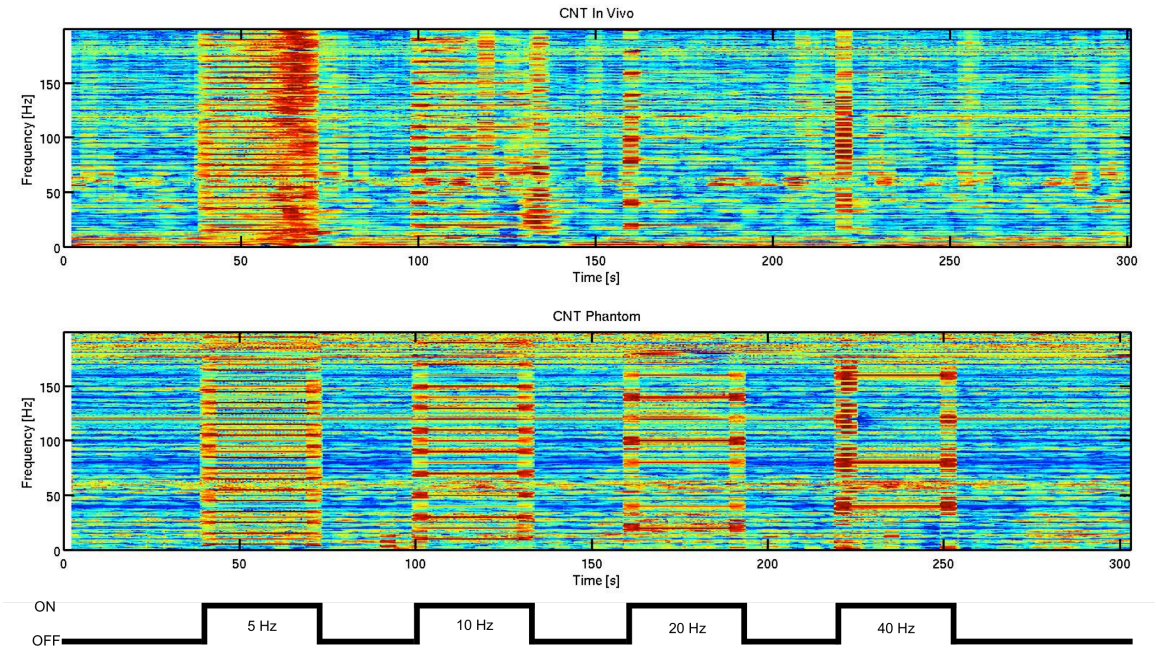

Figure 6.7. *Spectrogram comparison of in vivo (top) and phantom (bottom) responses to 30-second blocks of optical stimulation at 5, 10, 20, and 40 Hz.*

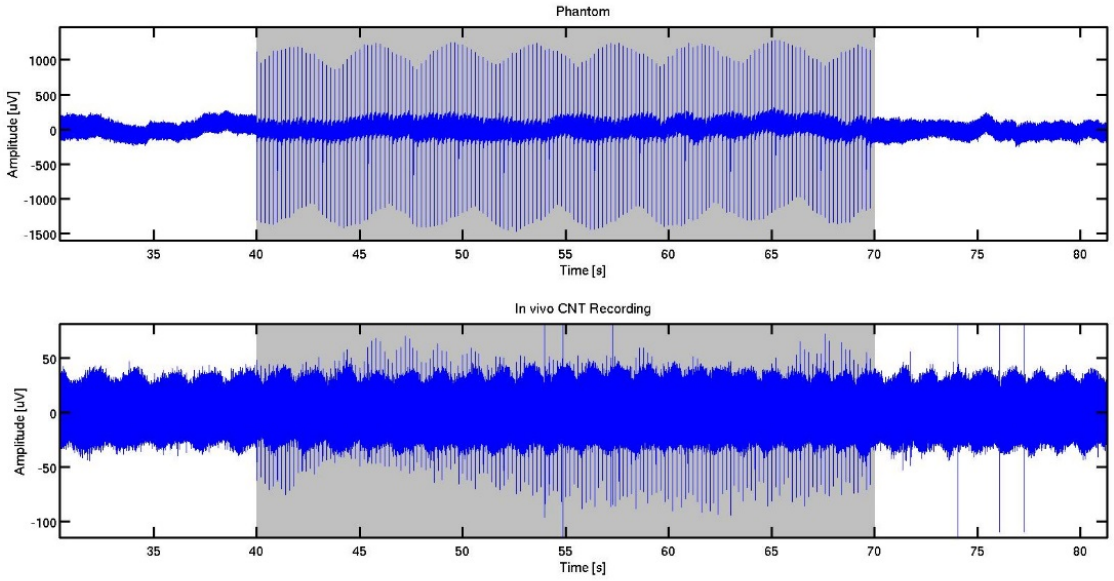

Figure 6.8. *CNT recording time course response to 5 Hz stimulation in phantom (top) versus in vivo (bottom). Despite different scales, the photoelectric effect is not as reproducible in vivo. The grey region indicates stimulation ON. Signal modulation is due to undersampling for visualization purposes in the top plot, and a breathing artifact in the bottom plot.*

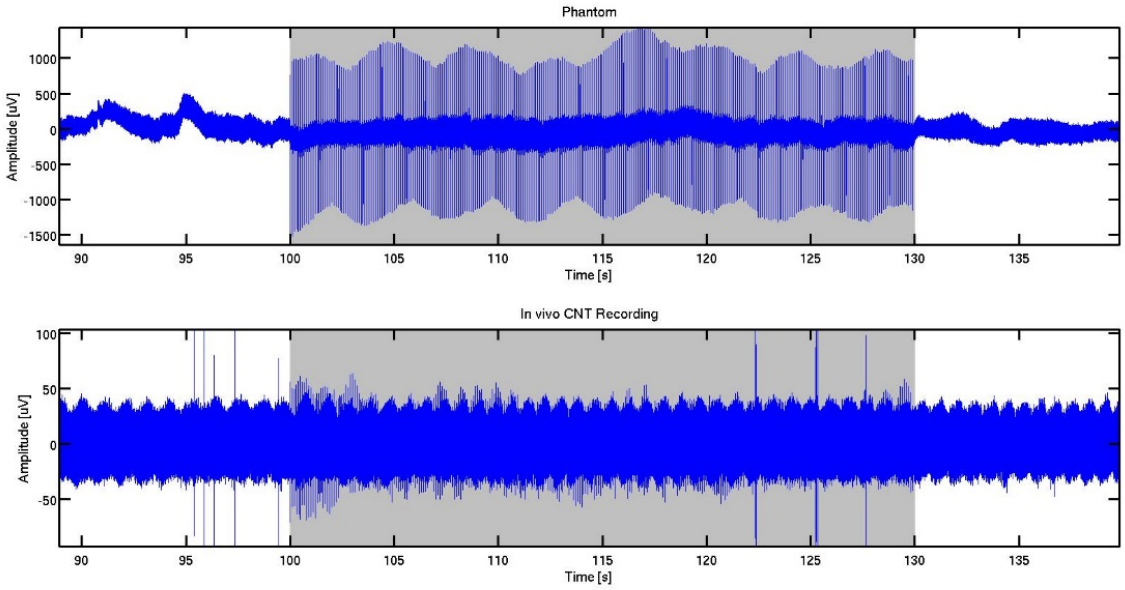

Figure 6.9. *CNT recording time course response to a 10 Hz stimulation in phantom (top) versus in vivo (bottom). The photoelectric effect was again consistent and reproducible in phantom, but is only visible during stimulus onset in vivo. The grey region indicates stimulation ON.*

responses to the 20 and 40 Hz stimulation periods, with onset responses seen in both tests but off responses only seen in phantom. This wide range effect can also be observed in the time domain. For the 5 Hz stimulation, shown in **Figure 6.8**, the photoelectric effect was robust in phantom but not *in vivo*, showing a consistent artifact with varying amplitude. This effect is even further attenuated at 10 Hz (**Figure 6.9**), with little artifact noticeable above noise level in the *in vivo* recording, and only as a stimulation onset response with the amplitude decaying similar to a saturation effect. A reduced artifact amplitude is likely related to differences in light refraction in the agar phantom versus brain tissue, although the artifact variation observed *in vivo* requires more investigation.

Histology was collected a week later, verifying the location of the tungsten electrode tip in the nucleus accumbens shell and the CNT optrode tip in the rostral nucleus accumbens shell (**Figure 6.10**). Presence of fluorescence in terminals in the nucleus accumbens originating from ventral hippocampus indicates proper transfection, however this was observed only in the CNT implantation hemisphere (**Figure 6.11**).

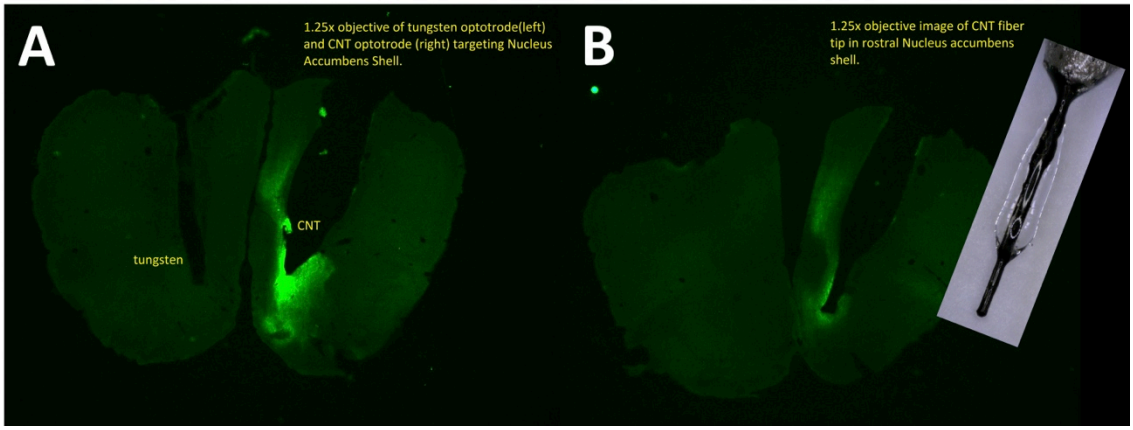

Figure 6.10. *Optrode mouse histology. Looking at the (A) nucleus accumbens shell, proper placement of the tungsten optrode can be seen in the left hemisphere, although without the green fluorescence indicating proper opsin transfection. (B) The CNT optrode tip ended up in the rostral nucleus accumbens shell, with the empty space in the cortex matching the physical space of the electrode and its insulation (inset). Work in collaboration with Drs. Mark Thomas, Anders Asp, and Erin Larson. Modified from a figure by Anders Asp.*

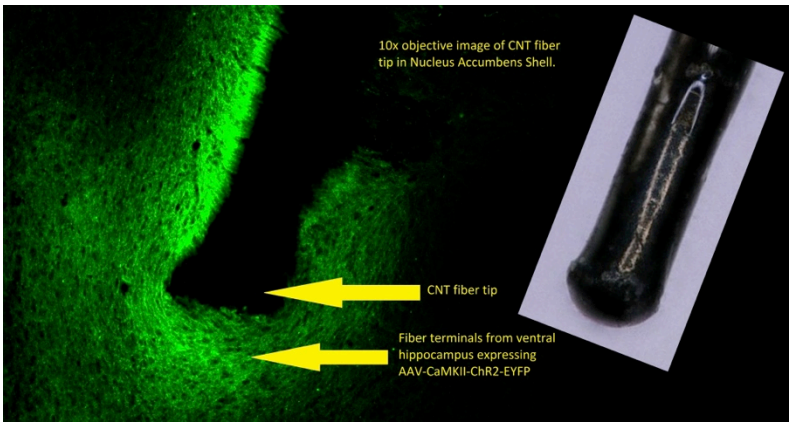

Figure 6.11. *CNT optrode histology close up. Bright green fluorescence indicates the proper presence of axon terminal projections from the infected ventral hippocampus. Modified from a figure by Anders Asp. (Inset) Optical microscope image of optrode at 200X matching the physical void in the brain slice.*

6.7 DISCUSSION

While more refinement is needed, MR-compatible optrodes open up a wide array of experiments. We have shown a proof-of-concept for CNT electrodes on an optical fiber base that does not induce a magnetic susceptibility artifact. With careful polishing, the addition of the CNT does not impact the light transmission through the optical fiber, allowing for use in optogenetic experiments. Preliminary recordings show good SNR during baseline recordings, although more work is needed to eliminate photoelectric artifacts during optical stimulation. Differences in photoelectric responses in phantom versus *in vivo* highlight how neuronal responses were still recordable despite the effect. Using this new technology, we can begin to directly study the neuronal and functional responses to optical stimulation paradigms.

Chapter 7 :

CONCLUSION

In order to further the investigation of brain function at multiple scales, we have demonstrated the successful development of new simultaneous acquisition technologies. By acquiring ^{1}H and ^{31}P MRS together, direct correlations between metabolites can be measured with high temporal resolution. Using this technology to monitor rat metabolic responses to a whole brain occlusion, we showed high animal variability in lactate and PCr responses that would not have been observable in a group analysis. Our high temporal resolution capability allowed the observation of a 2.2-minute delay in ATP depletion following global brain occlusion onset, which in combination with neuronal activity reaching a low steady-state supports the theory of a minimal housekeeping energy level for brain function survival.

Simultaneous acquisition of neuronal activity with fMRI will facilitate an understanding of the relationship between local and global brain function. We have shown that electrodes made from the conductive nano-structured carbon materials CNT and graphene do not induce susceptibility distortions in the highly sensitive EPI fMRI sequence, and that they are capable of recording local field potentials with signal quality comparable to commercial probes. We have demonstrated the use of these electrodes for the investigation of changing anesthesia level responses, finding high variability amongst animal LFP activity and network connectivity maps. Lastly, we have demonstrated an expansion of these CNT electrodes to the manufacturing of MR-compatible optrodes for the integration of optogenetics, neuronal recording or stimulation, and fMRI.

Using these new and integrated techniques, paradigms designed for individual modalities may now be incorporated into new experiments for the investigation of coupling in spontaneous and stimulated conditions. Individual responses to pathological states may also be investigated with the high temporal resolution and SNR of these techniques, eliminating assumptions of repeatability. New insights may now be acquired into the direct correlations and multi-modal responses of neuronal activity, metabolism, and hemodynamics function that together make up the full complexity of brain function.

BIBLIOGRAPHY

1. Abidian MR, Ludwig KA, Marzullo TC, Martin DC, and Kipke DR. Interfacing Conducting Polymer Nanotubes with the Central Nervous System: Chronic Neural Recording using Poly(3,4-ethylenedioxythiophene) Nanotubes. *Advanced Materials* 2009; 21(37):3764-3770.
2. Ackerman JJ, Grove TH, Wong GG, Gadian DG, and Radda GK. Mapping of metabolites in whole animals by ^{31}P NMR using surface coils. *Nature* 1980; 283(5743):167-170.
3. Airaksinen AM, Niskanen JP, Chamberlain R, Huttunen JK, Nissinen J, Garwood M, Pitkanen A, and Grohn O. Simultaneous fMRI and local field potential measurements during epileptic seizures in medetomidine-sedated rats using raser pulse sequence. *Magnetic Resonance in Medicine* 2010; 64(4):1191-1199.
4. Akhavan O, and Ghaderi E. Toxicity of graphene and graphene oxide nanowalls against bacteria. *ACS Nano* 2010; 4(10):5731-5736.
5. Allen PJ, Josephs O, and Turner R. A method for removing imaging artifact from continuous EEG recorded during functional MRI. *Neuroimage* 2000; 12(2):230-239.
6. Alwarappan S, Erdem A, Liu C, and Li C-Z. Probing the Electrochemical Properties of Graphene Nanosheets for Biosensing Applications. *Journal of Physical Chemistry C* 2009; 113(20):8853-8857.
7. An KH, Kim WS, Park YS, Moon JM, Bae DJ, Lim SC, Lee YS, and Lee YH. Electrochemical properties of high-power supercapacitors using single-walled carbon nanotube electrodes. *Advanced Functional Materials* 2001; 11(5):387-392.
8. Armstrong C, Krook-Magnuson E, Oijala M, and Soltesz I. Closed-loop optogenetic intervention in mice. *Nature Protocols* 2013; 8(8):1475-1493.
9. Attwell D, and Laughlin SB. An energy budget for signaling in the grey matter of the brain. *Journal of Cerebral Blood Flow and Metabolism* 2001; 21(10):1133-1145.
10. Bainbridge A, Tachtsidis I, Faulkner SD, Price D, Zhu T, Baer E, Broad KD, Thomas DL, Cady EB, Robertson NJ, and Golay X. Brain mitochondrial oxidative metabolism during and after cerebral hypoxia-ischemia studied by simultaneous phosphorus magnetic-resonance and broadband near-infrared spectroscopy. *Neuroimage* 2014; 102 Pt 1(0):173-183.
11. Bandettini PA, Wong EC, Hinks RS, Tikofsky RS, and Hyde JS. Time course EPI of human brain function during task activation. *Magnetic Resonance in Medicine* 1992; 25(2):390-397.
12. Bareket-Keren L, and Hanein Y. Carbon nanotube-based multi electrode arrays for neuronal interfacing: progress and prospects. *Frontiers in Neural Circuits* 2012; 6:122.

13. Bartolo MJ, Gieselmann MA, Vuksanovic V, Hunter D, Sun L, Chen X, Delicato LS, and Thiele A. Stimulus-induced dissociation of neuronal firing rates and local field potential gamma power and its relationship to the resonance blood oxygen level-dependent signal in macaque primary visual cortex. *European Journal of Neuroscience* 2011; 34(11):1857-1870.
14. Ben-Jacob E, and Hanein Y. Carbon nanotube micro-electrodes for neuronal interfacing. *Journal of Materials Chemistry* 2008; 18(43):5181.
15. Biswal B, Zerrin Yetkin F, Haughton VM, and Hyde JS. Functional connectivity in the motor cortex of resting human brain using echo-planar mri. *Magnetic Resonance in Medicine* 1995; 34(4):537-541.
16. Bolas NM, Rajagopalan B, Mitsumori F, and Radda GK. Metabolic changes during experimental cerebral ischemia in hyperglycemic rats, observed by ^{31}P and ^{1}H magnetic resonance spectroscopy. *Stroke* 1988; 19(5):608-614.
17. Bottomley PA. Spatial Localization in NMR Spectroscopy in Vivo. *Annals of the New York Academy of Sciences* 1987; 508(1 Physiological):333-348.
18. Bruhn J, Lehmann LE, Ropcke H, Bouillon TW, and Hoeft A. Shannon entropy applied to the measurement of the electroencephalographic effects of desflurane. *Anesthesiology* 2001; 95(1):30-35.
19. Cardin JA, Carlen M, Meletis K, Knoblich U, Zhang F, Deisseroth K, Tsai LH, and Moore CI. Targeted optogenetic stimulation and recording of neurons in vivo using cell-type-specific expression of Channelrhodopsin-2. *Nature Protocols* 2010; 5(2):247-254.
20. Chang LH, Shirane R, Weinstein PR, and James TL. Cerebral metabolite dynamics during temporary complete ischemia in rats monitored by time-shared ^{1}H and ^{31}P nmr spectroscopy. *Magnetic Resonance in Medicine* 1990; 13(1):6-13.
21. Chen W, Zhu X-H, Adriany G, and Uğurbil K. Increase of creatine kinase activity in the visual cortex of human brain during visual stimulation: A ^{31}P NMR magnetization transfer study. *Magnetic Resonance in Medicine* 1997; 38(4):551-557.
22. Collaert N, Mora Lopez C, Cott DJ, Cools J, Braeken D, and De Volder M. *In vitro* recording of neural activity using carbon nanosheet microelectrodes. *Carbon* 2014; 67:178-184.
23. Demanuele C, James CJ, and Sonuga-Barke EJ. Distinguishing low frequency oscillations within the 1/f spectral behaviour of electromagnetic brain signals. *Behavioral and Brain Functions* 2007; 3:62.
24. Dreher W, and Leibfritz D. New method for the simultaneous detection of metabolites and water in localized *in vivo* ^{1}H nuclear magnetic resonance spectroscopy. *Magnetic Resonance in Medicine* 2005; 54(1):190-195.
25. Du F, Zhang Y, Iltis I, Marjanska M, Zhu X-H, Henry P-G, and Chen W. *In vivo* proton MRS to quantify anesthetic effects of pentobarbital on cerebral metabolism and brain activity in rat. *Magnetic Resonance in Medicine* 2009; 62(6):1385-1393.

26. Du F, Zhu XH, Zhang Y, Friedman M, Zhang N, Uğurbil K, and Chen W. Tightly coupled brain activity and cerebral ATP metabolic rate. *Proceedings of the National Academy of Sciences* 2008; 105(17):6409-6414.
27. Duffy BA, Choy M, Chuapoco MR, Madsen M, and Lee JH. MRI compatible optrodes for simultaneous LFP and optogenetic fMRI investigation of seizure-like afterdischarges. *Neuroimage* 2015.
28. Dunn JF, Tuor UI, Kmech J, Young NA, Henderson AK, Jackson JC, Valentine PA, and Teskey GC. Functional brain mapping at 9.4T using a new MRI-compatible electrode chronically implanted in rats. *Magnetic Resonance in Medicine* 2009; 61(1):222-228.
29. Duverger D, and MacKenzie ET. The quantification of cerebral infarction following focal ischemia in the rat: influence of strain, arterial pressure, blood glucose concentration, and age. *Journal of Cerebral Blood Flow and Metabolism* 1988; 8(4):449-461.
30. Eleff SM, Schnall MD, Ligetti L, Osbakken M, Subramanian H, Chance B, and Leigh JS. Concurrent measurements of cerebral blood flow, sodium, lactate, and high-energy phosphate metabolism using ^{19}F, ^{23}Na, ^{1}H, and ^{31}P nuclear magnetic resonance spectroscopy. *Magnetic Resonance in Medicine* 1988; 7(4):412-424.
31. Emir UE, Tuite PJ, and Öz G. Elevated pontine and putamenal GABA levels in mild-moderate Parkinson disease detected by 7 tesla proton MRS. *PLoS One* 2012; 7(1):e30918.
32. Fleidervish IA, Gebhardt C, Astman N, Gutnick MJ, and Heinemann U. Enhanced spontaneous transmitter release is the earliest consequence of neocortical hypoxia that can explain the disruption of normal circuit function. *Journal of Neuroscience* 2001; 21(13):4600-4608.
33. Fox MD, and Raichle ME. Spontaneous fluctuations in brain activity observed with functional magnetic resonance imaging. *Nature Reviews Neuroscience* 2007; 8(9):700-711.
34. Fox MD, Snyder AZ, Zacks JM, and Raichle ME. Coherent spontaneous activity accounts for trial-to-trial variability in human evoked brain responses. *Nature Neuroscience* 2006; 9(1):23-25.
35. Gonen O, Murphy-Boesch J, Li C-W, Padavic-Shaller K, Negendank WG, and Brown TR. Simultaneous 3D NMR spectroscopy of proton-decoupled fluorine and phosphorus in human liver during 5-fluorouracil chemotherapy. *Magnetic Resonance in Medicine* 1997; 37(2):164-169.
36. Gonen O, Murphyboesch J, Srinivasan R, Hu JN, Jiang H, Stoyanova R, and Brown TR. Simultaneous and Interleaved Multinuclear Chemical-Shift Imaging, a Method for Concurrent, Localized Spectroscopy. *Journal of Magnetic Resonance, Series B* 1994; 104(1):26-33.
37. Grouiller F, Vercueil L, Krainik A, Segebarth C, Kahane P, and David O. A comparative study of different artefact removal algorithms for EEG signals acquired during functional MRI. *Neuroimage* 2007; 38(1):124-137.

38. Gruetter R. Automatic, localized *in vivo* adjustment of all first- and second-order shim coils. *Magnetic Resonance in Medicine* 1993; 29(6):804-811.
39. Gruetter R, Garwood M, Uğurbil K, and Seaquist ER. Observation of resolved glucose signals in ^{1}H NMR spectra of the human brain at 4 Tesla. *Magnetic Resonance in Medicine* 1996; 36(1):1-6.
40. Gyulai L, Schnall M, McLaughlin AC, Leigh JS, Jr., and Chance B. Simultaneous ^{31}P- and ^{1}H-nuclear magnetic resonance studies of hypoxia and ischemia in the cat brain. *Journal of Cerebral Blood Flow and Metabolism* 1987; 7(5):543-551.
41. Hesselmann G, Kell CA, Eger E, and Kleinschmidt A. Spontaneous local variations in ongoing neural activity bias perceptual decisions. *Proceedings of the National Academy of Sciences* 2008; 105(31):10984-10989.
42. Hopkins AL, and Barr RG. Oxygen-17 compounds as potential NMR T_2 contrast agents: Enrichment effects of $H_2{}^{17}O$ on protein solutions and living tissues. *Magnetic Resonance in Medicine* 1987; 4(4):399-403.
43. Howarth C, Gleeson P, and Attwell D. Updated energy budgets for neural computation in the neocortex and cerebellum. *Journal of Cerebral Blood Flow and Metabolism* 2012; 32(7):1222-1232.
44. Howe FA, Maxwell RJ, Saunders DE, Brown MM, and Griffiths JR. Proton spectroscopy *in vivo*. *Magnetic Resonance Quarterly* 1993; 9(1):31-59.
45. Hoxworth JM, Xu K, Zhou Y, Lust WD, and LaManna JC. Cerebral metabolic profile, selective neuron loss, and survival of acute and chronic hyperglycemic rats following cardiac arrest and resuscitation. *Brain Research* 1999; 821(2):467-479.
46. Hu S, Rajamani R, and Yu X. Flexible solid-state paper based carbon nanotube supercapacitor. *Applied Physics Letters* 2012; 100(10):104103.
47. Hu W, Peng C, Luo W, Lv M, Li X, Li D, Huang Q, and Fan C. Graphene-based antibacterial paper. *ACS Nano* 2010; 4(7):4317-4323.
48. Hyder F, Patel AB, Gjedde A, Rothman DL, Behar KL, and Shulman RG. Neuronal-glial glucose oxidation and glutamatergic-GABAergic function. *Journal of Cerebral Blood Flow and Metabolism* 2006; 26(7):865-877.
49. Jazayeri M, Lindbloom-Brown Z, and Horwitz GD. Saccadic eye movements evoked by optogenetic activation of primate V1. *Nature Neuroscience* 2012; 15(10):1368-1370.
50. Jenkins BG, and Kraft E. Magnetic resonance spectroscopy in toxic encephalopathy and neurodegeneration. *Clinical Opinion in Neurology* 1999; 12(6):753-760.
51. Jupp B, Williams JP, Tesiram YA, Vosmansky M, and O'Brien TJ. MRI compatible electrodes for the induction of amygdala kindling in rats. *Journal of Neuroscience Methods* 2006; 155(1):72-76.
52. Just N, Petersen C, and Gruetter R. BOLD responses to trigeminal nerve stimulation. *Magnetic Resonance Imaging* 2010; 28(8):1143-1151.

53. Kahn I, Desai M, Knoblich U, Bernstein J, Henninger M, Graybiel AM, Boyden ES, Buckner RL, and Moore CI. Characterization of the functional MRI response temporal linearity via optical control of neocortical pyramidal neurons. *Journal of Neuroscience* 2011; 31(42):15086-15091.
54. Kan S, Fan M, and Courtieu J. A single-coil triple resonance probe for NMR experiments. *Review of Scientific Instruments* 1980; 51(7):887.
55. Keefer EW, Botterman BR, Romero MI, Rossi AF, and Gross GW. Carbon nanotube coating improves neuronal recordings. *Nature Nanotechnology* 2008; 3(7):434-439.
56. Kemp GJ, and Radda GK. Quantitative interpretation of bioenergetic data from ^{31}P and ^{1}H magnetic resonance spectroscopic studies of skeletal muscle: an analytical review. *Magnetic Resonance Quarterly* 1994; 10(1):43-63.
57. Kozai TD, and Vazquez AL. Photoelectric artefact from optogenetics and imaging on microelectrodes and bioelectronics: New Challenges and Opportunities. *Journal of Materials Chemistry B* 2015; 3(25):4965-4978.
58. Kuzum D, Takano H, Shim E, Reed JC, Juul H, Richardson AG, de Vries J, Bink H, Dichter MA, Lucas TH, Coulter DA, Cubukcu E, and Litt B. Transparent and flexible low noise graphene electrodes for simultaneous electrophysiology and neuroimaging. *Nature Communications* 2014; 5:5259.
59. Kwong KK, Belliveau JW, Chesler DA, Goldberg IE, Weisskoff RM, Poncelet BP, Kennedy DN, Hoppel BE, Cohen MS, and Turner R. Dynamic magnetic resonance imaging of human brain activity during primary sensory stimulation. *Proceedings of the National Academy of Sciences* 1992; 89(12):5675-5679.
60. Lee JH, Durand R, Gradinaru V, Zhang F, Goshen I, Kim DS, Fenno LE, Ramakrishnan C, and Deisseroth K. Global and local fMRI signals driven by neurons defined optogenetically by type and wiring. *Nature* 2010; 465(7299):788-792.
61. Li N, Zhang X, Song Q, Su R, Zhang Q, Kong T, Liu L, Jin G, Tang M, and Cheng G. The promotion of neurite sprouting and outgrowth of mouse hippocampal cells in culture by graphene substrates. *Biomaterials* 2011; 32(35):9374-9382.
62. Liebe S, Hoerzer GM, Logothetis NK, and Rainer G. Theta coupling between V4 and prefrontal cortex predicts visual short-term memory performance. *Nature Neuroscience* 2012; 15(3):456-462, S451-452.
63. Liu X, Zhu X-H, Zhang Y, and Chen W. Neural origin of spontaneous hemodynamic fluctuations in rats under burst-suppression anesthesia condition. *Cerebral Cortex* 2011; 21(2):374-384.
64. Ljunggren B, Norberg K, and Siesjö BK. Influence of tissue acidosis upon restitution of brain energy metabolism following total ischemia. *Brain Research* 1974; 77(2):173-186.

65. Logothetis NK, Pauls J, Augath M, Trinath T, and Oeltermann A. Neurophysiological investigation of the basis of the fMRI signal. *Nature* 2001; 412(6843):150-157.
66. Lowry OH, Passonneau JV, Hasselberger FX, and Schulz DW. Effect of Ischemia on Known Substrates and Cofactors of the Glycolytic Pathway in Brain. *Journal of Biological Chemistry* 1964; 239:18-30.
67. Luo Y, de Graaf RA, DelaBarre L, Tannus A, and Garwood M. BISTRO: an outer-volume suppression method that tolerates RF field inhomogeneity. *Magnetic Resonance in Medicine* 2001; 45(6):1095-1102.
68. Malisza KL, Kozlowski P, and Peeling J. A review of *in vivo* ^{1}H magnetic resonance spectroscopy of cerebral ischemia in rats. *Biochemistry and Cell Biology* 1998; 76(2-3):487-496.
69. Mangia S, Tkáč I, Gruetter R, Van De Moortele PF, Giove F, Maraviglia B, and Uğurbil K. Sensitivity of single-voxel ^{1}H-MRS in investigating the metabolism of the activated human visual cortex at 7 T. *Magnetic Resonance Imaging* 2006; 24(4):343-348.
70. Mangia S, Tkáč I, Gruetter R, Van de Moortele PF, Maraviglia B, and Uğurbil K. Sustained neuronal activation raises oxidative metabolism to a new steady-state level: evidence from ^{1}H NMR spectroscopy in the human visual cortex. *Journal of Cerebral Blood Flow and Metabolism* 2007; 27(5):1055-1063.
71. Manivannan S, Saranya AM, Renganathan B, Sastikumar D, Gobi G, and Park KC. Single-walled carbon nanotubes wrapped poly-methyl methacrylate fiber optic sensor for ammonia, ethanol and methanol vapors at room temperature. *Sensors and Actuators B: Chemical* 2012; 171-172:634-638.
72. Manivannan S, Shobin LR, Saranya AM, Renganathan B, Sastikumar D, and Park KC. Carbon nanotubes coated fiber optic ammonia gas sensor. 2011; 7941:79410M-79410M-79417.
73. Mantini D, Perrucci MG, Del Gratta C, Romani GL, and Corbetta M. Electrophysiological signatures of resting state networks in the human brain. *Proceedings of the National Academy of Sciences* 2007; 104(32):13170-13175.
74. Martin C, Martindale J, Berwick J, and Mayhew J. Investigating neural-hemodynamic coupling and the hemodynamic response function in the awake rat. *Neuroimage* 2006; 32(1):33-48.
75. Martinez Santiesteban FM, Swanson SD, Noll DC, and Anderson DJ. Magnetic resonance compatibility of multichannel silicon microelectrode systems for neural recording and stimulation: design criteria, tests, and recommendations. *IEEE Transactions on Biomedical Engineering* 2006; 53(3):547-558.
76. Mateescu GD. Functional oxygen-17 magnetic resonance imaging and localized spectroscopy. *Advances in Experimental Medicine and Biology* 2003; 510:213-218.

77. Merboldt K-D, Bruhn H, Hanicke W, Michaelis T, and Frahm J. Decrease of glucose in the human visual cortex during photic stimulation. *Magnetic Resonance in Medicine* 1992; 25(1):187-194.
78. Meyerspeer M, Kemp GJ, Mlynarik V, Krssak M, Szendroedi J, Nowotny P, Roden M, and Moser E. Direct noninvasive quantification of lactate and high energy phosphates simultaneously in exercising human skeletal muscle by localized magnetic resonance spectroscopy. *Magnetic Resonance in Medicine* 2007; 57(4):654-660.
79. Mirsattari SM, Ives JR, Bihari F, Leung LS, Menon RS, and Bartha R. Real-time display of artifact-free electroencephalography during functional magnetic resonance imaging and magnetic resonance spectroscopy in an animal model of epilepsy. *Magnetic Resonance in Medicine* 2005; 53(2):456-464.
80. Morgenthaler FD, Koski DM, Kraftsik R, Henry P-G, and Gruetter R. Biochemical quantification of total brain glycogen concentration in rats under different glycemic states. *Neurochemistry International* 2006; 48(6–7):616-622.
81. Mukamel R, Gelbard H, Arieli A, Hasson U, Fried I, and Malach R. Coupling between neuronal firing, field potentials, and fMRI in human auditory cortex. *Science* 2005; 309(5736):951-954.
82. Musa S, Rand DR, Cott DJ, Loo J, Bartic C, Eberle W, Nuttin B, and Borghs G. Bottom-up SiO_2 embedded carbon nanotube electrodes with superior performance for integration in implantable neural microsystems. *ACS Nano* 2012; 6(6):4615-4628.
83. Nagatomo Y, Wick M, Prielmeier F, and Frahm J. Dynamic monitoring of cerebral metabolites during and after transient global ischemia in rats by quantitative proton NMR spectroscopy *in vivo*. *NMR in Biomedicine* 1995; 8(6):265-270.
84. Niazy RK, Beckmann CF, Iannetti GD, Brady JM, and Smith SM. Removal of FMRI environment artifacts from EEG data using optimal basis sets. *Neuroimage* 2005; 28(3):720-737.
85. Nielsen AN, and Lauritzen M. Coupling and uncoupling of activity-dependent increases of neuronal activity and blood flow in rat somatosensory cortex. *Journal of Physiology* 2001; 533(3):773-785.
86. Nir Y, Mukamel R, Dinstein I, Privman E, Harel M, Fisch L, Gelbard-Sagiv H, Kipervasser S, Andelman F, Neufeld MY, Kramer U, Arieli A, Fried I, and Malach R. Interhemispheric correlations of slow spontaneous neuronal fluctuations revealed in human sensory cortex. *Nature Neuroscience* 2008; 11(9):1100-1108.
87. Oeltermann A, Augath MA, and Logothetis NK. Simultaneous recording of neuronal signals and functional NMR imaging. *Magnetic Resonance Imaging* 2007; 25(6):760-774.

88. Ogawa S, Lee TM, Kay AR, and Tank DW. Brain Magnetic-Resonance-Imaging with Contrast Dependent on Blood Oxygenation. *Proceedings of the National Academy of Sciences* 1990; 87(24):9868-9872.
89. Ogawa S, Tank DW, Menon R, Ellermann JM, Kim SG, Merkle H, and Uğurbil K. Intrinsic signal changes accompanying sensory stimulation: functional brain mapping with magnetic resonance imaging. *Proceedings of the National Academy of Sciences* 1992; 89(13):5951-5955.
90. Pan WJ, Thompson G, Magnuson M, Majeed W, Jaeger D, and Keilholz S. Simultaneous FMRI and electrophysiology in the rodent brain. *Journal of Visualized Experiments: JoVE* 2010; (42).
91. Pan WJ, Thompson G, Magnuson M, Majeed W, Jaeger D, and Keilholz S. Broadband local field potentials correlate with spontaneous fluctuations in functional magnetic resonance imaging signals in the rat somatosensory cortex under isoflurane anesthesia. *Brain Connectivity* 2011; 1(2):119-131.
92. Park DW, Schendel AA, Mikael S, Brodnick SK, Richner TJ, Ness JP, Hayat MR, Atry F, Frye ST, Pashaie R, Thongpang S, Ma Z, and Williams JC. Graphene-based carbon-layered electrode array technology for neural imaging and optogenetic applications. *Nature Communications* 2014; 5:5258.
93. Park SY, Park J, Sim SH, Sung MG, Kim KS, Hong BH, and Hong S. Enhanced differentiation of human neural stem cells into neurons on graphene. *Advanced Materials* 2011; 23(36):H263-267.
94. Petroff OA, Prichard JW, Behar KL, Alger JR, den Hollander JA, and Shulman RG. Cerebral intracellular pH by ^{31}P nuclear magnetic resonance spectroscopy. *Neurology* 1985; 35(6):781-788.
95. Pfeuffer J, Tkáč I, Provencher SW, and Gruetter R. Toward an *in Vivo* Neurochemical Profile: Quantification of 18 Metabolites in Short-Echo-Time ^{1}H NMR Spectra of the Rat Brain. *Journal of Magnetic Resonance* 1999; 141(1):104-120.
96. Prasai D, Tuberquia JC, Harl RR, Jennings GK, Rogers BR, and Bolotin KI. Graphene: corrosion-inhibiting coating. *ACS Nano* 2012; 6(2):1102-1108.
97. Price TB, Perseghin G, Duleba A, Chen W, Chase J, Rothman DL, Shulman RG, and Shulman GI. NMR studies of muscle glycogen synthesis in insulin-resistant offspring of parents with non-insulin-dependent diabetes mellitus immediately after glycogen-depleting exercise. *Proceedings of the National Academy of Sciences of the United States of America* 1996; 93(11):5329-5334.
98. Pulsinelli WA, and Brierley JB. A new model of bilateral hemispheric ischemia in the unanesthetized rat. *Stroke* 1979; 10(3):267-272.
99. Pulsinelli WA, Brierley JB, and Plum F. Temporal profile of neuronal damage in a model of transient forebrain ischemia. *Annals of Neurology* 1982; 11(5):491-498.

100. Raffin CN, Harrison M, Sick TJ, and Rosenthal M. EEG suppression and anoxic depolarization: influences on cerebral oxygenation during ischemia. *Journal of Cerebral Blood Flow and Metabolism* 1991; 11(3):407-415.
101. Raichle ME, MacLeod AM, Snyder AZ, Powers WJ, Gusnard DA, and Shulman GL. A default mode of brain function. *Proceedings of the National Academy of Sciences* 2001; 98(2):676-682.
102. Reed JC, Zhu H, Zhu AY, Li C, and Cubukcu E. Graphene-enabled silver nanoantenna sensors. *Nano Letters* 2012; 12(8):4090-4094.
103. Rolfe DF, and Brown GC. Cellular energy utilization and molecular origin of standard metabolic rate in mammals. *Physiological Reviews* 1997; 77(3):731-758.
104. Rudin M, and Sauter A. Dihydropyridine calcium antagonists reduce the consumption of high-energy phosphates in the rat brain. A study using combined $^{31}P/^{1}H$ magnetic resonance spectroscopy and ^{31}P saturation transfer. *Journal of Pharmacology and Experimental Therapeutics* 1989; 251(2):700-706.
105. Ryoo SR, Kim YK, Kim MH, and Min DH. Behaviors of NIH-3T3 fibroblasts on graphene/carbon nanotubes: proliferation, focal adhesion, and gene transfection studies. *ACS Nano* 2010; 4(11):6587-6598.
106. Sahni D, Jea A, Mata JA, Marcano DC, Sivaganesan A, Berlin JM, Tatsui CE, Sun Z, Luerssen TG, Meng S, Kent TA, and Tour JM. Biocompatibility of pristine graphene for neuronal interface. *Journal of Neurosurgery: Pediatrics* 2013; 11(5):575-583.
107. Schmidt-Kastner R, Paschen W, Ophoff BG, and Hossmann KA. A modified four-vessel occlusion model for inducing incomplete forebrain ischemia in rats. *Stroke* 1989; 20(7):938-946.
108. Schnall MD, Bolinger L, Renshaw PF, Haselgrove JC, Subramanian VH, Eleff SM, Barlow C, Leigh JS, Jr., and Chance B. Multinuclear MR imaging: a technique for combined anatomic and physiologic studies. *Radiology* 1987; 162(3):863-866.
109. Schnall MD, Yoshizaki K, Chance B, and Leigh JS. Triple nuclear NMR studies of cerebral metabolism during generalized seizure. *Magnetic Resonance in Medicine* 1988; 6(1):15-23.
110. Schneider CA, Rasband WS, and Eliceiri KW. NIH Image to ImageJ: 25 years of image analysis. *Nature Methods* 2012; 9(7):671-675.
111. Scholvinck ML, Maier A, Ye FQ, Duyn JH, and Leopold DA. Neural basis of global resting-state fMRI activity. *Proceedings of the National Academy of Sciences* 2010; 107(22):10238-10243.
112. Schridde U, Khubchandani M, Motelow JE, Sanganahalli BG, Hyder F, and Blumenfeld H. Negative BOLD with large increases in neuronal activity. *Cerebral Cortex* 2008; 18(8):1814-1827.
113. Schwinn DA, McIntyre RW, and Reves JG. Isoflurane-induced vasodilation: role of the alpha-adrenergic nervous system. *Anesthesia & Analgesia* 1990; 71(5):451-459.

114. Shabaneh AA, Girei SH, Arasu PT, Rashid SA, Yunusa Z, Mahdi MA, Paiman S, Ahmad MZ, and Yaacob MH. Reflectance Response of Optical Fiber Coated With Carbon Nanotubes for Aqueous Ethanol Sensing. *IEEE Photonics Journal* 2014; 6(6):1-10.
115. Shmuel A, Augath M, Oeltermann A, and Logothetis NK. Negative functional MRI response correlates with decreases in neuronal activity in monkey visual area V1. *Nature Neuroscience* 2006; 9(4):569-577.
116. Shyu BC, Lin CY, Sun JJ, Sylantyev S, and Chang C. A method for direct thalamic stimulation in fMRI studies using a glass-coated carbon fiber electrode. *Journal of Neuroscience Methods* 2004; 137(1):123-131.
117. Smith MR, Peterson ET, Gordon JW, Niles DJ, Rowland IJ, Kurpad KN, and Fain SB. *In vivo* imaging and spectroscopy of dynamic metabolism using simultaneous ^{13}C and ^{1}H MRI. *IEEE Trasactions on Biomedical Engineering* 2012; 59(1):45-49.
118. Sorkin R, Gabay T, Blinder P, Baranes D, Ben-Jacob E, and Hanein Y. Compact self-wiring in cultured neural networks. *Journal of Neural Engineering* 2006; 3(2):95-101.
119. Sugio K, Horigome N, Sakaguchi T, and Goto M. A model of bilateral hemispheric ischemia--modified four-vessel occlusion in rats. *Stroke* 1988; 19(7):922-922.
120. Tkáč I, Starcuk Z, Choi IY, and Gruetter R. *In vivo* ^{1}H NMR spectroscopy of rat brain at 1 ms echo time. *Magnetic Resonance in Medicine* 1999; 41(4):649-656.
121. Tomida S, Nowak TS, Jr., Vass K, Lohr JM, and Klatzo I. Experimental model for repetitive ischemic attacks in the gerbil: the cumulative effect of repeated ischemic insults. *Journal of Cerebral Blood Flow and Metabolism* 1987; 7(6):773-782.
122. Vincent JL, Patel GH, Fox MD, Snyder AZ, Baker JT, Van Essen DC, Zempel JM, Snyder LH, Corbetta M, and Raichle ME. Intrinsic functional architecture in the anaesthetized monkey brain. *Nature* 2007; 447(7140):83-86.
123. Wang K, Ruan J, Song H, Zhang J, Wo Y, Guo S, and Cui D. Biocompatibility of Graphene Oxide. *Nanoscale Research Letters* 2010.
124. White B, Abbott LF, and Fiser J. Suppression of cortical neural variability is stimulus- and state-dependent. *Journal of Neurophysiology* 2012; 108(9):2383-2392.
125. Xue W, and Cui T. Carbon nanotube micropatterns and cantilever arrays fabricated with layer-by-layer nano self-assembly. *Sensors and Actuators A: Physical* 2007; 136(2):510-517.
126. Yang W, Ratinac KR, Ringer SP, Thordarson P, Gooding JJ, and Braet F. Carbon nanomaterials in biosensors: should you use nanotubes or graphene? *Angewandte Chemie* 2010; 49(12):2114-2138.
127. Young CK, Brown AR, Robinson JH, Tuor UI, Dunn JF, Bland BH, and Teskey GC. Functional MRI response and correlated electrophysiological changes during

posterior hypothalamic nucleus deep brain stimulation. *Neuroimage* 2011; 56(1):35-44.
128. Yu D, and Dai L. Self-Assembled Graphene/Carbon Nanotube Hybrid Films for Supercapacitors. *Journal of Physical Chemistry Letters* 2010; 1(2):467-470.
129. Yu X, Rajamani R, Stelson KA, and Cui T. Active Control of Sound Transmission Through Windows With Carbon Nanotube-Based Transparent Actuators. *IEEE Transactions on Control Systems Technology* 2007; 15(4):704-714.
130. Zhu X-H, and Chen W. Observed BOLD effects on cerebral metabolite resonances in human visual cortex during visual stimulation: a functional ^{1}H MRS study at 4 T. *Magnetic Resonance in Medicine* 2001; 46(5):841-847.
131. Zhu XH, and Chen W. *In vivo* oxygen-17 NMR for imaging brain oxygen metabolism at high field. *Progress in Nuclear Magnetic Resonance Spectroscopy* 2011; 59(4):319-335.
132. Zhu XH, Qiao H, Du F, Xiong Q, Liu X, Zhang X, Uğurbil K, and Chen W. Quantitative imaging of energy expenditure in human brain. *Neuroimage* 2012; 60(4):2107-2117.
133. Zhu XH, Zhang N, Zhang Y, Uğurbil K, and Chen W. New insights into central roles of cerebral oxygen metabolism in the resting and stimulus-evoked brain. *Journal of Cerebral Blood Flow and Metabolism* 2009; 29(1):10-18.
134. Zhu XH, Zhang Y, Tian RX, Lei H, Zhang N, Zhang X, Merkle H, Uğurbil K, and Chen W. Development of ^{17}O NMR approach for fast imaging of cerebral metabolic rate of oxygen in rat brain at high field. *Proceedings of the National Academy of Sciences* 2002; 99(20):13194-13199.